METAL-REDUCED GRAPHENE OXIDE FOR SUPERCAPACITORS AND

ALTERNATING CURRENT LINE-FILTERS

A Thesis
Presented to
The Academic Faculty

by

Zhenkun Wu

In Partial Fulfillment
of the Requirements for the Degree
Doctor of Philosophy in the
School of Materials Science and Engineering

Georgia Institute of Technology
Peking University

August 2015

METAL-REDUCED GRAPHENE OXIDE FOR SUPERCAPACITORS AND

ALTERNATING CURRENT LINE-FILTERS

Approved by:

Dr. Ching-Ping Wong, Advisor
School of Materials Science &
Engineering
Georgia Institute of Technology

Dr. Mei-Lin Liu
School of Materials Science &
Engineering
Georgia Institute of Technology

Dr. Zhong-Lin Wang
School of Materials Science &
Engineering
Georgia Institute of Technology

Dr. Shu-Lin Bai, Co-Advisor
Department of Materials Science &
Engineering
Peking University

Dr. Ping-Chou Han
Department of Materials Science &
Engineering
Peking University

Date Approved: June 6, 2015

To my family and girlfriend!

ACKNOWLEDGEMENTS

TABLE OF CONTENTS

LIST OF TABLES

LIST OF FIGURES

LIST OF ABBREVIATIONS

ac	alternating current
AC	activated carbon
AEC(s)	aluminum electrolytic capacitor(s)
AFM	atomic force microscope
BLT	bond line thickness
$C"$	the imaginary component of capacitance
C_{areal}	areal capacitance
CD	charge/discharge
CDC	carbide-derived carbon
C_m	gravimetric capacitance
CNT(s)	carbon nanotubes
C_p	specific heat at constant pressure
CV	cyclic voltammetry
CVD	chemical vapor deposition
EIS	electrochemical impedance spectroscopy
EDLC	electrical double-layer capacitance
EDX	energy dispersive X-ray spectroscopy
ESR	electrochemical series resistance
f_0	frequency at -45 °
FTIR	Fourier transform infrared spectroscopy
GO	graphene oxide
HQ	hydroquinone

I$_D$	integrated intensity of D band in Raman spectra
I$_G$	integrated intensity of G band in Raman spectra
LFA	laser flash analysis
LSG	laser-scribed graphene
MLG	multi-layer graphene
MPD	*m*-phenylenediamine
MSC(s)	micro-supercapacitor(s)
NMP	N-methyl-2-pyrrolidone
OLC	onion-like carbon
OPD	*o*-phenylenediamine
PAP	*p*-aminophenol
PDMS	polydimethylsiloxane
PECVD	plasma-enhanced chemical vapor deposition
PET	polyethylene terephthalate
PMMA	poly-methyl methacrylate
PPD	*p*-phenylenediamine
PVA	polyvinyl alcohol
rGO	reduced graphene oxide
R_b	thermal boundary resistance
R_c	contact resistance
R_t	total thermal resistance
sccm	standard-state cubic centimeter per min
SEM	scanning electron microscope

SLG	single-layer graphene
TIM(s)	thermal interface material(s)
TSC(s)	traditional supercapacitor(s)
VACNT	vertically aligned carbon nanotube
VArGO	vertically aligned reduced graphene oxide
VG	vertically-oriented graphene
XPS	X-ray photoelectron spectroscopy
XRD	X-ray diffraction
Z'	the real component of resistance
Z''	the imaginary component of resistance
α	thermal diffusivity
η	Coulombic efficiency
κ	thermal conductivity
ρ	mass density
τ	pulse duration
τ_0	relaxation time constant
υ	scan rate
φ°	standard electrode potential
ϕ	diameter
ω	angular frequency of microwave

SUMMARY

Graphene is an outstanding candidate for electronics, energy storage and thermal interface materials because of its excellent electrical conductivity, extremely high specific surface area and superior in-plane thermal conductivity. However, it is difficult to utilize pristine single-layer graphene for industrial applications due to its limited yield and expensive price. Chemically functionalized graphene, especially reduced graphene oxide (rGO), retains part of these excellent properties. At the same time, it is available for mass production, which is promising for real applications. In our work, we focus on rGO-based supercapacitors and micro-supercapacitors (MSCs), flexible ac line-filters and vertically aligned thermal interface materials.

We first design a facile approach to investigate the role benzene derivatives play in the capacitance enhancement of graphene-based supercapacitors. In this work, graphene oxide (GO) is mixed with a specific benzene derivative, after which it is simultaneously reduced and assembled with a zinc plate at room temperature. This solid-phase room temperature reduction mechanism avoids those side reactions that may occur at elevated temperatures. Moreover, the non-covalent interaction helps to separate the contributions from the spacing effect and the pseudocapacitance effect. After investigating a series of similar benzene derivatives, the main reason is attributed to the pseudocapacitance of the aromatic molecules rather than the former one. Meanwhile, we find that the *para* and *ortho* substituted benzene derivatives contribute much more than the *meta* substituted ones. These conclusions will guide the search and design of promising aromatic molecules for high performance supercapacitors.

In addition, we fabricate an all-solid-state flexible MSC based on metal-reduced GO.

The as-prepared MSC shows a specific areal capacitance of 0.95 mF/cm^2 and maintains 98.3% of the initial capacitance after 11,000 times of charge/discharge cycles. In addition, a small relaxation time constant of 4.8 ms is achieved in gelled electrolyte, which indicates fast ion transfer mobility within the structure. Besides, the device also exhibits great flexibility which retains 93.5% of the capacitance after 2,500 times of bending and twisting. These properties make the as-fabricated MSC a promising energy storage candidate for wearable electronics.

Based on the work of MSC, we achieve a flexible ac line-filter that is suitable for mass production. Aqueous electrolyte is used in this device, which shows a phase angle of -75.4 °at 120 Hz with a specific capacitance of 316 μF/cm^2 and a RC time constant of 0.35 ms. In addition, it retains 97.2% of the initial capacity after 10,000 galvanostatic charge/discharge cycles.

Meanwhile, we produce a three-dimensional graphene/polydimethylsiloxane composite that gives a thermal resistance as small as 14 mm^{2}K/W, which is comparable to commercial products. What's more, a convenient transient program is developed to measure the thermal resistance. It saves much time compared with the steady-state method that generally consumes a lot of time for equilibrium. In addition, the non-contact attribute will avoid contamination to the equipment. This program is also applicable for measuring the contact resistance for thermal interface materials.

CHAPTER 1   INTRODUCTION

1.1 Graphene Structure and Properties

Graphene is a two-dimensional (2D) material that has attracted widespread attention in the past decade. It possesses outstanding electronic, optical, mechanical and thermal properties.[1-3] From the structure point of view, graphene is composed of single-layer sp^2 hybridized carbon atoms with a carbon-carbon bond of 1.42 Å. The structure is illustrated in Figure 1.1, which can be wrapped up into zero-dimensional (0D) carbon balls, one-dimensional (1D) carbon nanotubes (CNTs) or carbon nanorods and three-dimensional (3D) graphite.[3]

Graphene, as a pure 2D material that never naturally exists before, has a lot of bizarre properties. For example, graphene is a zero-bandgap semiconductor with dramatically different properties compared to its 3D form, namely graphite.[4] It also shows extremely high mobility that exceeds 15000 cm^2/Vs at room temperature. Theoretically it also has an electrical resistivity of as low as 10^{-6} Ω•cm, which is even better than the industrial standard silver.[1] Except for the excellent electrical properties, graphene also possesses an ultrahigh thermal conductivity of 4.8~5.3×10^3 W/mK, which is about five times the value of highly ordered pyrolytic graphite.[5] Meanwhile, graphene is also found to be the strongest material with a tensile strength of up to 130 GPa, a spring constant of 1~5 N/m and a Young's modulus of 0.5 TPa.[6] Another important property is the specific surface area (SSA). Graphene, as a single sheets of carbon atoms, has an extremely high surface area of 2675 m^2/g, which is promising for catalytic and

energy storage applications.[7]

1.2 Preparation of Graphene

Due to these outstanding properties, researchers have conceived a lot of interesting applications including field-effect transistors,[8, 9] transparent electrodes,[10-12] sensors [13, 14] and so on. However, there are still many barriers to be overcome before they can be used practically. One of the key issues is the production capacity.
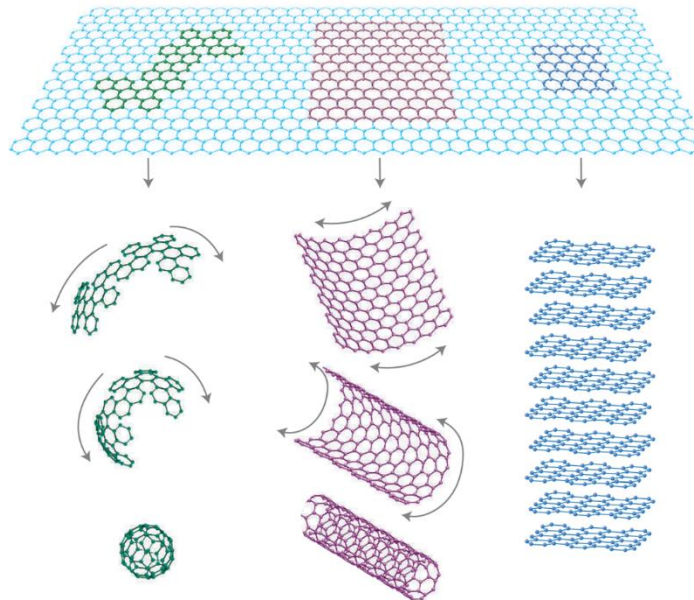
Figure 1.1 The structure of graphene. It is the building blocks of other carbon allotropes with different dimensions. For example, it can be wrapped up, rolled and stacked into fullerene, CNT and graphite.[3]

Historically, graphene is discovered with a scotch tape method that is able to produce high quality graphene with small grain size.[1] This kind of single-layer graphene (SLG) is highly crystalline and excellent for lab research. However, the yield is too low

and to be industrialized.[15, 16] From then on, different methods have been proposed towards the scalable production of graphene.

1.2.1 Exfoliation of Graphite

Exfoliation is one of the widely-adopted methods to produce graphene. In fact, the discovery of graphene, which is through successively peeling, is a kind of mechanical exfoliation method. However, the productivity of this scotch tape method is too limited to be industrialized. Solvent-assisted-sonication and shear-force-exfoliation are two of the scalable methods. For the solvent-assisted-sonication method, natural graphite powder is added into specific solvents with suitable surface energy, for instance N-methyl-2-pyrrolidone (NMP). The mixture is then ultra-sonicated for certain time, during which the solvent molecules intercalates into the graphite interlayers and separates the graphite sheets into graphene.[17-26] The other method utilizes the shear force in appropriate solvents to exfoliate graphene sheets from each other.[27, 28]

1.2.2 Epitaxial Growth and Chemical Vapor Deposition Method

Another kind of widely adopted method is the chemical growth method, especially epitaxial growth and chemical vapor deposition (CVD) growth. For example, ultrathin large-scale graphene is successfully grown on SiC substrate by epitaxial method.[29, 30] SLG and multi-layer graphene (MLG) are also grown via CVD methods on different metal substrates like Cu, Ni, etc.[12, 31-33]

1.2.3 Reduction of Graphene Oxide

The reduction of graphene oxide (GO) is a series of different methods. For this kind

of method, graphite is first oxidized into GO, which is readily dispersed into water in a single-layer or few-layer morphology due to the large amount of electro-negative hydrophilic function groups added onto the sheet in the oxidation process.[34, 35] These functional groups are removed during reduction. Different approaches have been used to prepare reduced graphene oxide (rGO), which can be generally categorized into thermal reduction,[36-42] hydrothermal reduction,[42-44] light reduction,[45-49] chemical reduction[34, 50-53] and electrochemical reduction methods.[54-58]

1.2.4 Comparison of Graphene obtained from Different Methods

We have categorized the sources of scalable production of graphene into three types, namely exfoliation of graphite, CVD grown and the reduction of GO. The exfoliation methods reserve the crystallinity of graphene to the largest extent from the quality point of view; while graphene produced from CVD methods generally shows inferior yet still much more crystalline structure than those produced with GO reduction methods. For the reduction methods, graphite layer is first oxidized with a lot of external function groups and defects added onto the carbon sheets. These function groups are removed during the reduction process, partially restoring the sp^2 structure of graphene. Unfortunately, many defects and exterior elements remain in the plane, which sacrifices some of the excellent properties of graphene.

The CVD methods give the best control of graphene structure on a variety of metal substrates. For example, SLG is easily grown on Cu substrate, which is widely used to investigate the properties of SLG. In addition, although exfoliated graphene reserves better graphene structure, the contamination solvent as well as the contact interfaces between graphene layers greatly reduce its performance. In many cases, CVD grown

graphene are much superior to the other two for large scale utilizations. For example, 30 inches CVD-grown SLG has been used as transparent electrodes.[12]

However, from the yield point of view, GO reduction methods are the one most suitable for mass production. All the involved procedures are wet-chemistry processed, which are readily available for scalable production. Thousands tons of GO are produced every year, orders of magnitude more than those obtained with other methods. The exfoliation methods, if appropriate solvents are chosen, can also produce large quantities of MLGs cost-effectively. The CVD methods, however, is less productive than the other two kinds of methods. It is highly dependent on the quantities of the metal substrates.

Except for the yield, there are also some other benefits of the GO reduction methods. One of them is the plenty of choices for chemical functionalization due to the various function groups on the GO plane. For example, rGO has been used for controlled loading and targeted delivery of anti-cancer drugs.[59-61] Besides, it also shows extremely large SSA and total surface area. The SSA for graphene itself is 2560 m2/g. However, only a small portion of this value is accessible due to the Van der Waals force induced aggregation between the graphene layers. On the contrary, GO is easily dispersed in solution because of the negatively charged attribute and the accompanied electrical repulsion force between the layers. A great extent of the surface area is maintained in this way, which is critical for the applications requiring a large amount of surface area. Two of the fields are electrochemical capacitors and catalytic applications.[62-65]

1.3 Research Objectives and Challenges

There are a lot of applications for graphene due to its excellent properties. We

choose three of these important fields, including electrochemical capacitors, ac line-filters and graphene-based thermal interface materials (TIMs). In our study, we want to find out the mechanisms for the observed phenomenon and guide the development of feasible applications.

1.3.1 Graphene/Electrochemical Benzene Derivatives-Based Electrochemical Capacitors

Electrochemical capacitors, also known as supercapacitors due to their extremely large capacitance compared with traditional ones, are an energy storage unit widely used as emergency power supplies. For better performance, the electrode materials should be highly conductive with a large surface area available to the electrolyte. Currently activated carbon (AC) is used as the commercial product for this purpose. Graphene, a 2D material, shows a SSA of as high as 2560 m^2/g and an electrical conductivity comparable to that of silver. As a result, it has been extensively investigated since its discovery.

There are two different types of supercapacitors, the electrical double-layer capacitors (EDLCs) and the pseudocapacitive capacitors. The former type stores the electrical energy as a kind of physical capacitor; while the latter one is more of a chemistry energy unit, in which the energy is stored within the redox reactive chemicals.

The schematic illustration of EDLCs is presented in Figure 1.2.[66] During charging, the positive electrode is charged to a higher potential than the negative electrode. As a result, the negative ions in the electrolyte are attracted to the surface of the positive electrodes and vice versa. A small gap exists between the electrode surface and the attracted ions, typical in the order of angstroms, and forms a capacitor prototype, by

which the electrical energy is stored.

Theoretically graphene has an extremely large gravimetric capacitance of 550 F/g. However, the actual results obtained from literature generally range between 100 and 200 F/g, the reason of which is often attributed to the aggregation caused by the attractive Van der Waals force between the graphene layers. Two kinds of approaches have been used to resolve this problem. One is through the increase of SSA accessible to the electrolyte, with specific capacitances reported ranging from 150 to 450 F/g.[67-71] The other is through the incorporation of electrochemically active materials, such as metal oxides,[72, 73] conducting polymers[74, 75] and small aromatic chemicals.[76-78] Electrochemically active benzene derivatives have attracted much attentions among these materials. However, the roles these benzene derivatives play remain unclear.

We designed an approach based on metal-reduction of GO to study the capacitance contribution. In this work, GO is mixed with specific benzene derivative and reduced with a zinc plate at room temperature. The room temperature solid-phase reduction mechanism avoids the side reactions that may occur at elevated temperatures. Moreover, the interaction is non-covalent, which helps separate the contributions from the spacing effect and the pseudocapacitance effect. By investigating the performance a series of similar benzene derivatives/rGO electrodes, we want to find whether the capacitance increase arises from the pseudocapacitance or their spacing effect.

1.3.2 Graphene-Based Alternating Current (ac) Line-Filter

Ac line-filter is a device used to smooth the leftover ac ripples on direct current (dc) voltage buses for many line-powered devices. The mechanism of ac line-filtering is shown in Figure 1.3. First, the frequency of the ac power is multiplied with four diodes

7

(Figure 1.3a and b). This signal is then smoothed with an ac line-filter that will greatly increase the dc component. The red curve shown in Figure 1.3c represents a smoothed ac signal that is very similar to dc signal. Figure 1.3d shows an actual ac line-filter, in which the capacitor is generally the bulkiest component.

Like shown in Figure 1.3d, a bulky capacitor is generally used in ac line-filtering devices to execute the smoothing purpose. Currently, aluminum electrolytic capacitors (AECs) are widely used for this purpose because of their low cost and moderate capacitance. For pure capacitors, the phase angle between voltage and current is -90 ° at 120 Hz. AEC can provide an extremely large phase angle of ~ -84 ° at this frequency. However, they are usually the bulkiest component in electronic devices, which is more and more incompatible with the trend of miniaturization in portable and wearable electronics.
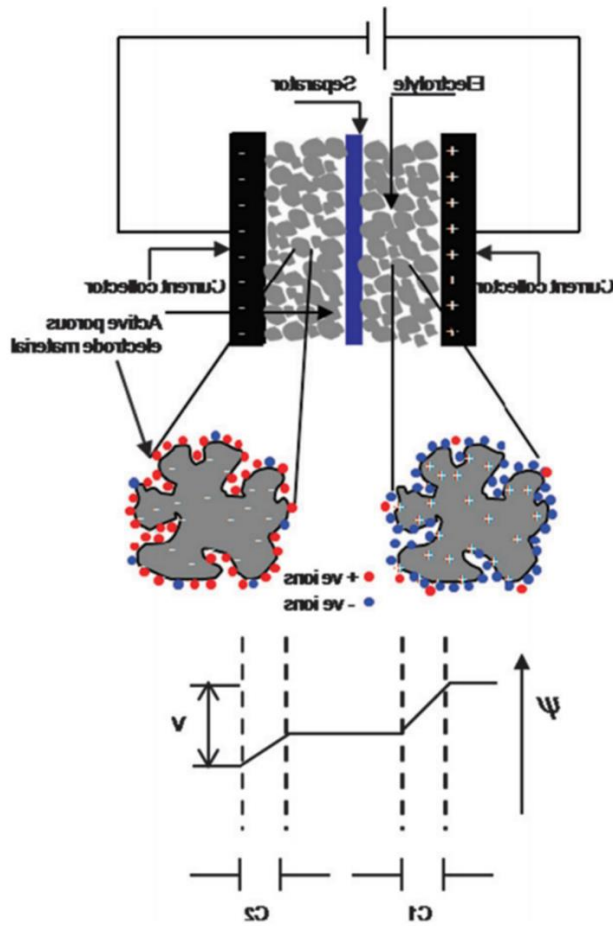
Figure 1.2 Schematic representation of an EDLC based on porous electrode materials.[66]

EDLC-based supercapacitors may help solve this problem due to their extremely large capacitance. However, their frequency response needs to be greatly improved. Graphene, with its extremely large SSA and excellent electrical conductivity, is a promising material for this purpose. Some novel graphene-based devices have been designed with competitive performance to those of AECs.[46, 49, 79-83] For example, ac line-filters based on vertically oriented graphene (VG) sheets,[81] graphene/vertically aligned carbon nanotube (VACNT) arrays[82] and electrochemically reduced GO[82] are fabricated with phase angles ranging from -81.5 ° to -84 ° at 120 Hz.
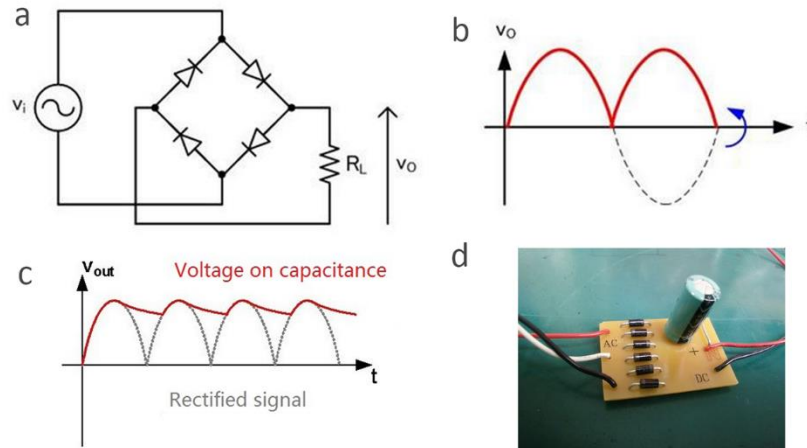
Figure 1.3 Schematic illustration of ac line-filters. (a) An ac power supply is converted with four diodes, exporting an external voltage with double frequency. (b) The sketch of phase conversion and the accompanied frequency multiplication. (c) The converted sinusoidal signal is smoothed with an ac line-filter, outputting a dc signal. (d) An actual ac line-filter.

Unfortunately, most of these devices utilize expensive approaches that are impractical for mass production. In addition, the high temperature involved in the process is incompatible with flexible electronics. We want to design a cost-effective graphene-based ac line-filter using a wet chemical method. In this approach, Cu-reduced GO is used as the electrode material while an interdigitated design is adopted to improve the frequency response. This method is also compatible with flexible electronics since it is fabricated at room temperature.

1.3.3 Graphene-Based TIMs

The electronic market is growing rapidly in the past decades. Meanwhile, the number of transistors in a processor doubles every two years according to Moore's law, which results in an intimidating number of 15 billion in 2015.[84] The growing packing density of transistors will not only increase the capability of a chip, but also the waste

10

heat generated during operation. High temperature and rapid change of temperature will increase the possibility of thermal failure, which is detrimental to the lifespan of electronic devices.

The heat generated in the chip should be conducted to heat sinks and dissipate away. Unfortunately, a high thermal resistance usually exists at the contact interface of two solid surfaces, resulting in poor heat conduction. A good TIM is needed to help alleviate this issue.
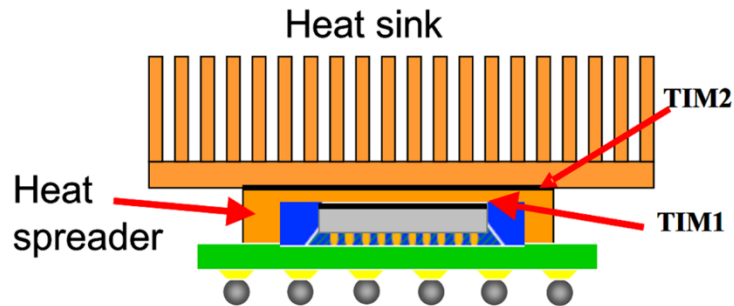
Figure 1.4 Schematic illustration of TIM architecture in flip-chip technology.[85]

Figure 1.4 illustrates the configuration of a simple flip-chip package.[85] Two TIMs are used in this architecture, in which TIM 1 conducts the heat from the backside of the chip to the cap of the heat spreader; while TIM 2 conducts it further to the external heat sink. For an ideal TIM, it should not only have excellent thermal conductivity but also small contact thermal resistance with substrates. Most researches focus on the investigation of TIM 1, which is also the case in our research.

A lot of materials have been studied and commercialized, including thermal greases,[86-89] phase change materials,[90-95] solders[96-100] and thermally conductive

composites,[101-105] most of which compose a polymeric matrix filled with thermally conducive fillers. Thermal greases are cost-effective materials with high thermal conductivity and low thermal stress due to their high compliance. However, dry-out and pump-out issues impair their reliability. Phase change materials offer better stability yet higher viscosity and lower thermal conductivities. Low melting temperature solders provide higher conductivity yet worse thermal stress and corrosion performance. Thermally-conductive composites are easy to handle and resistive to harsh environments and pump-out problems. They also conform to the surface due to the low viscosity. Their drawback is the relative more expensive cost, lower thermal conductivity and the vulnerability to delamination failure.

We want to design a novel graphene-based 3D graphene/polydimethylsiloxane (PDMS) composite and test its performance as a TIM. For most of the literatures, only the thermal conductivity is measured without mention the performance of contact resistance. This is not thorough for the characterization of a TIM. Previously we have shown that our 3D graphene/PDMS composite has a moderate thermal conductivity of 0.56 W/mK.[106] We want to find out whether it can also provide sound total thermal resistance as a practical TIM.

In addition, the test for contact resistance is often tedious for steady-state methods, wasting a lot of time and energy. Here we want to design a non-contact transient method based on laser flash analysis (LFA). This method directly gives the total thermal resistance, which can also be developed to accommodate the contact thermal resistance.

CHAPTER 2   GRAPHENE-BASED SUPERCAPACITORS ENHANCED WITH ELECTROACTIVE BENZENE DERIVATIVES

2.1 Introduction

Supercapacitors have been considered as a promising energy storage unit for portable electronics, electric vehicles, etc. due to their high power density and long lifetime.[107] Various materials have been investigated as the active electrode, such as metal oxides,[72, 73] conducting polymers,[74, 75] AC,[108] CNTs,[109] graphene derivatives[110, 111] as well as the hybrids of them.[73, 112] Among all these materials, rGO is most extensively studied because of its extremely high SSA, good electrical conductivity and the capability for large-scale production.[62, 63] However, the specific capacitance reported for graphene (~ 100 to 200 F/g) is much smaller than the theoretical value (~550 F/g).[113] This deficiency largely results from the aggregation of graphene sheets caused by the Van der Waals force, which greatly reduces the surface area accessible to the electrolyte and thus decreases the specific capacitance.

Generally two approaches have been used to improve the capacitance performance of graphene-based materials. The first one is through the modification of rGO morphology to increase the surface area accessible to the electrolyte. For example, curved graphene that alleviates the aggregation during sample preparation was prepared by anti-solvent[67] or fast-solvent-evaporation treatment.[68] In addition, different types of spacers, such as $Mg(OH)_2$,[69] CNTs[70] and covalently-grafted benzene molecules,[71] were introduced to increase the spacing between the rGO sheets. Gravimetric

13

capacitances ranging from 150 to 450 F/g are achieved by these methods. The second approach is through the incorporation of electrochemically active materials that provide large pseudocapacitance via redox reactions, such as metal oxides,[72, 73] conducting polymers[74, 75] and small aromatic chemicals.[76-78] Among these materials, electrochemically active benzene derivatives have attracted lots of attentions. For example, Xu et al. incorporated hydroquinone (HQ) and achieved a specific capacitance of 441 F/g.[76] Lu et al. reported a specific capacitance of 313 F/g with *p*-phenylenediamine (PPD)/rGO hybrid electrode, of which the improvement was attributed to spacing and nitrogen doping effect.[77] Cui et al. investigated 1,2,4,5-benzenetetraamine grafted rGO and obtained a specific capacitance of 370 F/g.[78] These benzene derivatives are very promising because of their large capacitance and ease of production. However, the roles of these benzene derivatives remain unclear. The puzzle becomes more complicated when the reactions occur at elevated temperatures, which may introduce byproducts into the system.[76-78, 114]

Herein we design a facile approach to study the capacitance contribution from electrochemically active benzene derivatives. In this work, GO is mixed with a specific benzene derivative, after which it is simultaneously reduced and assembled onto a zinc plate at room temperature. The benzene

derivative molecules are physically adsorbed on the rGO layers in a face-to-face fashion via π-π interaction. The solid-phase room temperature reduction process avoids the side reactions that may occur at elevated temperatures. Moreover, the interaction between benzene derivatives and rGO is non-covalent, which helps to separate the contributions from spacing effect and pseudocapacitance effect. By investigating the

performance a series of similar benzene derivatives/rGO electrodes (*b*-rGO, in which *b*-stands for benzene derivatives) including phenol, aniline, HQ, *p*-aminophenol (PAP), *o*-phenylenediamine (OPD), and *m*-phenylenediamine (MPD), we find that the capacitance increase mainly arises from the pseudocapacitance of specific benzene derivative molecules rather than their spacing effect. With a small loading of PPD, a gravimetric capacitance of 273 F/g and capacitance retention of 86% after 10,000 charge/discharge cycles are achieved.

2.2 Experimental and Methods

2.2.1 Preparation of GO

GO was synthesized according to a modified Hummers' method.[115, 116] Briefly, $NaNO_3$ (4 g) was dissolved into concentrated H_2SO_4 (98 wt%, 200 mL) in an ice bath. Graphite powder (Asbury 230U, 4 g) and $KMnO_4$ (18 g) were slowly added into the solution with the temperature kept below 8 ℃. The mixture was vigorously stirred for 2 h in the ice bath and another 30 min in a 35 ℃ water bath. After the reaction, the solution was diluted with deionized water (500 mL) followed by the addition of H_2O_2 (30% w/w in H_2O, 50 mL), during which the temperature was maintained below 80 ℃. The as-obtained GO was washed with HCl (1 M, 2 L) and deionized water repeatedly until the pH reached 6.

2.2.2 Preparation of rGO, *p*-rGO, Hydrothermal *p*-rGO and *b*-rGO

GO (1 mg/mL, 40 mL) was first dispersed in water and ultrasonically exfoliated for 30 min. Benzene derivatives such as phenol, aniline, HQ and PAP, PPD, OPD or MPD

(0.36 mM if not stated otherwise) was added into the solution and ultrasonicated for another 30 min. In this process the aromatic molecules dissolved in the GO solution and attached onto the GO surface. After that a Zn plate (4 cm $\times$ 4 cm) was immersed into the GO solution at ambient temperature and GO was thus reduced into rGO hydrogel. The as-prepared b-rGO hydrogel film was removed from the substrate by immersion in a dilute HCl solution for about 30 min, after which it was washed with excess amount of dilute HCl for 1 h and 10 L deionized water for two days to remove the Zn residues and non-adsorbed aromatic molecules.

For hydrothermally prepared p-rGO, GO (15 mg) was first dispersed in water (15 mL) and ultrasonically exfoliated for 30 min. Then PPD (15 mg) was added into the solution and ultrasonicated for another 30 min. After that the vial was placed in an oil bath (90 ℃, 30 min) and a cylinder rGO hydrogel was formed. The as-prepared p-rGO hydrogel was washed with 10 liters of deionized water to remove the non-adsorbed PPD molecules.

2.2.3 Structural Characterization

The morphologies of GO, rGO and PPD/rGO (p-rGO) were characterized with scanning electron microscope (SEM, Hitachi SU8010) and atomic force microscope (AFM, Dimension Edge, Veeco with silicon tip MPP-11100-10). Raman spectra were taken with LabRAM ARAMIS, HORIBA JOBIN YVON using 532 nm laser as the excitation light. X-ray photoelectron spectroscopy (XPS) measurement was performed with a Thermo K-Alpha XPS. Fourier transform infrared spectra (FTIR) were obtained with FTIR spectrometer (Nicolet, Magna IR 560) at room temperature. X-ray diffraction (XRD) was performed with an X'Pert Pro Alpha-1 machine with Cu Kα radiation.

2.2.4 Electrochemical Measurements

Two-electrode and three-electrode test setups were used to test the electrochemical performance. For the two-electrode test setup, a regular filter paper was sandwiched between two circular hydrogels as the separator (ϕ=1.0 cm, loading ~ 1 mg/cm^2). The sandwiched structure was kept between two stainless steel plates that serve as the current collector. For the three-electrode test setup, a platinum wire and Ag/AgCl electrode filled with saturated KCl aqueous solution were used as the counter and reference electrode, respectively. A rectangular hydrogel (0.5 cm $\times$ 2 cm) was pressed onto a gold foil with a piece of carbon fiber paper to improve their contact. 1 M H$_2$SO$_4$ was used as the electrolyte throughout this work. Before test, the samples were soaked into the electrolyte for 3 h. Cyclic voltammetry (CV), galvanostatic charge/discharge test (CD) and electrochemical impedance spectroscopy (EIS) were carried out with a Versastat 2-channel system (Princeton Applied Research). EIS was carried out in the frequency range of 0.01 Hz to 100 kHz with a 10 mV sinusoidal voltage.

2.2.5 Calculations

2.2.5.1 Specific Capacitance

For three-electrode configuration, the specific capacitance derived from the galvanostatic discharge curve is calculated by $C = \frac{i\Delta t}{m\Delta V}$, where i is the discharging current, Δt is the discharging time, ΔV is the voltage range and m is the weight of the rGO hydrogel. Specific capacitance derived from CV curves follows $C_m = \frac{\oint i dV}{2m\Delta Vv}$, where i is the current, V is voltage, m is the weight of the rGO electrode, ΔV is the voltage range

(0.8 V) and ν is the scan rate. Integration is carried out over a whole cycle of the CV curve.

For two-electrode configuration, the specific capacitance derived from the galvanostatic discharge curves is calculated with $C = \frac{4i\Delta t}{m\Delta V}$, where i is the discharging current, Δt is the discharging time, ΔV is the voltage range and m is the total weight of both rGO hydrogels. Specific capacitance derived from CV curves follows $C_m = \frac{2\oint idV}{m\Delta V\nu}$, where i is the current, V is voltage, m is the total weight of both rGO electrodes, ΔV is the voltage range (0.8V) and ν is the scan rate. Integration is carried out over a whole cycle of the CV curve.

2.2.5.2 PPD loading estimation

The loading of PPD is estimated according to the XPS survey spectrum of *p*-rGO. The atomic ratio obtained from XPS survey is 82.8:14.3:2.9 for C:O:N. It is reasonable to assume that all the nitrogen element comes from that PPD since the GO sheets does not show any nitrogen peak. The element contribution (C:N:O) from rGO and PPD in *p*-rGO is 74.1:14.3:0, and 87:0:29, respectively. Based on these data, the weight ratio of PPD to rGO is 1.0:7.7, corresponding to a PPD loading of about 11 wt%.

2.3 Results

Active metals such as zinc, iron and copper, can reduce due to their lower redox potentials.[57, 58] Here Zn plate is used as the reducing agent and PPD is used as a representative of these benzene derivatives. The reduction process is illustrated in Figure 2.1. Due to its higher redox potential, the GO sheet will be spontaneously reduced once it

contacts the Zn plate. The as-reduced GO is electrically conductive, which in turn serves as the conducting path for electrons and results in the continuous reduction and assembly of GO sheets.
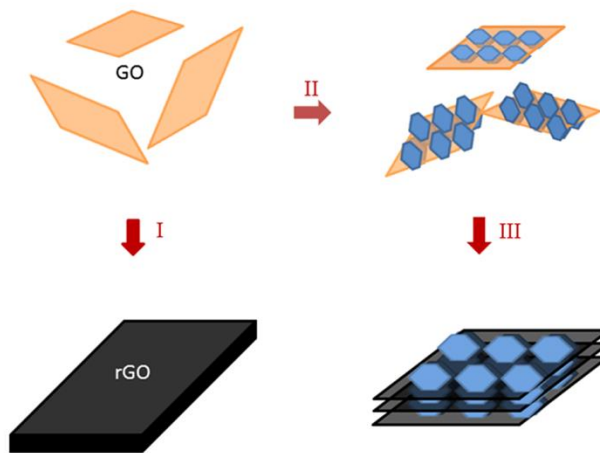
Figure 2.1 Schematic illustration of the fabrication of rGO and b-rGO. Step I: The reduction; step II: Mixing GO solution with benzene derivatives; step III: The mixture of GO and benzene derivatives is reduced with Zn substrate.

Figure 2.2 presents the photos of 1 mg/mL GO solution with (right) and without (left) the addition of PPD. Both samples had been left for 24 h before these photos were taken and neither of them showed any sign of agglomeration. The stable dispersion results from the electric repulsion force between the negatively charged GO sheets.[117] Meanwhile, the addition of PPD does not disturb the stability, indicating PPD does not interact the electronegativity of GO.

The SEM images of rGO (Figure 2.3a) and p-rGO (Figure 2.3b) exhibit a similar open-porous structure that reflects the layer-by-layer reducing mechanism. In addition, it also helps the ion transport within the electrode, which is beneficial for the

electrochemical performance.[57] This simple reducing method takes place at room temperature and uses solid phase reducing agent. As a result, it avoids the side reactions that may occur at elevated temperatures or by using liquid reducing agents, making it excellent for studying the function of these benzene derivatives.[114]
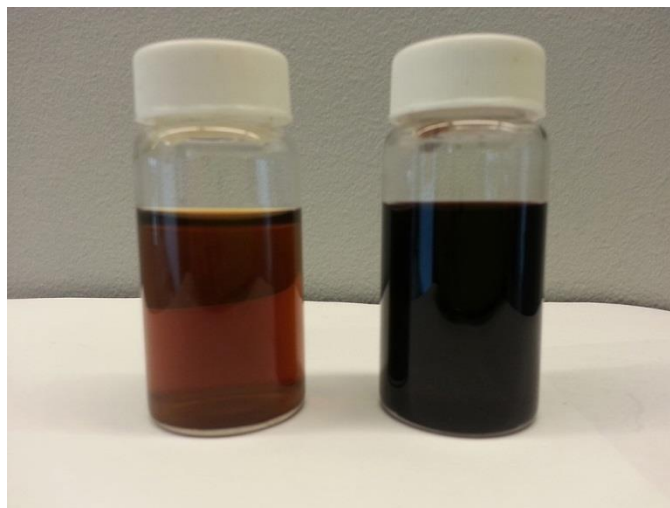
Figure 2.2 Optical images of GO and GO/PPD solution. Left: GO solution; right: GO/PPD solution. Both samples were left for one day before the images were taken.
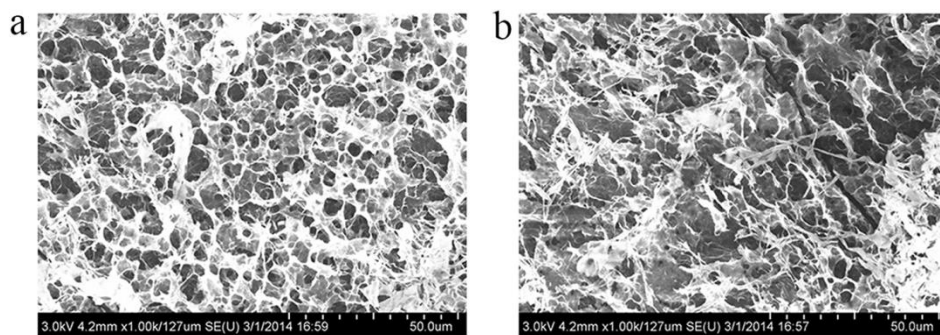
Figure 2.3 SEM images of freeze-dried rGO (a) and *p*-rGO (b) aerogel, respectively.

The morphology of GO and rGO after the PPD absorption is characterized by AFM and XRD, respectively. From the AFM images, the thickness of GO is measured to be 0.9 nm (Figure 2.4a), which increases to 1.6 nm after the attachment of PPD (Figure 2.4b). Figure 2.4c shows the XRD patterns of GO and rGO reduced with Zn plate. A sharp peak appears at 10.2 ° for GO, corresponding to an inter-layer spacing of 0.87 nm. The peak shifts to 23.4 ° after reduction, which corresponds to an inter-layer spacing of 0.38nm. For p-rGO, a distinct new peak shows up at 9.5 °, which does not exist in the XRD patterns of either rGO or PPD (Figure 2.4d). This peak corresponds to a spacing of 0.93 nm, 0.57 nm larger than that of the graphitic peak (0.36nm). The height increase from AFM and XRD characterization is equivalent to twice the thickness of the aromatic core.[75, 118] It thus indicates that the PPD molecules may attach parallel onto both sides of GO surfaces. The small difference between PPD/GO (0.7 nm) and p-rGO (0.57nm) can be attributed to the restoration of π-conjugation and the accompanied stronger interaction between rGO and PPD molecules.
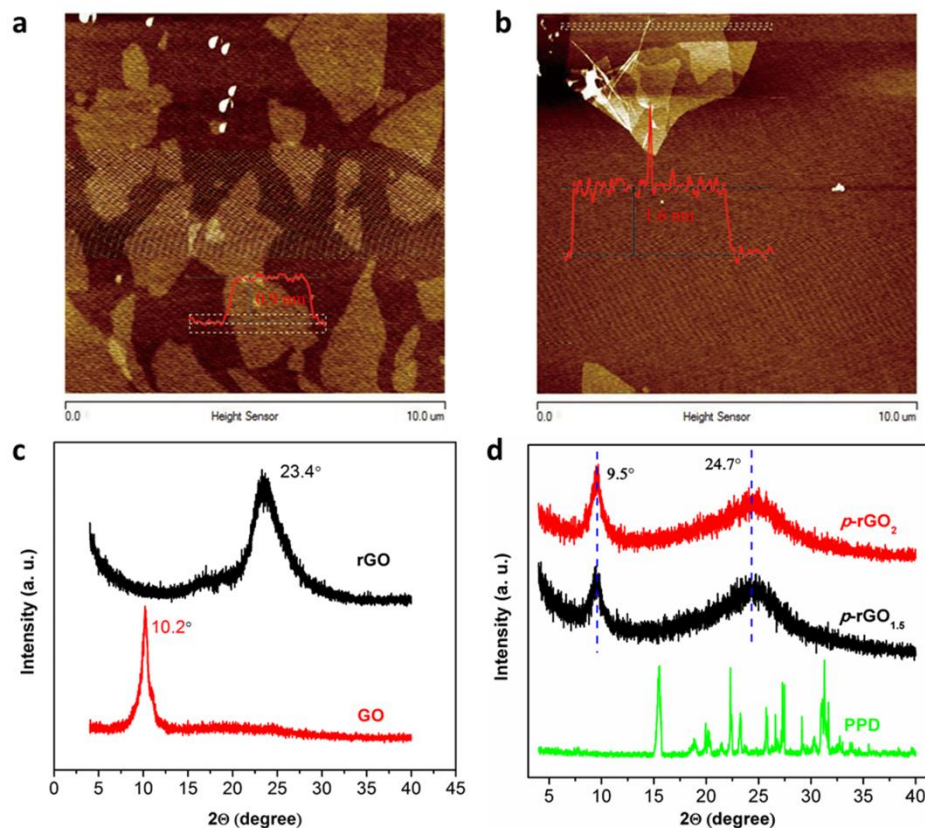
Figure 2.4 (a,b) AFM images of GO and PPD/GO, respectively. (c) XRD patterns of GO and rGO. (d) XRD patterns of PPD and *p*-rGO. The subscript designates the weight ratio of PPD-to-GO.

The interaction between PPD and rGO is shown to be non-covalent by chemical analysis. The XPS survey of p-rGO shows a small N1s peak from the residue of PPD molecules at 400 eV (Figure 2.5a). It thus proves the existence of PPD molecules even after prolonged washing. The strong adsorption should arise from the interaction between graphene and the benzene derivatives. The deconvoluted N1s spectrum (Figure 2.5b) contains a single peak centered at 399.5 eV, corresponding to the amine group in PPD.[119] Neither pyridinic nitrogen (398.2 eV) nor graphitic nitrogen (401.3 eV) shows up in the spectrum.[71, 119]

Figure 2.6a presents the deconvoluted C1s XPS spectra for GO, rGO and *p*-rGO. The rGO shows three distinct peaks at 284.6 eV, 286.0 eV and 288.5 eV, corresponding to C-C, C-O and C=O bonds, respectively. The peak intensity of C-O bond sharply decreases after GO is reduced by Zn. In addition, the C/O ratio increases from 2.4 for GO to 6.4 for rGO and 5.2 for *p*-rGO, suggesting an efficient removal of oxygen during this process. The similar C/O ratio found in rGO and *p*-rGO indicates that the addition of PPD does not affect the reduction process significantly. The Raman spectra of GO, rGO and *p*-rGO (in Figure 2.6b) show two characteristic peaks at 1342 cm^{-1} and 1577 cm^{-1}, corresponding to D and G bands of graphene, respectively. The I_D/I_G ratio increases from 1.0 of GO to 1.6 and 1.3 of rGO and *p*-rGO after the Zn-assisted reduction. This increase is attributed to the restoration of small graphene domains, a widely observed phenomenon for GO reduction.[120]
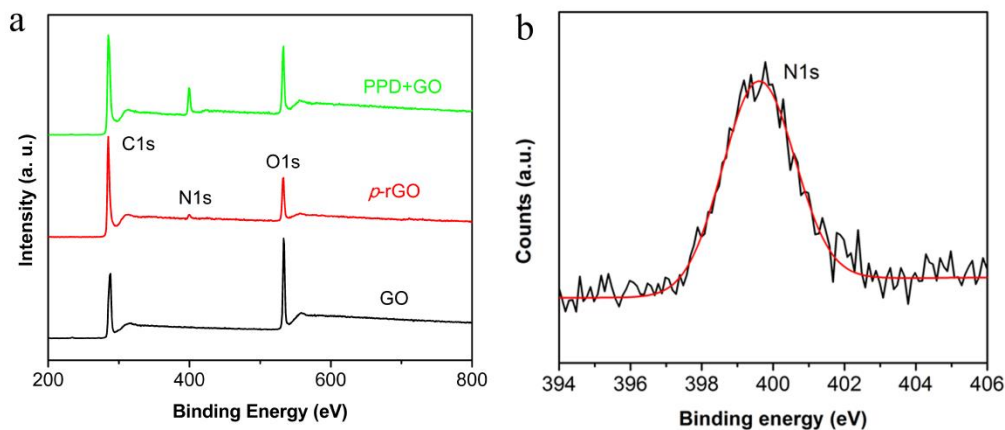
Figure 2.5 (a) XPS survey spectra of GO, *p*-rGO and PPD/GO. (b) N1s spectrum of *p*-rGO.
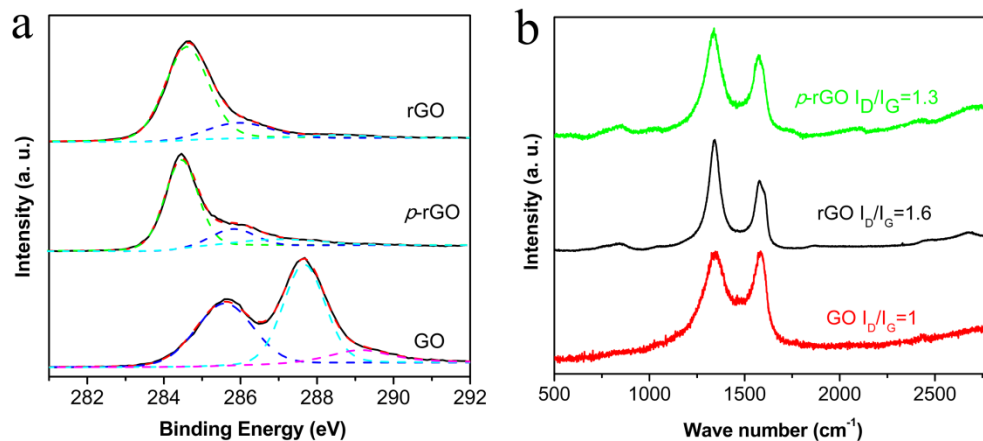
Figure 2.6 (a) C1s spectra of GO, rGO and *p*-rGO. (b) Raman spectra of GO, rGO and *p*-rGO.
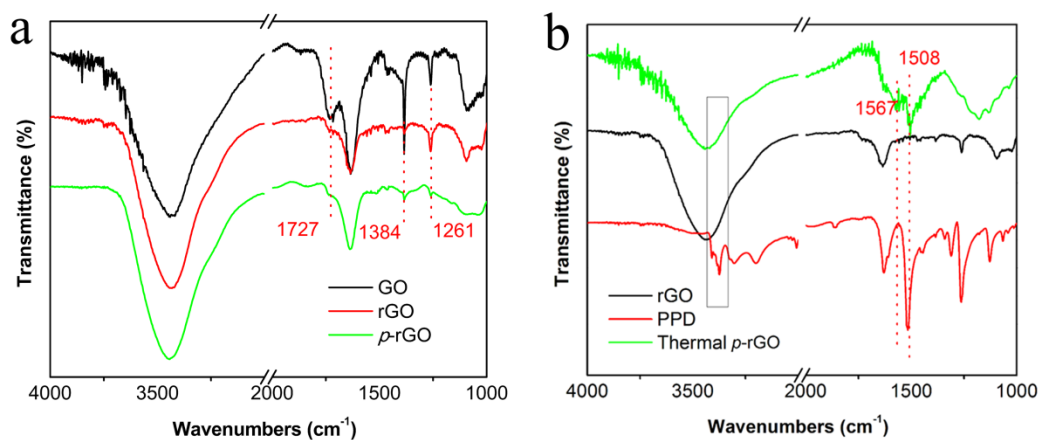
Figure 2.7 (a) FTIR spectra of GO, rGO and *p*-rGO. (b) FTIR spectra of rGO, PPD and *p*-rGO synthesized by hydrothermal method.

Figure 2.7a shows the FTIR spectra of GO, rGO and *p*-rGO. The peak intensities at 1727 cm^{-1} (C=O), 1384 cm^{-1} (O-H) and 1261 cm^{-1} (epoxy group)[119] of rGO and *p*-rGO are significantly smaller than those of GO, which also proves the successful reduction. The spectrum of *p*-rGO is nearly identical to that of rGO reduced by Zn. It thus implies that the PPD molecules do not react with GO or rGO in the presence of Zn at room

24

temperature. As a comparison, a control sample is prepared by hydrothermal treatment of GO with the addition of PPD. A distinct new peak at 1567 cm^{-1} appears in the FTIR spectrum, corresponding to the formation of a new N-H bending vibration that does not exist in either p-rGO or PPD itself (Figure 2.7b).[69, 71] It means that the hydrothermal method will generate new products while the room temperature reduction with Zn plate won't. In conclusion, these characterizations reveal that the PPD molecules remain after the reduction and washing process, during which they do not react with either GO or rGO.

From the characterizations above, we believe that PPD molecules are adsorbed face-to-face onto the rGO sheets via a non-covalent interaction. It is suggested that graphene interacts with benzene and other similar π-conjugated molecules via π-π interaction and amino/hydroxyl substitution will increase this interaction.[75, 76, 121, 122] We propose this adsorption arises from this π-π interaction, which is also supported with our characterization. Meanwhile, the PPD/GO dispersion in water is very stable, which is opposite to the rapid agglomeration caused by the electric attraction between oppositely charged materials.[69] As a result, the electric interaction is also excluded in our case.

2.4 Discussion

2.4.1 Electrochemical Test of rGO and p-rGO

Electrochemical characterizations are carried out with a two-electrode test setup.[123] Figure 2.8a shows the CV curves for rGO and p-rGO at a scan rate of 2 mV/s. The specific capacitance calculated based on the CV curves increases from 113 F/g for rGO to 273 F/g for p-rGO. Figure 2.8b represents the CD plots of p-rGO at different current

density. The linear and symmetric CD curves give a Coulombic efficiency of 97.5% and indicate excellent charge storage reversibility.

In addition, the *p*-rGO exhibits excellent rate performance. The capacitance at a discharge current density of 16 A/g is 242 F/g, which retains 93.6% of the value (259 F/g) at 0.6 A/g (Figure 2.9a). The superior rate behavior can be attributed to the conductive open-porous rGO hydrogel structure as well as the extremely short electron path of the face-to-face attaching mechanism. The hybrid electrode also shows excellent stability; it retains 86% of the initial capacitance after 10,000 cycles in the CD test at a current density of 11.9 A/g (Figure 2.9b). This capacitance retention is much better compared to those incorporated with metal oxides (84% after 1,000 cycles)[73] and conducting polymers (70% after 1,000 cycles).[74]
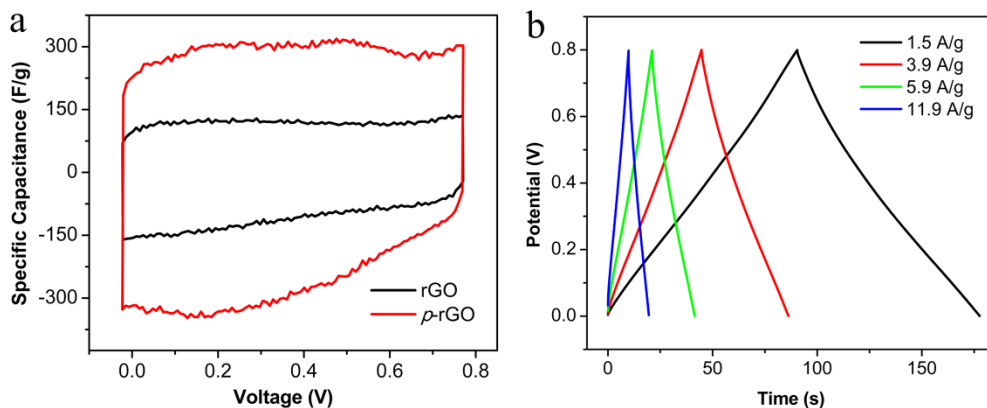
Figure 2.8 Electrochemical performance of the rGO and *p*-rGO electrodes in 1 M H_2SO_4 aqueous electrolyte. (a) CV curves of rGO and *p*-rGO at a scan rate of 2 mV/s. (b) CD curves of *p*-rGO at charge/discharge current of 1.5, 3.9, 5.9 and 11.9 A/g.
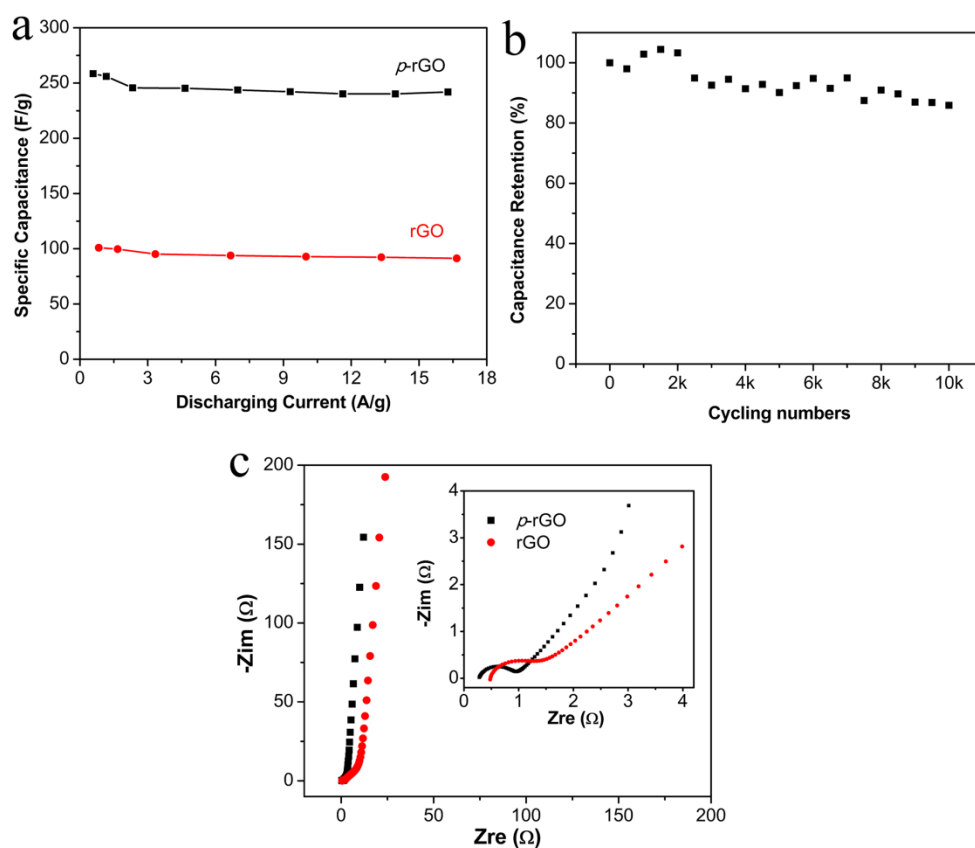
Figure 2. 9 Electrochemical performance of the rGO and *p*-rGO electrodes in 1 M H_2SO_4 aqueous electrolyte. (a) Specific capacitance of rGO and *p*-rGO at different current densities. (b) Cycling stability of *p*-rGO electrode at a current density of 11.9 A/g. (c) Impedance spectra of rGO and *p*-rGO. The inset shows the part of spectra at high frequency region.

The impedance spectroscopy is also tested for rGO and *p*-rGO (Figure 2.9c). Both spectra are nearly perpendicular to the real axis at the low frequency region, which indicates pure capacitive behavior and confirms excellent ion transport within the electrode materials.[57, 108] The electrochemical series resistance (ESR), estimated from the intercept of the impedance spectrum at low frequency region with the real axis, is comparable for rGO (4.1 Ω) and *p*-rGO (3.0 Ω). At high frequencies, there's a loop

corresponding to a nano-porous structure within both rGO and *p*-rGO.[108] The small internal resistance for *p*-rGO (0.28 Ω) also confirms the excellent electrical conductivity with the presence of PPD.

2.4.2 Mechanism Study

A series of benzene derivatives are incorporated into rGO following the same procedure as *p*-rGO to investigate the role these chemicals play in the capacitance enhancement. The specific capacitances are measured using a three-electrode setup, in which the redox reactions can be closely monitored by the corresponding pseudocapacitive CV peaks.

2.4.2.1 the Pseudocapacitance of the Electrochemically Active Benzene Derivatives Increased the Capacitance instead of the Spacing Effect

We firstly compared *mono*-substituted benzene (phenol and aniline) and *bi*-substituted benzene (HQ, PAP and PPD). All of these aromatic molecules improve the specific capacitance to some extent. However, the CV curves for *mono*-substituted benzene treated rGO (*mono*-rGO) show similar shapes and areas to that of pure rGO (Figure 2.10a); whereas those for *bi*-substituted benzene treated rGO (*bi*-rGO) exhibit new pseudocapacitive peaks (Figure 2.10b). The specific capacitance are 143, 128, 210, 160 and 211 F/g for the as-prepared electrodes incorporated with aniline, phenol, PPD, HQ and PAP, respectively. The capacitance enhancement with *mono* molecules is generally less than 30 F/g from that of rGO (115 F/g), while those for *bi*-rGOs are much larger (~100 F/g).
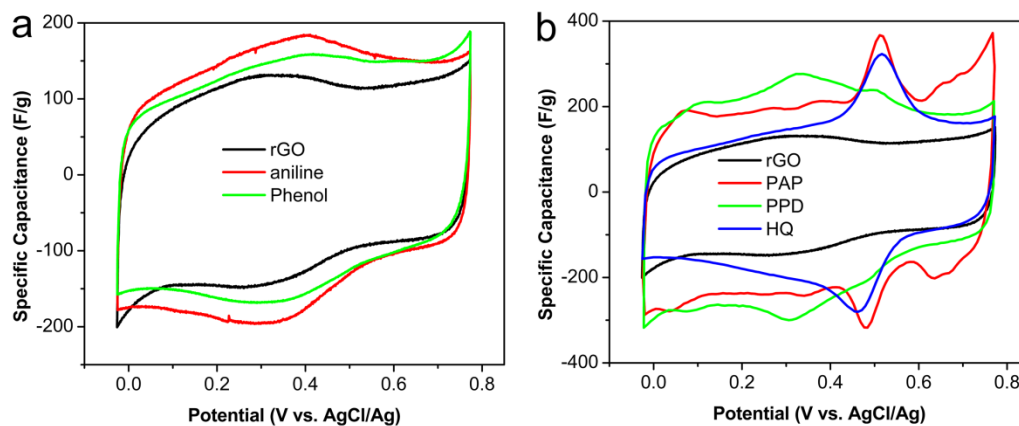
Figure 2.10 CV curves of (a) rGO, *aniline*-rGO, *phenol*-rGO and (b) rGO, *p*-rGO, *PAP*-rGO and *HQ*-rGO at a scan rate of 10 mV/s in 1 M H_2SO_4 aqueous electrolyte.

2.4.2.2 the Pseudocapacitance comes from the para and ortho Configuration

Mono- and *bi*-substituted benzenes have similar chemical structures with an aromatic core in the center that provides the adsorption force onto the graphene sheets. As a result, the specific capacitance for *mono*-rGO and *bi*-rGO should be comparable if the enhancement primarily comes from the spacing effect of the aromatic core. However, this expectation is contrary to the much smaller enhancements for *mono*-rGOs than for *bi*-rGOs. Moreover, characteristic pseudocapacitive peaks show up in the CV curves for *bi*-rGOs, indicating the occurrence of redox reactions. Therefore, we believe that these redox reactions, which only occur when two functional groups are present in a benzene ring, are the major contributors for the large enhancement.

It is known that there is a simple two-electron redox reaction between quinone and HQ.[124] We suggest that the capacitance increase primarily arises from similar redox reactions as shown in Figure 2.11.

29
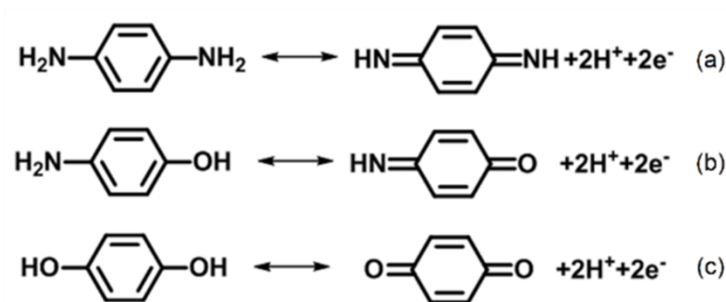
Figure 2.11 Proposed redox reactions accounting for the capacitance increase.

If the mechanism proposed above stands, there should be some differences for *bi*-substituted benzene derivatives with different configurations. For example, redox reaction occurs between OPD and *o*-benzoquinone diimine (OBD). However, there is no similar reaction for MPD. As a result, it is expected that MPD will not result in capacitance enhancement from the pseudocapacitance effect. From the CV measurements, distinct redox reaction peaks do show up at about 0.5 V for OPD/rGO (*o*-rGO). However, no such peaks appear for MPD/rGO (*m*-rGO, Figure 2.12a). The specific capacitance of *o*-rGO (200 F/g) is much larger than that of *m*-rGO (123 F/g), which agrees well with the proposed mechanism. Based on these findings, we can conclude that the main reason for the capacitance increase is the redox reactions from the benzene derivatives with *para* and *ortho* configurations of amino or hydroxyl groups.

The specific capacitance is listed in Figure 2.12b. It is obvious that the specific capacitances for samples without redox reactions (on the left) are much lower than those with (on the right). In addition, the above-mentioned hypothesis is further supported with the calculated results. The atom ratio of C/O/N for *p*-rGO is 82.8:14.3:2.9 obtained from the XPS survey spectrum, from which the PPD loading after reduction is estimated to be

30

about 11 wt%. Assuming the capacitance contribution from rGO remains unchanged in *p*-rGO, the expected specific capacitance of *p*-rGO is about 299 F/g. This value agrees well with the measurement value of 273 F/g. Moreover, the specific capacitance contributed by PPD alone is about 1551 F/g, which is 87% of its theoretical value (1784 F/g derived from the reaction shown in Figure 2.11a). The supreme utilization arises from the double-sided parallel adsorption mechanism that guarantees extremely short electron transportation for the pseudocapacitive molecules.
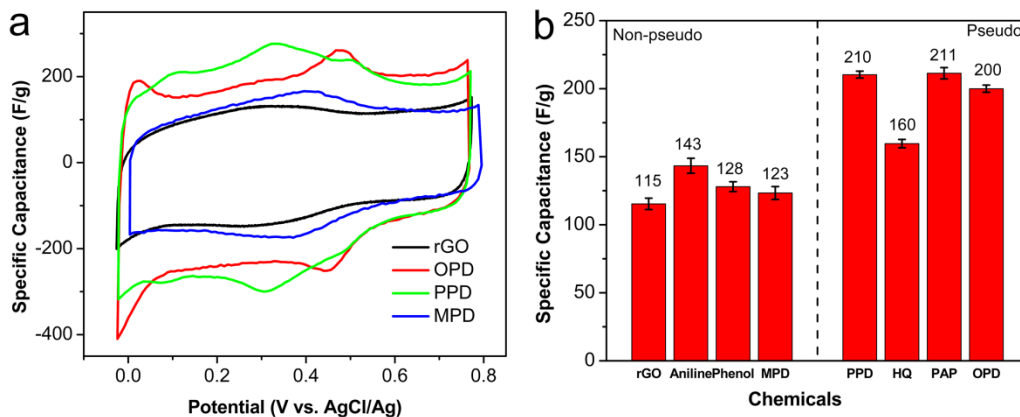
Figure 2.12 (a) CV curves of rGO, *p*-rGO, *m*-rGO and *o*-rGO at a scan rate of 10 mV/s 1 M H_2SO_4 aqueous electrolyte. (b) Specific capacitance histogram of rGO, *mono*-rGOs and *bi*-rGOs.

2.5 Conclusion

In summary, PPD is incorporated into rGO and significantly increases the specific capacitance. The as-fabricated *p*-rGO also exhibits excellent rate capability and cycling performance. After investigating a series of benzene derivatives, we attributed the main reason for the capacitance improvement to the pseudocapacitance of the aromatic

31

molecules themselves rather than the spacing effect. The pseudocapacitance arises from the redox reactions of the molecules. In accordance, the configuration of functional groups plays an important role in the capacitive enhancement; *para* and *ortho* substituted benzene derivatives have much higher capacitance values than that obtained with *meta* substituted ones. This conclusion will guide the searching of promising aromatic molecules for further enhanced supercapacitors.

CHAPTER 3   FLEXIBLE MICRO-SUPERCAPACITOR UTILIZING METAL-REDUCED GRAPHENE OXIDE

3.1 Introduction

The rapid development of portable and wearable electronics imposes many requirements on the energy storage units, including reduced form factor, good compatibility, fast charge/discharge response, excellent mechanical compliance,[125] etc. Supercapacitors are promising candidates because of their high power density and long lifetime; however, conventional supercapacitors utilize sandwiched design and require complicated packaging, making them bulky for miniaturization.

Recently, planar micro-supercapacitors (MSCs) designed for portable and wearable applications have been reported, using onion-like carbon (OLC),[125] carbide-derived carbon(CDC),[126] AC[127, 128] and graphene[46, 48, 49, 82, 129-133] as the active materials. The AC based MSCs showed large specific capacitances. However, the limited ion transport within its internal micro-porous structure resulted in a rapid capacitance decrease with increased scan rates.[127, 128] Graphene-based materials are most extensively studied for supercapacitors due to their high SSA and excellent electrical conductivity. Gao et al.[49] and El-Kady et al.[46, 48] used laser writers to reduce GO and designed various rGO/GO/rGO microstructures for MSCs. Lin et al. and Zhu et al. made graphene/CNT hybrid MSCs with CVD technique.[82, 129] Majid et al. applied the electrostatic spray deposition process to fabricate rGO/CNT based MSC.[130] For some of these devices, the direct deployment in on-chip application is difficult since high temperature environment

or liquid electrolytes are involved.[49, 82, 129, 130] In this regard, gelled electrolyte would largely alleviate this problem due to the all-solid-state characteristics. Niu et al. used gelled polyvinyl alcohol (PVA)/H_3PO_4 as the electrolyte and patterned hydrazine reduced rGO stripes as the active material.[131] Wu et al. adopted gelled PVA/H_2SO_4 electrolyte for ultrathin heteroatom-doped-graphene MSC[132] and methane-plasma-treated rGO MSC.[133] However, the loadings of the active materials were generally too small to deliver moderate capacitance for these all-solid-state MSCs, limiting their applications.

In this work, we developed a scalable method to fabricate all-solid-state flexible MSC based on rGO hydrogel (open-porous structure formed by π-π stack force between rGO sheets) *in-situ* assembled on metal template at room temperature. The as-prepared MSC shows a specific areal capacitance of 0.95 mF/cm^2 and maintains 98.3% after 11,000 times of charge/discharge cycles. In addition, extremely small relaxation time constant of 4.8 ms is achieved in gelled electrolyte, which indicates high ion transfer mobility within the structure. Besides, the device also exhibits great flexibility which retains 93.5% of the capacitance after 2,500 times of bending and twisting. These properties make as-fabricated MSC a promising energy storage candidate in wearable electronics.

3.2 Experimental

3.2.1 Preparation of Cu/Au Interdigit

The Kapton® polyimide substrate was used as-received. A 1.6 μm thick layer of positive resist (Microposit S1813, Shipley, USA) was spun cast on the Kapton substrate and exposed in a mask aligner (Karl Suss MA6 Mask Aligner, Garching, Germany) with

405 nm ultra-violet light. The exposed sample was developed in Microposit MF 315 (Shipley) developer. All the samples with patterned photoresist were cleaned by oxygen plasma in a reactive ion etching (RIE) tool (Plasma Therm Inc., USA) to remove any resist residue in exposed areas. Then Cu/Au layer was deposited in an electron beam evaporator at pressure of 3×10^{-6} Torr (CVC Product Inc., USA).

A 10-finger interdigital design with finger width of 300 μm, finger gap 200 μm and total dimension 4.8×4.8 mm^2 was employed. Ti (10 nm), Au (200 nm) and Cu (200 nm) were deposited onto the substrate successively. In the end, the photoresist was lifted off with 5 min of sonication in acetone and dried by N_2 flow.

3.2.2 Preparation of PVA/H2SO4 Gelled Electrolyte

The PVA/H_2SO_4 gelled electrolyte was prepared for the all-solid-state MSC.[134] H_2SO_4 (98 wt%, 10 g) was added into deionized water (100 mL). After that PVA (10 g) was added and the mixture was stirred at 80℃ until it became clear.

3.2.3 Preparation of All-Solid-State MSC

GO was prepared according to modified Hummers method.[135] Kapton substrate with patterned metal interdigit was immersed in GO (50 mL, 1 mg/mL) aqueous solution at room temperature for 12 h. It was then taken out from the solution and mildly washed with deionized water. PVA/H_2SO_4 electrolyte (~10 wt% for both PVA and H_2SO_4) was drop coated onto the interdigit and the sample was dried in air for certain time (12~72 h). The all-solid-state MSC was thus obtained.

3.2.4 Fabricate Conventional Sandwiched Supercapacitor

Copper foils (25 μm thickness) were cleaned with isopropyl alcohol and deionized water respectively. They were immersed in GO (1 mg/mL, 50 mL) aqueous solution for 12 h to reduce GO on the surface. After that deionized water was used to wash the adsorbed GO platelets away. The samples were immersed in dilute nitric acid to remove Cu away and washed with deionized water several times. A glass microfiber filter paper was sandwiched between two freestanding rGO hydrogel films as the separator. Two carbon fiber paper disks were attached to the backside of rGO hydrogel films as mechanical supporter and current collectors. The assembly was immersed in H_2SO_4 (1 M) for overnight. After that it was clamped between two stainless steel plates and connected to copper tapes for characterization.

3.2.5 Bending and Twisting Tests

For bending tests, samples were slowly bent around iron columns (ϕ=11 mm). For twisting, sample was bent to its diagonal around the same column.

3.2.6 Structural Characterization

Morphology of rGO hydrogel was observed with SEM (Hitachi SEM SU8010) after being freeze-dried into rGO aerogel. XPS characterization was performed with a Thermo K-Alpha XPS. Raman spectra were obtained with LabRAM ARAMIS, HORIBA JOBIN YVON with 532 nm laser used as the excitation source. FTIR was carried out at room temperature with FTIR spectrometer (Nicolet, Magna IR 560). Sheet resistance was measured with Lucas Labs S302 four point probe system. Bulk conductivity was estimated based on the thickness measured with a micrometer.

3.2.7 Electrochemical Measurement

CV, CD and EIS were measured with a Versastat 2-channel system (Princeton Applied Research). Specific areal capacitance was derived from discharging curve at different current densities. Gravimetric capacitance was obtained from CV data at different scan rates for comparison.

3.2.8 Calculations

The specific areal capacitance is derived from the constant discharge curves and calculated with $C_{areal} = \frac{i\Delta t}{A\Delta V}$, where i is the discharging current, Δt is the discharging time, ΔV is the voltage range and A is the area of the device excluding the contact pads.

Gravimetric capacitance is derived from CV curves with $C_m = \frac{2\oint idV}{m\Delta V v}$, where i is the current, V is voltage, m is the weight of the rGO hydrogel on the interdigit fingers, ΔV is the voltage range (0.8V) and v is the scan rate. Integration is carried out over a whole cycle of CV curve.

Coulombic efficiency is calculated by $\eta = \frac{\Delta t_d}{\Delta t_c} \times 100\%$, where Δt_d is the discharging duration and Δt_c is the charging time.

3.3 Results and Discussion

3.3.1 Complete Oxidation of Cu by GO

The mechanism of the simultaneous self-assembling and reduction process is schematically illustrated in Figure 3.1a. The Cu/Au interdigit serves as the current collector as well as reducing agent. Beneath that is the Ti layer used to improve the

adhesion between the metal interdigit and the polyimide substrate. The standard electrode potential $\varphi^\circ_{rGO/GO(pH=6.0)}$ was reported to be in the range of 0.4 ~ 0.6 V while $\varphi^\circ_{Cu/Cu^{2+}}$ is 0.337 V.[136] Thus Cu is able to reduce GO when it comes across the GO sheet due to its lower redox potential. Electrons will spontaneously transfer from Cu to GO by Reaction 1, leading to the reduction of GO and the dissolution of Cu.

$$anode \quad : \quad Cu \rightarrow Cu^{2+} + 2e^-$$

$$cathode : \quad GO + 2H^+ + 2e^- \rightarrow rGO + H_2O \tag{1}$$
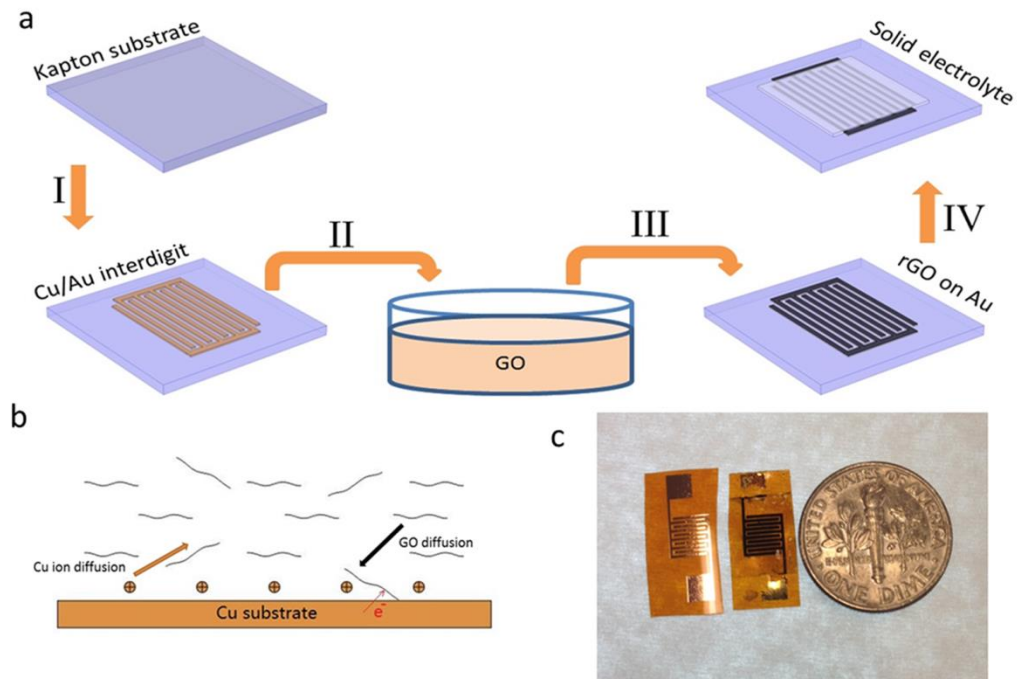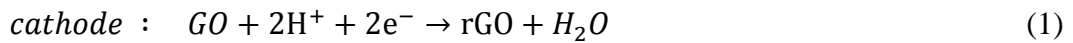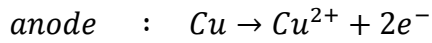
Figure 3.1 (a) MSC fabrication process: I) Fabricate Cu/Au interdigit. II) GO reduction process. III) Washing process. IV) Electrolyte infiltration. (b) Schematic illustration of the reducing mechanism. (c) Optical images of the as-fabricated devices before (left) and after reduction (middle) with a one-dime coin of U.S. as a reference.
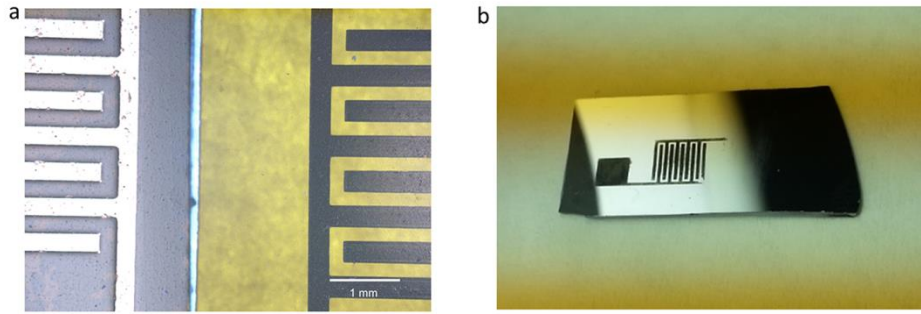
Figure 3.2 Optical microscope image of samples. (a) Left: a sample on Kapton substrate; right: a sample after rGO deposition and dry-out in air. (b) Freeze-dried rGO interdigit on SiO_2/Si substrate.

The reduced GO sheets will stay together by π-π stack force and form a hydrogel structure. The remaining Au layer will keep in contact with the obtained rGO hydrogel (Figure 3.1b) and act as the current collector. Moreover, the rGO hydrogel is electrically conductive and will act as an electron pathway from Cu to GO sheets, causing continuous GO reduction and deposition until the complete consumption of Cu is reached. After 12 h of reaction, the surface of the metal interdigit turns from shinny golden to black, which also indicates successful reduction and deposition of rGO hydrogel onto the metal surface.

Figure 3.1c presents an optical image of the original Cu/Au interdigit (left) and as-fabricated MSC (middle), which indicates the conformal coating of rGO hydrogel onto the surface of metal interdigit. The rGO hydrogel maintained the same sharp and straight design after being dried out (Figure 3.2a). No GO residue is found between the gaps of the interdigit fingers. The conformal coating phenomenon eliminates the possibility of potential short circuit during operation and allows for convenient design. Similar rGO

interdigit features are observed when Si/SiO$_2$ substrate was used instead (Figure 3.2b), which indicates that the substrate material has negligible effect on the reducing process and thus offers various choices for substrates. In our case, complete dissolution of Cu after 12 h of reaction is confirmed by energy dispersive X-ray spectroscopy (EDX). No Cu residues were found on the substrate when the rGO hydrogel was removed (Figure 3.3), which implies that Cu on the substrate was fully oxidized and removed during this process.

A control experiment is carried out to further verify the complete consumption of Cu. The Cu/Au interdigit was immersed in a GO solution for 4 h and as-fabricated MSC was tested in aqueous H$_2$SO$_4$ electrolyte. The CV curves deviate much from a rectangular shape (Figure 3.4a), which is caused by the residue Cu left on the metal interdigit during the electrochemical test:

$$anode \quad : \quad Cu \rightarrow Cu^{2+} + 2e^-$$

$$cathode \quad : \quad 2H^+ + 2e^- \rightarrow H_2 \uparrow \tag{2}$$

As can be seen in Reaction 2, H$^+$ is released from the cathode in the form of H$_2$. This is confirmed with the bubbling of gas out of alternative interdigit fingers during the CV test. Figure 3.4b shows the interdigit after being dried out. The rGO hydrogel on the even-numbered fingers (cathode) is peeled off by the generated gas while that on the odd-numbered fingers (anode) remains. The bubbling does not show up for samples immersed for 12 h and thus confirms the complete consumption of Cu during the process.
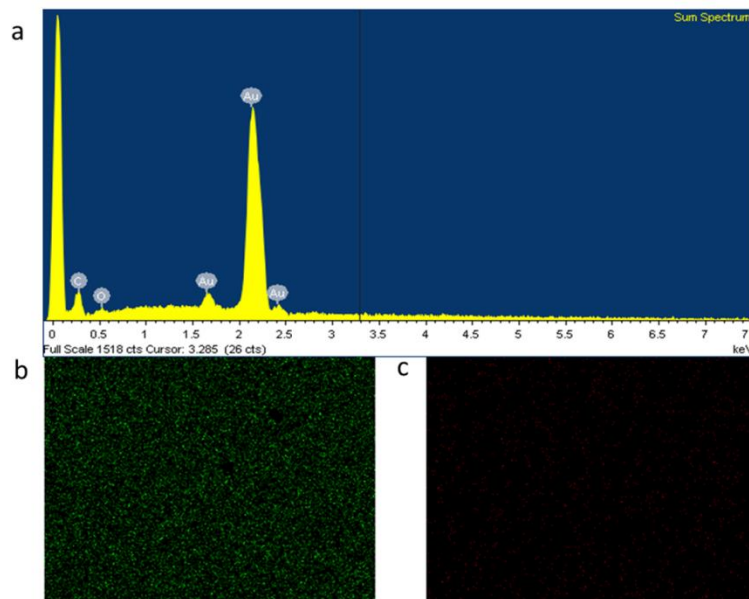
Figure 3.3 EDX analysis. The tested area was one of the contacting pads on Kapton substrate. It was carried out after the device was put in 50 mL GO solution (1 mg/mL) for 12 h and the rGO was gently wiped away with a wet napkin. (a) Sum spectrum. No obvious peaks corresponding to Cu were detected. (b-c) Element mappings of Au (b) and Cu (c). The intensity for Cu is much smaller compared with that of Au.
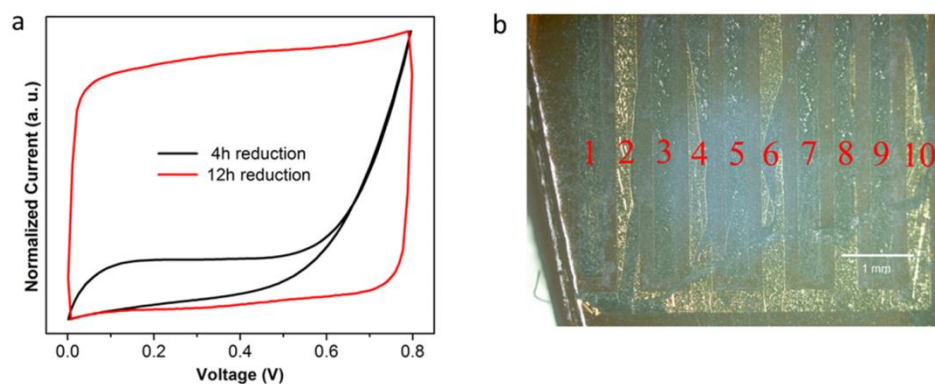
Figure 3.4 (a) CV curves of samples (normalized for easier comparison) reduced for 4 and 12 h in GO solution, and tested in aqueous H_2SO_4 electrolyte, respectively. (b) The 4 h sample dried out in air after CV test.

3.3.2 Benefits of this Method

This method is suitable for the facile fabrication of MSC due to many advantages, including 1) the rGO hydrogel coating is conformal to the metal patterns, allowing for the precise control of rGO hydrogel electrodes and fine-pitch designs; 2) The reduction reaction and the assembly procedure are simultaneous, low-temperature processed and environmentally benign, eliminating the need for post-treatment that usually involves either toxic chemicals or high temperature;[137] 3) The procedure is applicable to different substrates such as ceramic, polymer film and silicon wafer as long as they are compatible with photolithography.

3.3.3 Morphology and Chemical Properties of the as-produced rGO Hydrogel

The rGO hydrogel is freeze-dried into aerogel and characterized with SEM. The top-view SEM image (Figure 3.5a) reveals an open porous structure similar to those obtained with hydrothermal method[44] and Zn reduction approach.[138] No obvious lateral growth is observed and the sharp edges of as-prepared rGO interdigit allow the possibility for further pitch reduction (Figure 3.2a). The cross-section SEM image in Figure 3.5b reveals an interconnected porous structure with rGO sheets lying preferentially parallel to the substrate. This open-porous quasi-parallel structure will decrease the resistance for lateral ion transport, improving the rate performance.[139]
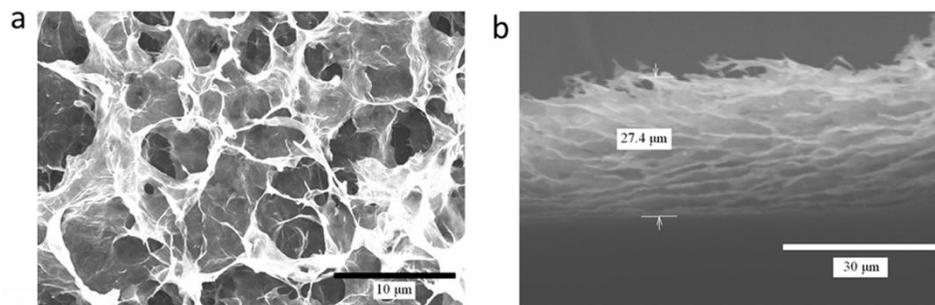
Figure 3.5 (a) Top and (b) cross-section SEM images of freeze-dried rGO aerogel on a Kapton substrate.

The reduction of GO is confirmed by XPS, Raman spectrum, and FTIR. Carbon-to-oxygen atom ratio increases from 2.1 of GO to 6.8 of rGO aerogel by the quantitative XPS survey, indicating that significant amount of oxygen is removed during the process.[140] In addition, the high resolution C1s XPS spectrum of rGO aerogel in Figure 3.6a can be deconvoluted into three characteristic peaks at 284.4 eV (C-C/C=C graphitic structure), 286.2 eV (hydroxyl and epoxy C-O groups) and 288.9 eV (carbonyl group). The peak intensity corresponding to C-O group is greatly reduced for rGO compared to that of GO. In the Raman spectra (Figure 3.6b), the D to G peak intensity ratio (I_D/I_G) increases from 0.9 to 1.2, probably caused by the formation of smaller sp2 domains after reduction.[141] These small domains will increase sp3 edge defects, which might provide extra surface area and thus enhance the specific capacitance. In the FTIR spectra (Figure 3.6c), the carboxyl peak at 1725 cm^{-1} disappears after the reaction, further validating the reduction of GO.[142, 143] In addition, the rGO reduced by Cu shows good electrical conductivity. The as-prepared rGO hydrogel has sheet resistance of 192 $\Omega/\square$ and bulk electrical conductivity of 0.38 S/cm, which are comparable to that prepared by

43

vacuum filtration method (0.58 S/cm).[144] The electrical conductive rGO hydrogel provides a fast electrical transport pathway and eliminates the need of conductive additives generally used in supercapacitor electrodes.[62]
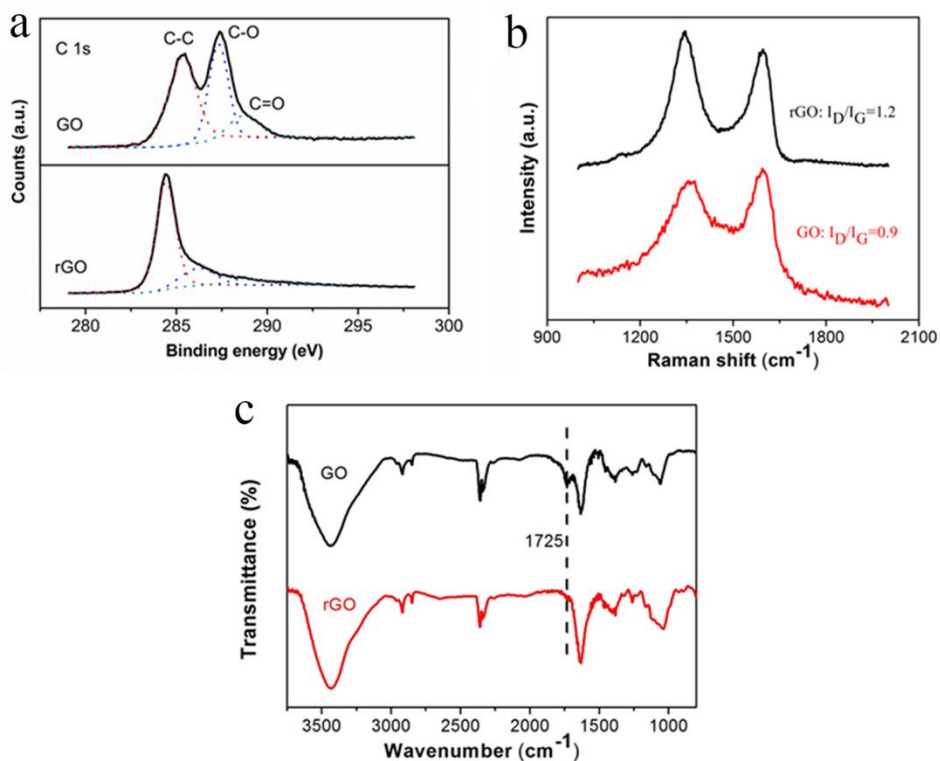
Figure 3.6 (a) XPS spectra, (b) Raman spectra, and (c) FTIR spectra of GO film and rGO aerogel.

3.3.4 Electrochemical Performance of the Solid-State MSC

The all-solid-state MSC was fabricated utilizing PVA/H_2SO_4 gel as the solid-state electrolyte. Gelled electrolyte exhibits excellent mechanical flexibility which is suitable for wearable electronics. It also eliminates the necessity of complicated sealing

components generally required in conventional supercapacitors, greatly easing the manufacturing process. During fabrication, the low-viscosity PVA/H_2SO_4 liquid electrolyte first infiltrates into the rGO hydrogel. With the evaporation of H_2O, the viscosity of the electrolyte increases so much that it turns into a gel. The as-fabricated MSC shows rectangular CV curves even at a scan rate of 6 V/s (Figure 3.7a), which indicates that the capacitance arises from EDLC and the ion transportation within the electrode is extremely fast. It is suggested that volumetric and areal capacitance are of equivalent significance as the gravimetric capacitance in real applications.[145] Here the areal performance of the as-fabricated MSC is evaluated considering the total area of device (the rGO hydrogel interdigit, the Au interdigit current collectors and the gaps between them). Figure 3.7b shows the CD curves at different current densities. The perfect linear charge/discharge curves further confirm that the capacitance arises from EDLC. Also, the symmetric CD curves imply high Coulombic efficiency,[146] which reaches 99% for as-prepared MSC and guarantees excellent charge/discharge reversibility.

Figure 3.7c shows the areal capacitance at different current densities. The MSC exhibits an areal capacitance of 0.95 mF/cm^2 at a discharging current of 0.43 mA/cm^2, which slightly decreases to 0.82 mF/cm^2 at 4.3 mA/cm^2. The areal capacitance achieved is comparable to those EDLC based MSC reported in literatures (0.4~2 mF/cm^2).[128, 147, 148] Cycling test was carried out at a charge/discharge current of 1.3 mA/cm^2 and the result is shown in Figure 3.7d. The areal capacitance retained about 98.3% of the initial value after 11,000 cycles, suggesting an excellent cycling performance.
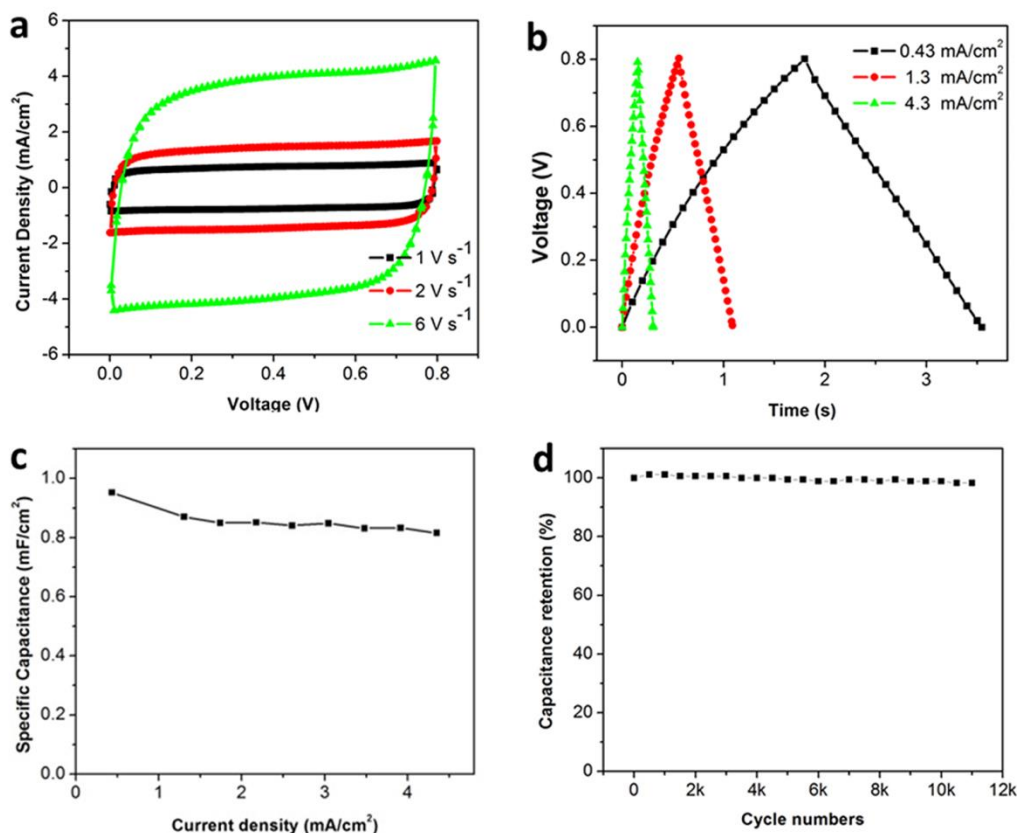
Figure 3.7 Electrochemical characterization of as-fabricated MSC in PVA/H_2SO_4 gelled electrolyte dried in air for 72 h. (a) CV curves at scan rates of 1, 2, and 6 V/s, respectively. (b) CD curves at current densities of 0.43, 1.3, and 4.3 mA/cm^2, respectively. (c) Specific areal capacitance calculated from discharge curves at different current densities. (d) Capacitance retention during 11,000 times of charging and discharging at current density of 1.3 mA/cm^2.

EIS was further used to study the performance of as-prepared MSC. The Nyquist curve (Figure 3.8a) is almost perpendicular to the X-axis at low frequency region, which indicates that the MSC acts like an ideal capacitor.[62, 149, 150] In addition, the semicircle typically observed at high frequency region for conventional carbon-based supercapacitors does not show up in our MSC. This semicircle is associated with nano pores within the electrode material which will impose large ionic diffusion resistance to the system.[150] The absence of this semicircle indicates fast ion transportation, which

might be caused by the open-porous structure of rGO hydrogel that makes the entire surface accessible for fast ion adsorption/desorption.
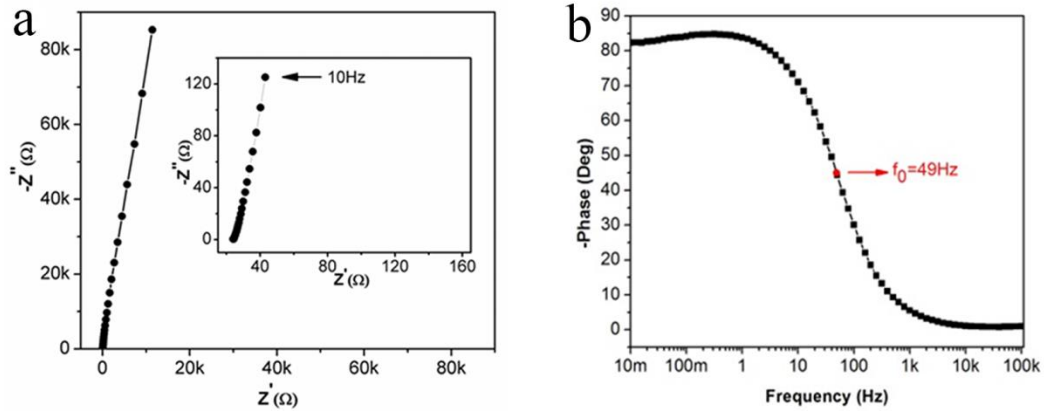
Figure 3.8 (a) EIS spectrum measured from 10 mHz to 100 kHz. Inset shows magnified view of high frequency region. (b) Bode phase diagram versus frequency. f_0=49 Hz corresponds to phase angle of -45 °.

Figure 3.8b shows the plot of impedance phase angle versus frequency, also known as Bode phase plot. The phase angle stays above -80° at frequency below 3.2 Hz, indicating nearly pure capacitive behavior. The frequency at -45° is 49 Hz for the sample fully dried in air for 72 h, corresponding to a relaxation time constant (τ_0) of 20 ms. The τ_0 can be further controlled by adjusting the evaporating time which will affect the water concentration and ion mobility within the gelled electrolyte. For example, it decreases to 4.8 ms (208 Hz) when gelled in air for 12 h and 1.9 ms (529 Hz) when 1 M H_2SO_4 aqueous electrolyte was used (Figure 3.9a). These values are comparable to those of the state-of-art MSCs fabricated with onion-like nano-diamond (26 ms),[125] laser-scribed graphene (LSG, 19 ms),[46] and CVD grown CNT carpets (0.82~2.62 ms).[82]

The excellent rate performance probably arises from the quasi-parallel structure of the rGO hydrogel and the in-plane design of the electrodes, which greatly reduce the in-plane ion transport barrier. For comparison, the performance of our work and those of state-of-the-art MSCs are listed in Table 3.1. Our sample exhibits a specific areal capacitance comparable to those reported in literature.[82, 125, 130] What's more, the relaxation time constant of our all-solid-state MSC is even competitive compared with those of liquid electrolyte based MSCs.
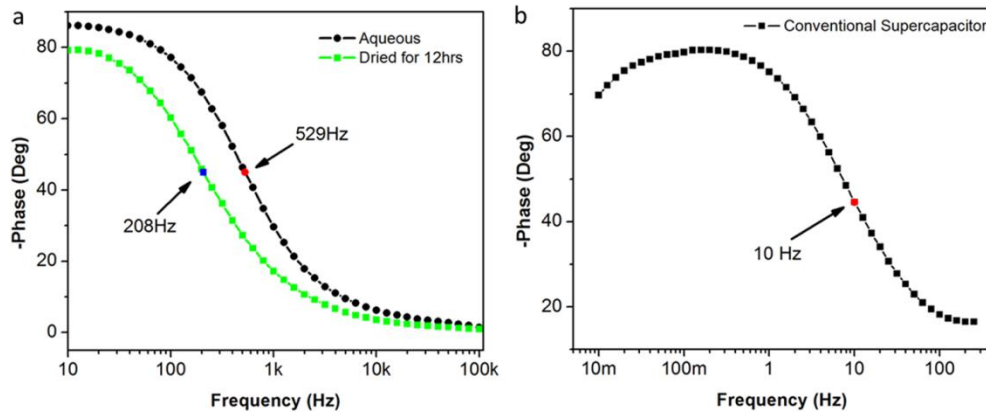
Figure 3.9 (a) Plot of impedance phase angle against frequency for MSC with aqueous and gelled electrolyte, respectively. (b) Plot of impedance phase angle against frequency for TSC in 1 M H_2SO_4 aqueous electrolyte. The frequency at -45^0 was 10 Hz.

3.3.5 Comparison with Traditional Supercapacitors (TSCs)

TSCs were also fabricated using rGO hydrogel reduced on Cu foil for comparison. Figure 3.9b shows the Bode phase plot of as-fabricated supercapacitor in 1 M H_2SO_4 aqueous electrolyte. The frequency corresponding to -45 ° (10 Hz) is much smaller than that of MSC with 1 M H2SO4 aqueous electrolyte (529 Hz, Figure 3.9a). In addition, a

semicircle at high frequency region is clearly shown in the impedance spectrum (Figure 3.10b), indicating large ionic diffusion resistance at high frequency in the device. Besides, the knee frequency of TSC (100 Hz), above which the supercapacitor will act more resistive, is an order of magnitude smaller than that obtained for MSC with an aqueous electrolyte (~2.0 kHz Figure 3.10a). As a result, the CV curves at high scan rates (Figure 3.11a) are much more deformed. For convenience, gravimetric capacitance is compared between TSC and MSC (Figure 3.11b). It can be seen that MSC shows a higher specific capacitance of 147 F/g compared to 110 F/g of TSC at a scan rate of 50 mV/s and retains 66.0% of that value at 6 V/s compared to 48.9% for TSC.

Table 3.1 Comparison of the as-prepared MSC with State-of-the-Art MSCs.

materials	electrolyte	capacitance (mF/cm2)	τ_0 (ms)	substrate	Ref.
rGO	solid	0.87	4.8~20	All	this work
rGO	solid	0.14[a]	N/A	Si/SiO$_2$	[151]
rGO	solid	0.16[a]	N/A	All	[131]
laser reduced GO	solid	1.6[a]	19	All	[46]
Graphene/CNT	liquid	0.97[a]	2.6	Si/SiO$_2$	[82]
rGO/CNT	liquid	4.5	4.8	Si/SiO$_2$	[130]
OLC	liquid	1.1[a]	26	All	[125]

[a]These values were adjusted to specific areal capacitance at a scan rate of 1 V/s based on information from the papers.
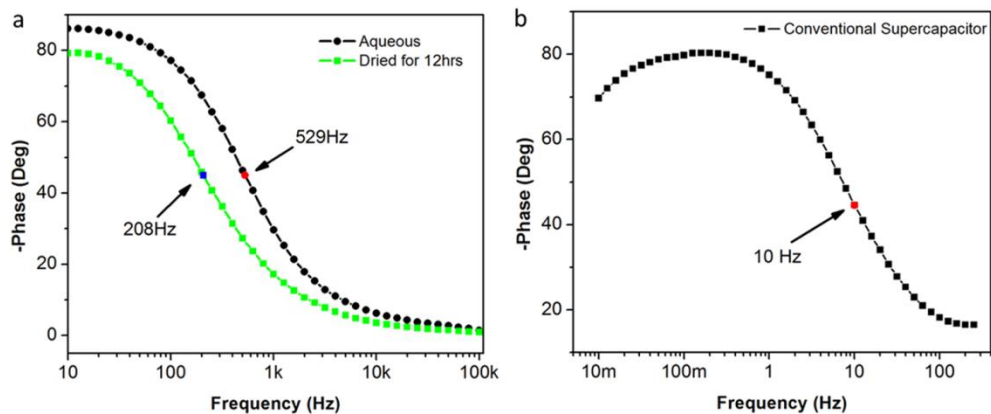
Figure 3.9 (a) Plot of impedance phase angle against frequency for MSC with 1 M H_2SO_4 electrolyte and gelled PVA/H_2SO_4 electrolyte, respectively. (b) Plot of impedance phase angle against frequency for TSC in 1 M H_2SO_4 aqueous electrolyte. The frequency at -45^0 was 10 Hz.
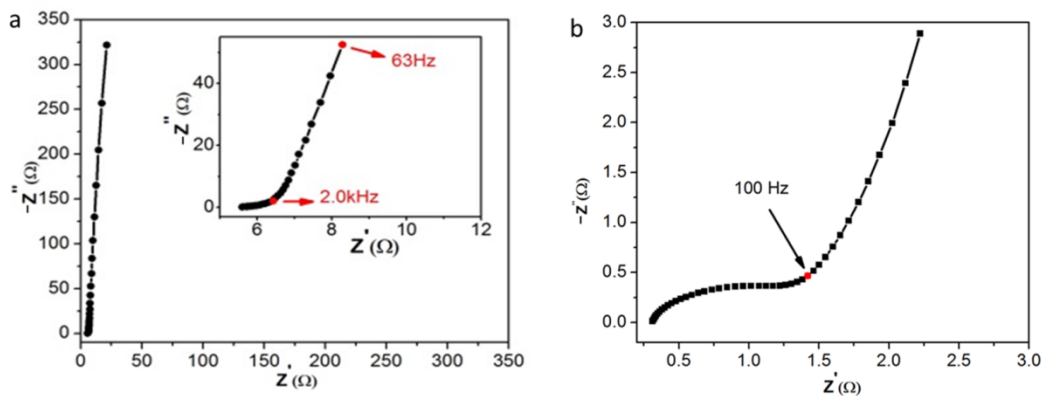
Figure 3.10 (a) EIS spectrum of MSC in 1 M H_2SO_4 electrolyte. Inset shows the magnified view of the high-frequency region. (b) EIS spectrum of TSC in 1 M H_2SO_4 electrolyte.
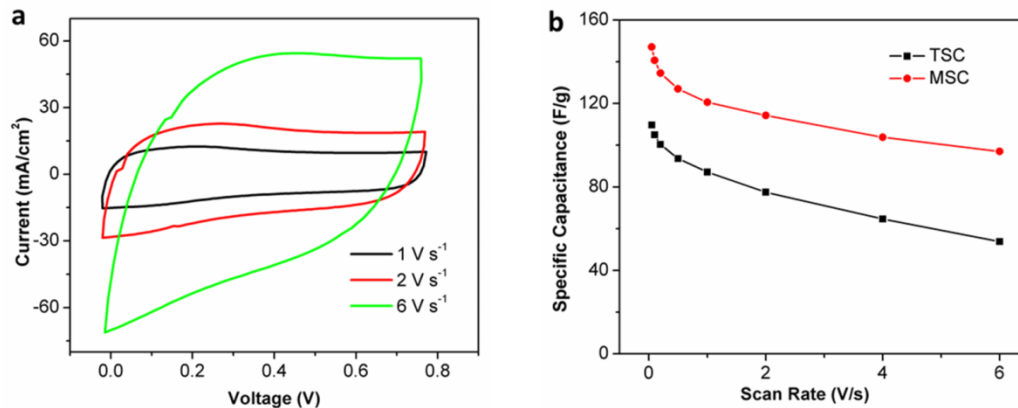
Figure 3.11 (a) CV curves of TSC at scan rates of 1, 2, 6 V/s, respectively. (b) Comparison of the gravimetric capacitance between TSC and MSC.

3.3.6 Flexibility Test

Our MSC shows great mechanical compliance. Figure 3.12a shows an image of the all-solid-state MSC bent around a fingertip. Electrochemical characterizations of the MSCs bent at different curvatures were carried out to test the flexibility. CV curves for samples bent around columns with different diameters exhibit nearly identical profiles to those of the unbent sample (Figure 3.12b). The sample was further bent around an 11 mm diameter column for 2,500 times and then twisted around the same column for another 2,500 times (the diagonal of the sample parallel to the column axis). Charge/discharge tests were carried out every 100 bending/twisting operations to test the mechanical reliability (Figure 3.12c). It retained 95.9% of the initial capacitance after 2,500 times of bending and 93.5% after another 2,500 times of twisting. The excellent flexibility and stability make the as-fabricated MSC suitable for flexible and wearable applications.

51
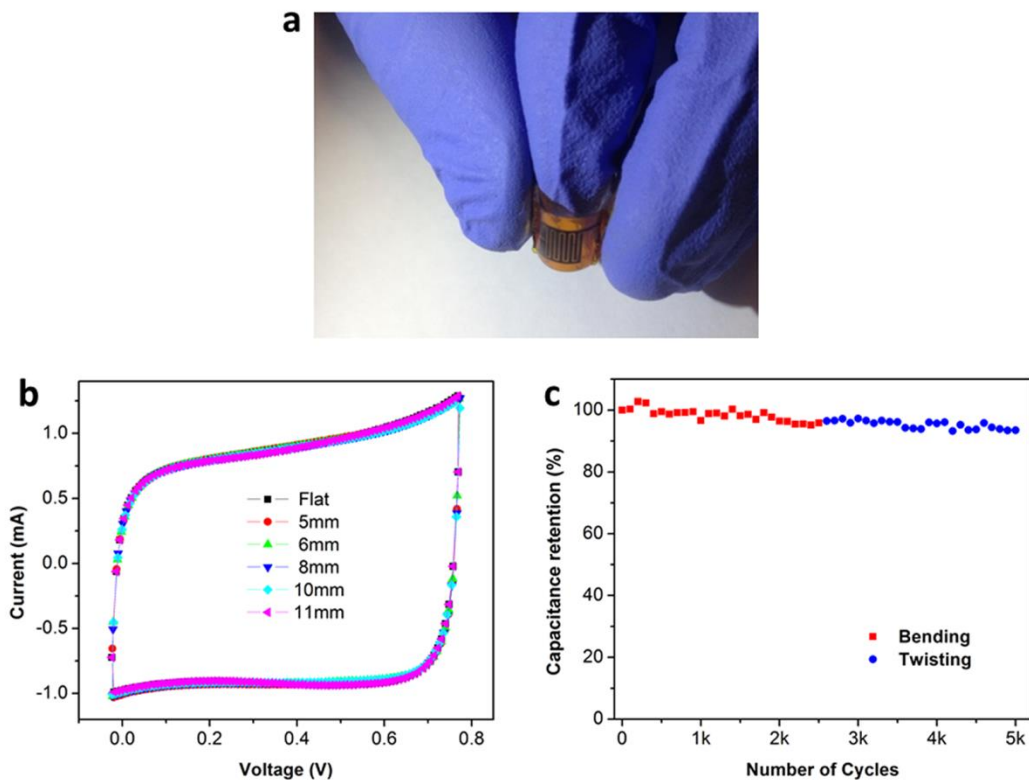
Figure 3.12 Performance of MSC at deformed condition. (a) A photo of the device at bent state. (b) CV curves of a device bent around columns with different diameters as well as that of unbent state as a reference (scan rate 1 V/s). (c) Capacitance retention during bending and twisting test for 5,000 times.

3.4 Conclusion

In summary, an all-solid-state flexible MSC is fabricated by in situ reduction and assembly of GO on a Cu interdigit template. The interdigital design and quasi-parallel alignment of rGO hydrogel provide a rapid charge and electron transport pathway. Excellent rate performance and extremely small relaxation time constant are achieved even in solid state. In addition, the superior mechanical compliance and stability of MSC make it suitable for wearable electronic applications. The fabrication process is room

temperature operated, environmentally-friendly, and easily scalable by using Cu interdigit

prepared by industrialized methods such as inkjet printing. This approach might play an

important role as on-chip energy storage in the future.

CHAPTER 4   GRAPHENE-BASED AC LINE-FILTERS

4.1 Introduction

Ac line-filters are used to smooth the leftover ac ripples on direct current (dc) voltage buses for most line-powered devices. To effectively filter out the ac ripples on dc input, a large capacitor is required in ac line-filtering devices. Currently, AECs are widely used for this purpose due to their relatively lower fabrication cost and higher specific capacitance compared to conventional thin-film capacitors. However, they are still the biggest component in many electronic systems. Their bulky size is becoming more and more incompatible with the rapid development of miniaturized portable and wearable electronics.

It is of great interest to develop a capacitor with competitive performance yet much smaller volume. Electrochemical capacitors, also known as supercapacitors, may help to alleviate the volumetric problem due to their extremely large capacitance density. Their specific capacitances are generally several orders of magnitude higher than other types of capacitors.[152] As a result, it requires much less space to obtain the designed capacitance. Different materials are studied extensively, including carbon derivatives,[62, 150, 153] conducting polymers,[154, 155] metal oxides[156, 157] and their hybrids.[158, 159] Unfortunately, their frequency response is still unsatisfactory and requires further improvement. Particularly, the phase angle of a typical supercapacitor approaches zero degree at 120 Hz for most supercapacitors, far below -90 ° that is ideal for ac line-filtering.

In principal, supercapacitors based on EDLC are similar to AECs in that they both

adopt physical storage mechanism. They are potentially capable of replacing the traditional AECs if their frequency response can be greatly improved. In this sense graphene and CNTs are the best candidates due to their extremely high SSA and excellent electrical conductivity. Recently devices based on these carbon allotropes have been designed and fabricated with rate performance comparable to those of AECs.[46, 49, 79-83] For example, Miller et al. used a radio frequency plasma-enhanced chemical vapor deposition method (PECVD) to fabricate VG sheets as the active material and reported a phase angle of -82° at 120 Hz.[81] Lin et al. designed interdigital MSCs with graphene/VACNT arrays, which was grown by a conventional CVD approach, and achieved a phase angle of -81.5°.[82] Sheng et al. electrochemically reduced GO on a gold foil and reported a phase angle of -84°.[83] However, most of these methods are unsuitable for large scale production. In addition, the high processing temperature is incompatible with the flexible substrate that is critical for wearable electronics.
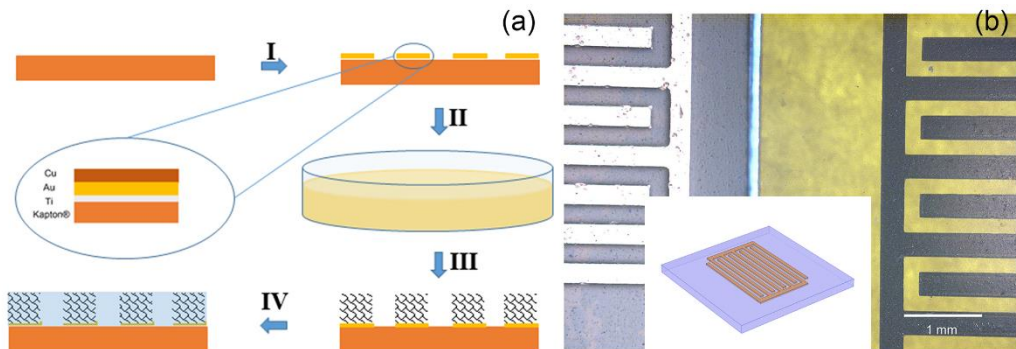
Figure 4.1 (a) Illustration of the fabrication process. I, photolithography process; II, GO reduction; III, washing and cleaning; IV, electrolyte infiltration. The inset represents the cross-section sketch of the metal interdigit (not to scale). (b) Optical images of the device before (left) and after (right) rGO assembling and air-drying. Inset: the illustration of the substrate patterned with metal interdigit.

Here we design a novel wet chemical method to fabricate a graphene-based ac line-filter. The as-fabricated device shows a phase angle of -75.4 °at 120 Hz. The device also shows a specific capacitance of 316 $\mu F/cm^2$ and a RC time constant of 0.35 ms. In addition, it retains 97.2% of the initial capacity after 10,000 galvanostatic charge/discharge (CD) cycles. The excellent stability is beneficial for practical deployment.

4.2 Experimental

4.2.1 Fabrication of the Graphene-Based ac Line-Filters

The procedure is illustrated in Figure 4.1a. First, a metal interdigit is fabricated on top of a polyimide substrate (125 μm thick, Kapton®, Dupont, USA). This step is identical to that described in Section 3.2.1. The as-prepared metal interdigit consists of three layers of metals: on top is a Cu layer (200 nm thick) acting as the reducing agent during the GO reduction and assembly process; beneath the Cu layer is an Au layer (200 nm thick) that serves as the current collector; at the bottom is a Ti layer (10 nm thick) used to improve the adhesion between the metal interdigit and the polyimide substrate. Then the substrate with patterned metal interdigit is soaked into the GO solution for 12 h, during which the GO sheets are simultaneously reduced and assembled onto the metal interdigit. After that the sample is mildly washed with deionized water and soaked in 1 M sulfuric acid for 3 h before electrochemical tests. The aqueous sulfuric acid serves as the electrolyte for our device.

4.2.2 Electrochemical Measurement

CV, CD and EIS are measured with a Versastat 2-channel system (Princeton Applied Research). Specific areal capacitance is derived from discharging curve at different current densities. Gravimetric capacitance is obtained from CV data at different scan rates for comparison.

<div align="center">

4.3 Results

</div>

4.3.1 Physical Properties of Our ac Line-Filters

The metal-reduction mechanism of GO is extensively explained in Section 3.3. Figure 4.1b presents the structure of our device (inset) and the optical images of the as-fabricated metal interdigit with and without rGO assembling. The shiny golden interdigit turns into black stripes with the rGO on top. In addition, the interdigit fingers remain sharp and straight without any GO residues in between, which avoids the risk of short-circuit failures during operation. The inset is the sketch of the metal interdigit pattern. Here Cu is chosen as the reducing agent mainly for two reasons: (1) Cu produces the best rGO in terms of the carbon-to-oxygen ratio compared to other metals like Zn and Fe, even though Cu is usually considered less reactive;[136] (2) the photo-lithography technique for patterning of Cu is very mature.

Our innovative approach provides many advantages. Firstly, it is prepared at room temperature, which offers great flexibility on substrate selections. For example, flexible polymer substrates such as polyimide or polyethylene terephthalate (PET), which cannot stand high temperature operation, can be employed. It thus enables the ability to be integrated into wearable electronics. Secondly, it utilizes an interdigital structure that

avoids the need of a bulky separator membrane and greatly eases the fabrication process. Moreover, our approach is readily scalable. All the steps involved, such as the photolithography step and the solution processing, are well established and mature. As a result, it reduces the fabrication cost significantly compared to those CVD methods.
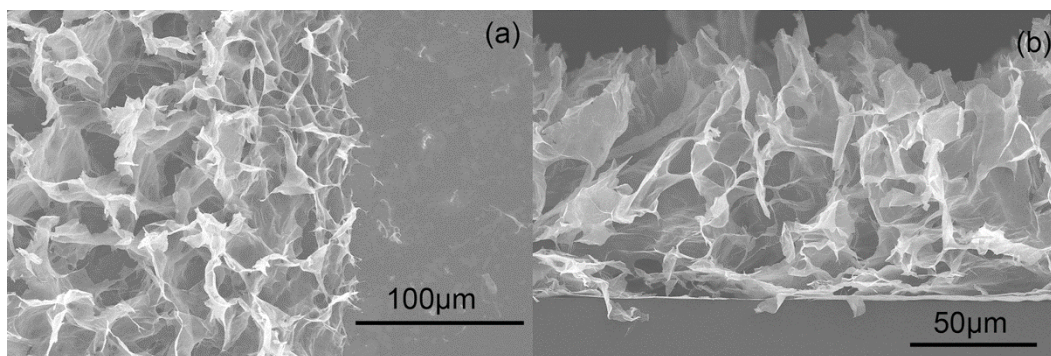
Figure 4.2 (a) Top-view and (b) side-view of a free-dried rGO aerogel on a metal interdigit finger.

4.3.2 Morphology of the rGO Electrodes

Figure 4.2 presents the top and cross-section SEM images of the freeze-dried rGO aerogel assembled on the metal interdigit of a silicon substrate. The as-reduced rGO sheets form a 3D interconnected structure that attaches onto the metal interdigit instead of diffusing away. The sharp edges clearly maintain the original metal interdigital design and illustrate the conformal coating mechanism.

Electrochemical tests were carried out to test the performance. Figure 4.3a shows the CV curves at scan rates of 2, 5 and 8 V/s, which are approximately two orders of magnitude higher than those for conventional supercapacitors. The rectangular CV curves

at high scan rates imply small series resistance and efficient EDLC attribute of the as-prepared rGO hydrogel electrode.[160] Figure 4.3b shows the cycling performance of the device. The capacitance retention is 97.2% after 10,000 times of CD cycles at a current density of 0.58 mA/cm^2. The good cycling performance of our device is highly desirable in real applications.
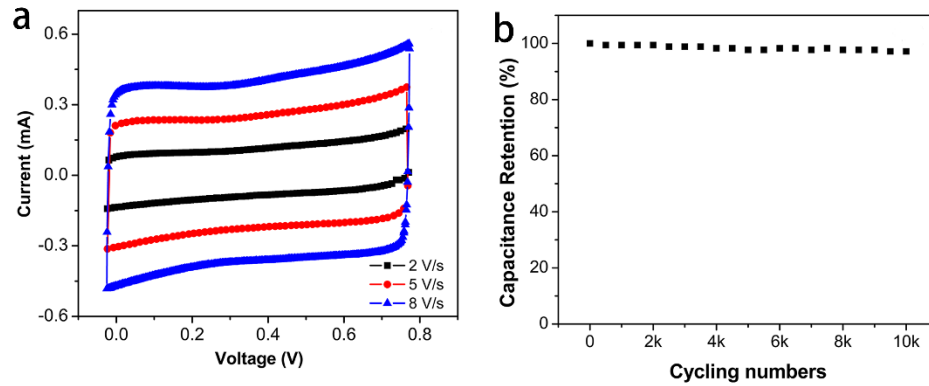
Figure 4.3 (a) CV curves of the device at scan rates of 2, 5 and 8 V/s, respectively. (b) Stability performance measured with CD cycling at a current density of 1.3 mA/cm^2.
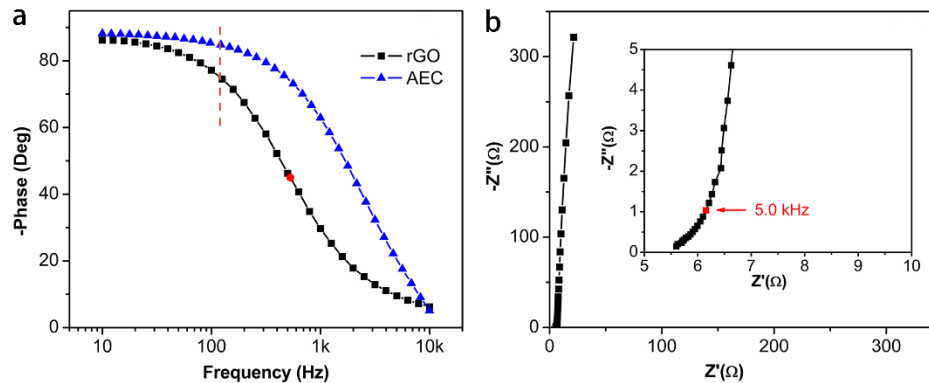
Figure 4.4 (a) Bode phase diagram of our device and AEC. (b) AC impedance spectrum of our device. The inset shows the magnified high-frequency region.

4.4 Discussion

The fast ion transport as well as the excellent stability is highly desirable for ac line-filtering. To justify the feasibility of our device, EIS is carried out from 10 Hz to 100 kHz with a 10 mV sinusoidal voltage input. The impedance phase angle for ideal capacitors is -90 ° regardless of the frequency. In real-life applications, the phase angle approaches -90 ° at low frequencies and then decreases as frequency further increases. The value at 120 Hz is usually used as a figure-of-merit to estimate the filtering efficacy. Figure 4.4a presents the impedance phase angle diagram for our as-fabricated ac line-filter. The phase angle maintains above -80 ° at frequency below 79 Hz and reaches -75.4 ° at 120 Hz. The frequency at -45 °, usually used for comparison, reaches 529 Hz in our case. These parameters are better than those high-power supercapacitors fabricated with LSG,[46] OLC[128] and CNT.[161, 162]

The superior performance is caused by the high-quality electrical conductive rGO electrodes that avoid distributed charge storage. Our rGO electrode achieves a high carbon-to-oxygen ratio of 6.8 for from the quantitative XPS survey, much higher than those reported with metal[136, 138] and thermal reduction methods.[140, 163] Figure 4.4b exhibits a nearly vertical impedance spectrum at low frequency region for the as-fabricated ac line-filter, which indicates almost pure capacitive behavior.[150] Typically a semi-circle is found in AC[150, 164] and rGO[62, 120] based supercapacitors at the high frequency region of the Nyquist plot; this semi-circle is caused by the capacitive coupling between the electrode and the current collector. In contrast, no semi-circle appears at the high frequency region for our device (Figure 4.4b, inset), suggesting excellent electrical connection at the interface between the rGO electrode and the gold current collector.
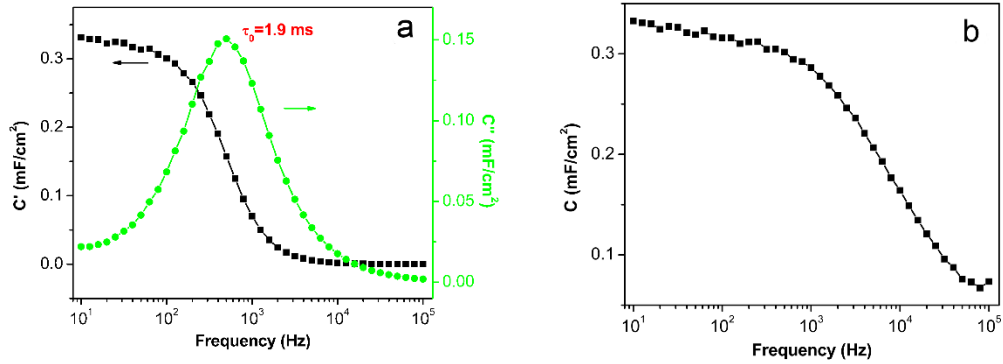
Figure 4.5 (a) The variation of real and imaginary part of capacitance versus frequency. (b) Areal capacitance versus frequency.

The outstanding performance is further supported with the ultra-small τ_0. τ_0 reflects the minimum time needed to discharge all the energy from the device with an efficiency of greater than 50%. It can be obtained from the frequency value at the maximum imaginary capacitance (C").[82, 83, 165] Figure 4.5a shows an extremely small τ_0 of 1.9 ms for the as-fabricated ac line-filter. Meanwhile, a series RC circuit model, also known as Randles circuit model, is employed to simulate the capacitive and resistive components of the device. The specific areal capacitance is calculated based on the equation of $C_A = -1/2\pi f A Z''$, in which f is the frequency, A is the area of the device and Z'' is the imaginary part of the impedance.[165] Figure 4.5b presents the frequency response of specific areal capacitance, which reaches 316 $\mu F/cm^2$ at 120 Hz and maintains capacitive behavior up to 10^4 Hz. The resistance at 120 Hz is 7.5 Ω, which corresponds to a RC time constant τ_{RC} of 0.35 ms considering an electrode area of 14.88 mm^2 of the device. This value is comparable to those reported with vertical graphene EDLC (0.20 ms),[81] graphene/VACNT hybrids (0.20~0.40 ms)[82] and electrochemically reduced GO (1.35 ms).[83] It is also significantly smaller than the required 8.3 ms for 120 Hz filtering.

61

A detailed comparison of performance with other ac line-filters is listed in Table 4.1. Our device exhibits very promising phase angle at 120 Hz, which is comparable to most of those reported in literature and slightly lower than that of electrochemically reduced GO and commercial AEC. It also possesses excellent time relaxation constants and RC time constant, much shorter than the required 8.3 ms for ac line-filtering. In addition, its specific areal capacitance is one of the best among those reported with phase angle better than -70 °at 120 Hz, which is beneficial for miniaturization. These attributes make it very promising in real-life applications.

Table 4.1 Comparison of performance of ac line-filters using different electrode materials.

Material	Substrate	-Phase at 120 Hz (°)	τ_{RC} (ms)	τ_0 (ms)	Capacitance (mF/cm^2)
this work	F[a]	75.4	0.35	1.9	0.32
AEC	N[a]	84.8	0.11	0.46	N/A
VG[81]	N	82	~0.2	N/A	0.0875
Graphene/ VACNT[82]	N	73.4~81.5	0.2~0.4	0.82~2.62	0.23~0.66
rGO[83]	F	79.5~85	1.35	0.17~1.0	0.283
LSG[46]	F	<30	N/A	19	N/A
OLC[128]	F	N/A	N/A	26	N/A

[a]F and N designate that the substrate can and cannot be flexible, respectively.

4.5 Conclusion

In conclusion, we have designed a scalable method to manufacture ac line-filter based on patterned rGO. The procedure is solution based and carried out at room temperature, which makes it compatible with flexible substrates. The rate performance,

areal capacitance and RC time constant of our device are competitive among all the reported ac line-filtering devices. The high areal capacitance of the device benefits significantly to the miniaturization of whole electronic system. The excellent rate performance, scalable room temperature manufacturing process and compatibility with flexible substrates make it suitable for ac line-filtering in the field of wearable electronics.

CHAPTER 5   3D GRAPHENE FOR THERMAL INTERFACE MATERIALS

5.1 Introduction

5.1.1 Thermal Interface Materials

The market of electronic devices is growing rapidly these decades. According to Moore's law, the number of transistors in a processor doubles approximately every two years, which will become 15 billion in 2015.[84] This large amount of transistors in a dense integrated circuit will generate a lot of waste heat and increase the temperature of the chip. High temperature environment or rapid temperature change, especially in the case of turn on and off, exerts great thermal stress on the packaging of the devices. In addition, elevated temperature will also increase the current leakage, which in turn further increases the temperature. These factors with the accompanied thermal stress will lead to thermal run-aways in the devices and reduce their lifespan over time.

A lot of heat sinks, for example the fans in laptops, are designed to help dissipate the heat away. The heat generated in the circuits needs to be conducted to the heat sink. Unfortunately, the surfaces of solid materials are rough and rigid. When two solid pads pressed together, only a small proportion of the surface area will contact the other pad (Figure 5.1a). The rest of the surface will be exposed to air, which is a poor heat conductor (κ=0.024 W/mK). As a result, the heat cannot be conveniently conducted from the chip to the external heat sink due to the surface mismatch.

TIMs play a critical role to alleviate this issue. As shown in Figure 5.1a, an ideal TIM is deployed to fully fill the gap between the two solids. In practice, the TIM is not

ideal, which generally leaves small air traps in between (Figure 5.1b). As a result, the total thermal resistance (R_t) will be composed of three parts: the contact resistance between the TIM and the surface as well as the thermal resistance of the TIM bond line thickness (BLT) itself (Equation 5.1). It is obvious that we should minimize the two contact resistance (R_{c1} and R_{c2}), increase the thermal conductivity of the TIM (κ_{TIM}) and decrease the BLT to improve its performance.

$$R_t = R_{c1} + \frac{BLT}{\kappa_{TIM}} + R_{c2} \qquad\qquad 5.1$$

Various TIMs have been investigated and commercialized. Generally they can be classified into the following categories according to their configurations: thermal greases,[86-89] phase change materials,[90-95] solders[96-100] and thermally conductive composites.[101-105] Most of these materials are made of a polymeric matrix filled with thermally conducive fillers. Thermal greases are mixtures of polymers and thermal-conductive ceramic or metallic fillers. They are convenient and cost-effective materials which also exhibit high thermal conductivity and low thermal stress due to their high compliance. However, dry-out and pump-out issues occurred during operation greatly impair their reliability. Phase change materials offer better stability yet higher viscosity and lower thermal conductivities compared with thermal greases. Low melting temperature solders are much more conductive, yet they suffer from their vulnerability to cracks and corrosions as well as the thermal stress induced by thermal mismatch. Thermally conductive composites are much more convenient to handle and conform to the surface irregularities smoothly due to their low viscosity. They are also resistive to harsh environments and pump-out problems. The drawback is their relative higher cost, lower thermal conductivity and delamination problem over time.
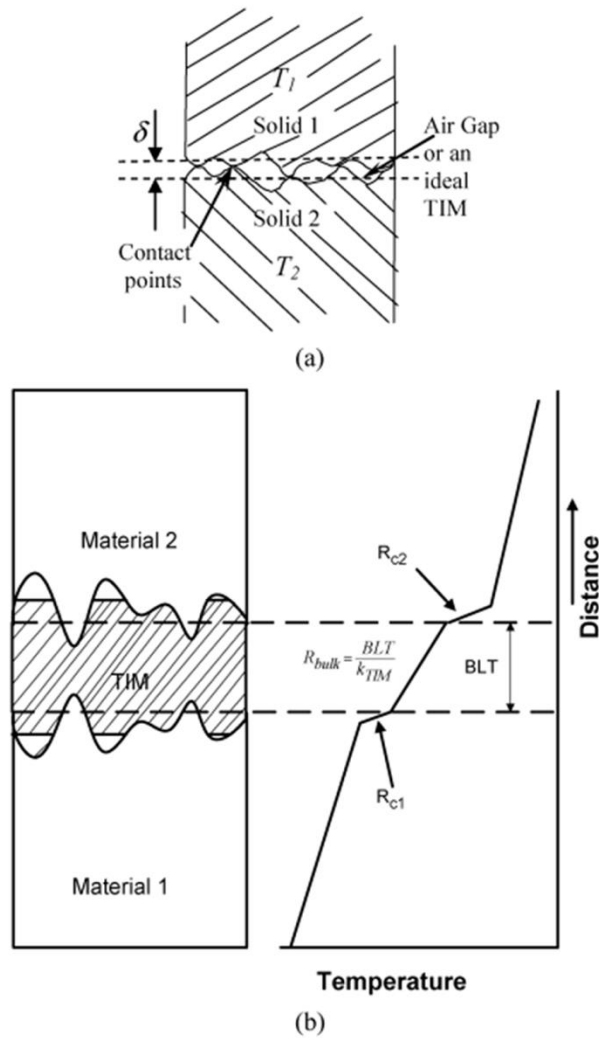
Figure 5.1 (a) Schematic showing that the real contact area is less than the apparent contact area. This figure also represents an ideal TIM that completely fills the gap. (b) Schematic representing of a real TIM.[166]

5.1.2 Carbon-Based TIMs

The past decade has witnessed the rapid development of carbon based TIMs, particularly those based on CNTs and Graphene.[105, 166-194] CNTs have long been thought as an ideal filler for TIMs because of their extremely high intrinsic thermal conductivity

(κ up to 6600 W/mK).[195-198] However, composites fabricated with CNT additives show much worse results than expectation.[199, 200] The reasons for the significant degradation are partially attributed to the large interface thermal resistance across the nanotube-interface.[200-202] In addition, their poor dispersion in polymer matrix also hinders the conductivity enhancement, resulting in much degraded performance.

Researchers have tried different ways to solve these problems. A promising approach is by using vertically aligned carbon nanotubes (VACNTs) instead of those randomly dispersed ones. This method circumvents the dispersion issue to a large extent and the result is greatly improved.[203-206] However, the achieved conductivity is still much lower than expectation. One of the possible reason is the complicated entanglement of individual VACNT and the accompanied large amount of scattering. Besides, the contact resistance is a big issue because of the rigidity of CNTs.

Generally there are few reports about the real application of CNT-based TIMs so far. Their poor performance is one of the main reason; meanwhile, their high price and the high-temperature CVD process have also amplified the difficulty for practical deployment. It is thus unlikely to achieve widespread usage in the industry and the research feat has gradually cooled down.

5.1.3 Graphene TIMs and 3D Graphene TIMs

Graphene has attracted a lot of attention since its discovery due to its excellent electrical, mechanical and thermal properties.[2, 3] Single-layer-graphene (SLG) has an extremely high thermal conductivity of $4.84 \sim 5.30 \times 10^3$ W/mK, much higher than natural materials.[207] Due to the superior thermal property, graphene has been extensively investigated for TIMs in the past decade.[168-175, 178-184, 189-194] This research feat is very

67

similar to that of CNTs due to their excellent intrinsic thermal conductivities. However, graphene offers several other advantages over the latter one. First, graphene is a 2D material, which is less vulnerable to the entanglement problem of 1D CNTs. As a result, the thermal conductivity retains a large portion of its intrinsic value due to reduced internal phonon scattering. For example, W. Cai et al. reported a thermal conductivity of 370 W/mK for supported CVD grown graphene.[193] Meanwhile, 2D graphene is easier to disperse compared with 1D entangled CNTs. It will thus ease the fabrication process. Another important issue is the potential for mass production of graphene, which is critical for practical applications.

The history of graphene-based TIMs is very similar to that utilizing CNTs. The first approaches randomly disperse graphene layers into a polymeric matrix[169, 172] and report thermal conductivities of 5.1[169] and 6.44 W/mK[172] with a loading of 10 and 25 vol%, respectively. These values are much higher than those reported with CNT-based composites; however, they are still much below the expected value due to the interlayer contact resistance.

Different methods are designed to solve the problems caused by contact resistance. For example, inter-connected 3D graphene that eliminates the contact issue is grown by CVD methods.[208] The internal thermal conductivity reaches 0.26~1.7 W/mK of the freestanding 3D graphene network at a solid concentration of 0.45 vol%.[168] Previously our group has fabricated 3D graphene/PDMS composites and achieved a thermal conductivity of 0.56 W/mK at a small loading of 0.7 wt%.[106] Another approach is through architecture design that fully utilizes the extremely high in-plane thermal conductivity of graphene. For example, QZ Liang et al. achieved a thermal conductivity

of up to 112 W/mK by vertically aligning functionalized multilayer graphene structure.[170]

5.1.4 Direct Measurement of Thermal Resistance

For practical applications, the total thermal resistance R_t is more critical. However, from Section 5.1, it is obvious that high thermal conductivity alone cannot guarantee a sound R_t. The contact resistance R_c plays an important role when the materials are rigid and unsmooth, such as the VACNT-based TIMs. Unfortunately, most of the researchers merely report the thermal conductivities of these samples. Generally they will adopt another layer of TIM like soft indium between the substrate and their samples in order to measure their performance. We need to design a material that is readily available for direct deployment.

Here we fabricate a 3D graphene/PDMS TIM and apply it between two Cu pads. Meanwhile, we've also designed a convenient approach for the direct measurement of R_t. Our sample shows a thermal resistance as small as 14 mm^2K/W, much lower than that of pure PDMS contact without the as-fabricated TIM (60 mm^2K/W). What's more, this method is much more convenient compared with the steady-state method for contact resistance measurement.

5.2 Experimental

5.2.1 Growth of 3D Graphene

3D interconnected graphene is grown by a CVD method.[106, 208] Ni foam (1.5 mm thick, 300 mesh) is placed in the quartz tube of a CVD furnace (SGL-1200). It is heated

to 1000℃ at a ramping rate of 16℃/min in an inert atmosphere (Ar 500 *sccm*, H$_2$ 200 *sccm*) and annealed for 5 min. Then CH$_4$ (10 *sccm*) is turned on for 5 min. It is shut off again after the reaction and the sample is cooled down to room temperature at a rapid rate of ~100℃/min.

Freestanding 3D interconnected graphene foam is obtained by etching the Ni foam away. First, a thin layer of poly-methyl methacrylate (PMMA, Mw: 996,000; 4 wt% in ethyl lactate) is drop-coated onto the Ni foams covered with graphene. A protecting layer is formed after dried at 180℃ for 3 h. It is then immersed into a hydrochloric acid solution (HCl, 3 M) at 80℃ for 4 h, during which the Ni foam is etched away by the acid. After that the protective PMMA layer is completely dissolved in a hot acetone (55℃ for 30 min). The sample is fetched out and dried in air, leaving the freestanding graphene network.

5.2.2 Fabrication of pure PDMS TIM and 3D Graphene/PDMS TIMs

For the preparation of 3D graphene/PDMS TIM, the graphene network is placed over a Cu plate (1 × 1 cm^2, 1 mm thick, polished with #1000 sand papers). PMDS (uncured Sylgard 184, Dow Corning. Base/curing agent=10/1 in weight) is dropped onto the network and left for 30 min, during which the bubbles are expelled and the liquid PDMS infiltrates into the holes. An identical Cu pad is then placed exactly on top of the graphene/PDMS with a pressure of 1 MPa. The samples are cured at 80℃ for 4 h.

No graphene is used for the preparation of pure PDMS TIM. Uncured PMDS is dropped onto a Cu plate and left for 30 min. An identical Cu pad is then placed exactly on top of the Cu plate with a pressure of 1 MPa. The samples are cured at 80℃ for 4 h.

5.2.3 LFA Measurement

Both surfaces of the sandwiched sample are coated with a thin carbon layer to enhance the absorption (or emission) to enhance the signal-to-noise ratio. The sandwiched sample is placed in the machine chamber (LFA447 Nanoflash®, Netzsch) to run the test. The data of the rear surface signal is stored and exported to a self-developed analysis program.

5.3 Results and Discussion

5.3.1 3D Graphene/PDMS TIM

Freestanding 3D graphene foam is obtained (Figure 5.2). The interconnected structure of Ni foam is well maintained after the Ni etching and PMMA dissolving process. The TEM image clearly shows a multilayer structure (Figure 5.3). Previously we've achieved a κ of 0.56 W/mK with this 3D graphene/PDMS TIM. In this work, the thermal resistance is measured to be 14 mm^{2}K/W. This result is slightly better than most of the CNTs and VACNTs based TIMs (ranging from 5.2~43 mm^{2}K/W) and comparable to that of commercial thermal greases.[203-205, 209, 210]
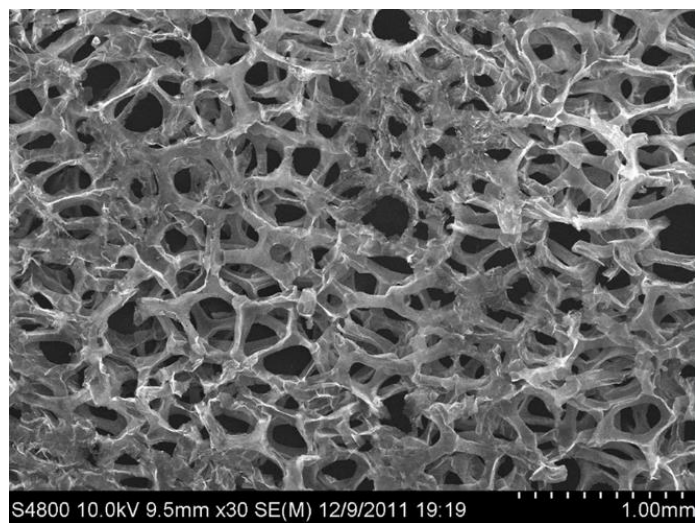
Figure 5.2 Freestanding 3D graphene network.
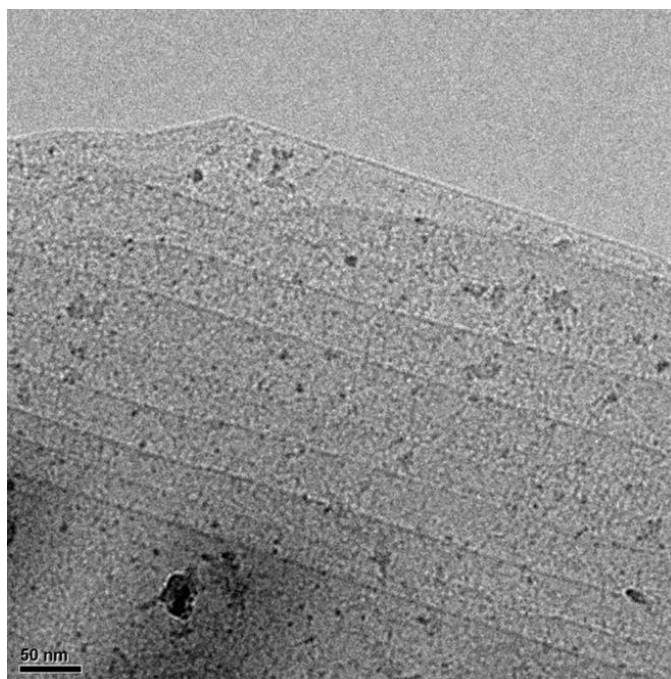
Figure 5.3 TEM image shows a multilayer structure of the 3D graphene sheet.

5.3.2 Mechanism of LFA

Our samples are measured with LFA method. LFA is a non-contact transient thermal measurement method widely used for measuring the thermal diffusivities (α) of a wide range of materials (α ranging from 0.01 to 1000 mm²/s with a reproducibility of about ±3%). The thermal conductivity is derived through Equation 5.2, where ρ is the mass density and C_p is the specific heat at constant pressure.

$$\kappa = \rho \times C_p * \alpha \qquad\qquad 5.2$$

The mechanism of LFA is illustrated in Figure 5.4. A short laser pulse generated by a flash lamp hits the bottom surface of the sample. Both the intensity and the duration of the pulse (100, 400 and 1000 μs for LFA447) can be adjusted in accordance with measured sample. The laser pulse energy is absorbed at the surface. Practically, both sides of the sample surface are coated with a thin layer of carbon to enhance the absorption (or emission) and thus improve the signal-to-noise ratio. The temperature of the rear surface is real-time monitored with an infrared detector, according to which the thermal diffusivity can be derived.

The analytical relation of the rear temperature and time (Figure 5.4b) follows Equation 5.3, where d is the thickness of the sample, $t_{1/2}$ is the time for the rear surface to reach half of the maximum temperature rise.[211]

$$\alpha = \frac{1.37}{\pi^2} \frac{d^2}{t_{1/2}} \qquad\qquad 5.3$$
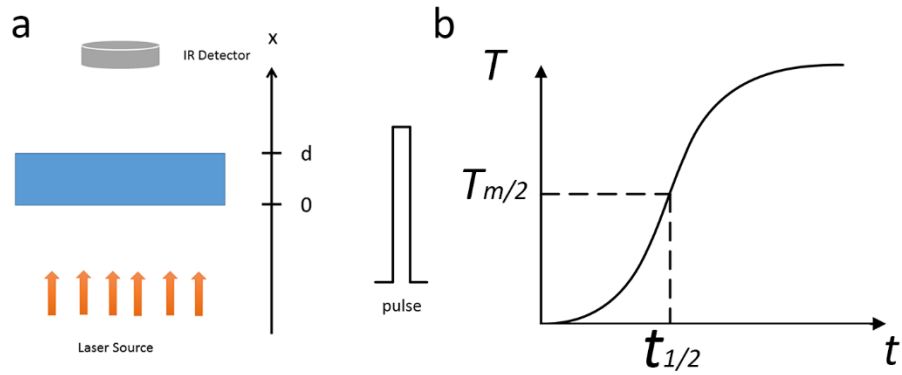
Figure 5.4 The mechanism of the LFA method. (a) A sketch of data acquisition procedure and (b) the profile of the obtained data (not to scale).

5.3.3 Sandwich Model

5.3.3.1 the Mechanism of the Sandwich Model

Previously we've measured the thermal conductivity of our 3D graphene/PDMS TIM.[106] A conductivity of 0.56 W/mK is achieved at a small loading of 0.7 wt%. Here we designed a sandwich model based on the prototype of LFA447 to test its feasibility for practical applications.

The TIM is sandwiched between two smooth Cu pads and the assembly is cured at elevated temperature. Then it is placed into the chamber for test. Figure 5.5a presents an image of the LFA447 machine. The mechanism is illustrated in Figure 5.5b, which is very similar to that designed to measure homogeneous materials (Figure 5.3a). For the derivation of Equation 5.3**Error! Reference source not found.**, four assumptions are proposed:

74
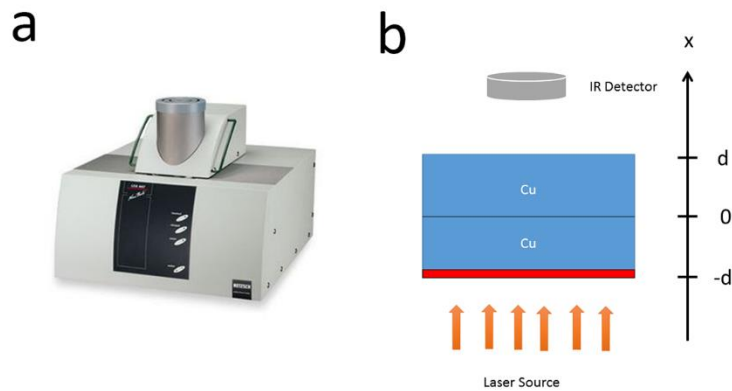
Figure 5.5 (a) An image of LFA447. (b) The illustration of the measurement mechanism. A pulsed-laser is absorbed by a thin layer of Cu at the bottom surface of the sandwiched structure (the red layer).

1. the heat conduction is 1D;

2. the duration of the laser pulse is negligible compared with the characteristic time $t_{1/2}$ and the energy absorption occurs instantaneously;

3. the penetration depth of the laser pulse is negligible;

4. the properties of samples is independent of temperature.

These assumptions are reasonable for our model. In addition, the thickness of our TIM is so small (< 25 μm) that it is reasonable to take it as a non-dimensional resistive layer. As a result, we can derive the thermal resistance based on these five reasonable assumptions.

The heat transfer equation inside the copper pads is:

$$\frac{\partial T(x,t)}{\partial t} = \alpha_{Cu} \frac{\partial^2 T(x,t)}{\partial x^2} \qquad 5.4$$

in which α_{Cu} is the thermal diffusivity of Cu, T is temperature and x is the distance

from the bottom surface.

Adiabatic boundary is chosen because of the short duration that can be tell from the temperature curve. So at the two surfaces, the boundary condition is:

$$\kappa_{Cu} \frac{\partial T(x,t)}{\partial x}\Big|_{x=d} = \kappa_{Cu} \frac{\partial T(x,t)}{\partial x}\Big|_{x=-d} = 0 \qquad \qquad 5.5$$

where κ_{Cu} is the thermal conductivity of Cu.

Energy conservation should be maintained across the interface:

$$Q = \kappa_{Cu} \frac{\partial T(x,t)}{\partial x}\Big|_{x=0^+} = \kappa_{Cu} \frac{\partial T(x,t)}{\partial x}\Big|_{x=0^-} \qquad \qquad 5.6$$

$$R_t \times Q = R_t \times \left(\kappa_{Cu} \frac{\partial T(x,t)}{\partial x}\right)\Big|_{x=0} = T(x,t)\big|_{x=0^-} - T(x,t)\big|_{x=0^+} \qquad 5.7$$

in which R_t is the thermal resistance across the interface and Q is the heat flux.

The initial condition is set to be:

$$T(x,t) = \begin{cases} T_0, (-d < x < -d + l) \\ 0, (-d + l < x < d) \end{cases} \qquad \qquad 5.8$$

in which l is the as-conceived thin absorption layer and T_0 is a constant temperature whose actual value is irrelevant to the result.

5.3.3.2 the Feasibility of the Sandwich Model

The Matlab® code is available in Appendix A. Figure 5.6 shows the results of our simulation with the model described previously, in which the red diamonds represent the data directly obtained from the machine. It is clear that the simulated curves agree well with the experiment (Figure 5.6). As seen from Figure 5.6a, the resistance lies in between 10 to 20 mm²K/W. It is further narrowed down to 12~15 mm²K/W, in which 14 mm²K/W gives the smallest deviation (Figure 5.6b).

Our method is also verified with an infrared thermometry method described elsewhere[212]. Briefly, the sample is sandwiched between a heating source with controlled power P and a cooling source with constant temperature. The system is left to equilibrium and an infrared thermometer is used to monitor the temperature across from the side view. The temperature of a small rectangular area near the interface is averaged, by which the temperature difference across the interface is obtained. Finally, the thermal resistance is obtained by $R = \frac{\Delta T \times A}{P}$, where A is the area of the sample.
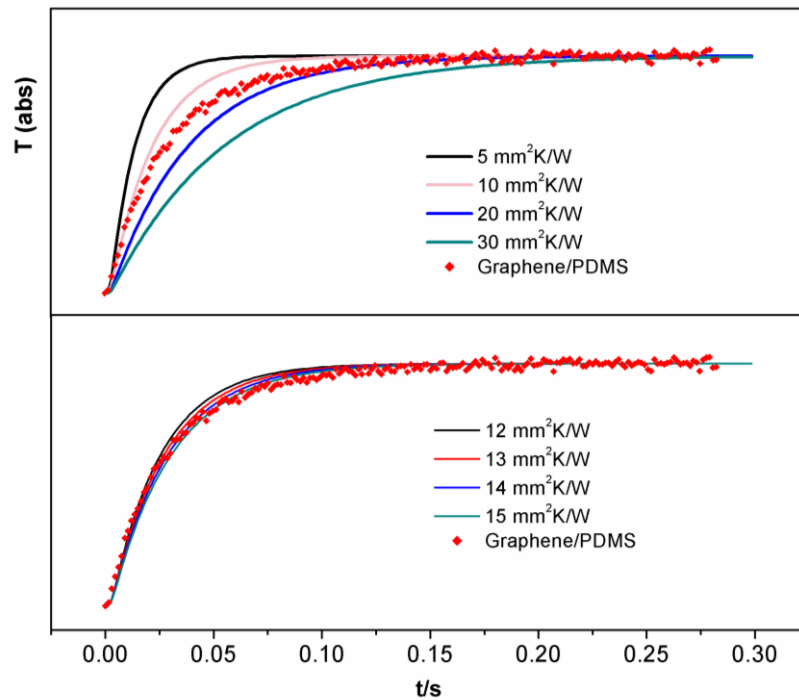
Figure 5.6 Deriving the thermal resistance of 3D graphene/PDMS TIM from the data obtained with LFA447. (a) Four curves simulated with Rc of 5, 10, 20 and 30 mm²K/W. It suggests that R_c lies between 10 and 20 mm²K/W. (b) R_c is further narrowed down to 12~15 mm²K/W. The blue diamonds represent the data obtained from the equipment.

The thermal resistance of our sample is measured to be 12 mm^{2}K/W with this steady-state method, which is very close to the value obtained with our model. What's more, it takes much shorter time for our method since it does not need to wait for the equilibrium of the system. Thus we can conclude that our model is feasible and practical for the measurement of thermal interface resistance.
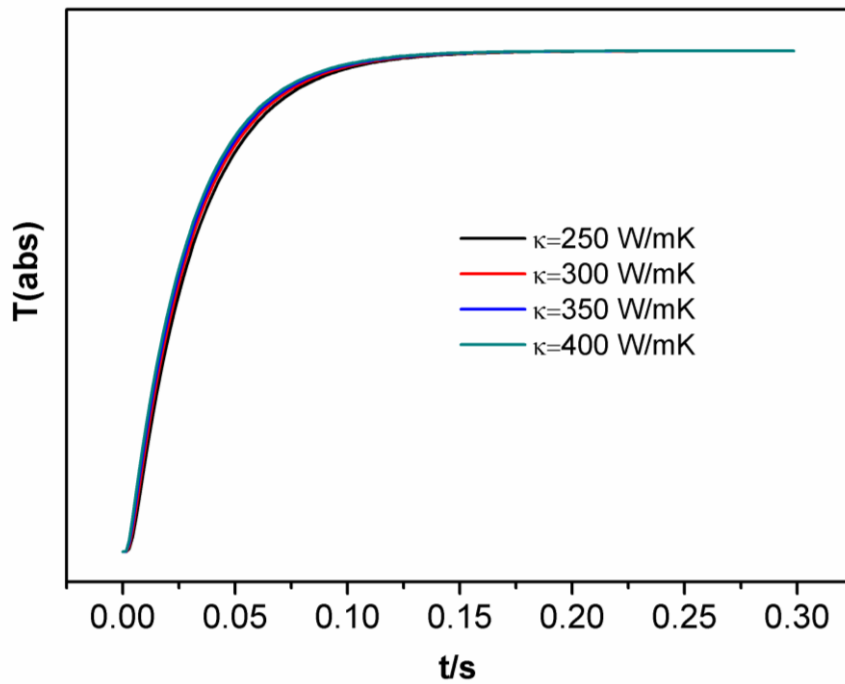
Figure 5.7 The stability test. κ_{Cu} is set to 250, 300, 350 and 400 W/mK, respectively. No significant deviation is obtained from the result.

5.3.3.3 the Stability and Reliability of the Sandwich Model

The stability of our model is also justified. The thermal interface resistance is much larger compared with that of pure Cu. As a result, the exact thermal conductivity of Cu

will not interfere as long as it is large enough. This is also supported with simulations (Figure 5.7). This phenomenon offers a convenient choice of substrates as long as its thermal conductivity is large enough.

Besides, the reliability of our codes is also checked. The iteration times is increased from 3000 to 30000, while the simulated curve are identical to each other (Figure 5.8). It thus indicates that our model is convergent and reliable for usage.

5.3.4 Thermal Resistance of PDMS and Graphene/PDMS TIM

The total thermal Resistance of our sample with the graphene/PDMS TIM is calculated to be 14 mm^{2}W/K with our model, which agrees well with that obtained with the traditional steady-state infrared thermometry method. This value is comparable to those commercial products. As a comparison, the TIM without the addition of 3D graphene network shows a much inferior thermal resistance of 60 mm^{2}W/K (Figure 5.9). These results suggest that the thermal interface is greatly improved with the addition of small loading of 3D graphene network. It also indicates that our graphene/PDMS TIM is of great potentail to be used in real applications.
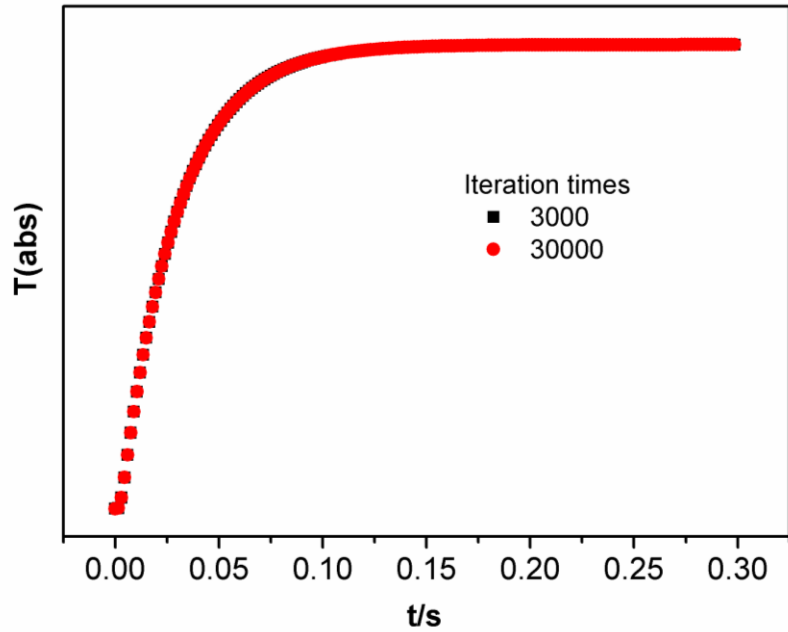
Figure 5.8 Stability test. Iteration numbers is increased from 3000 to 30000, yet the simulated curves remain identical to each other.
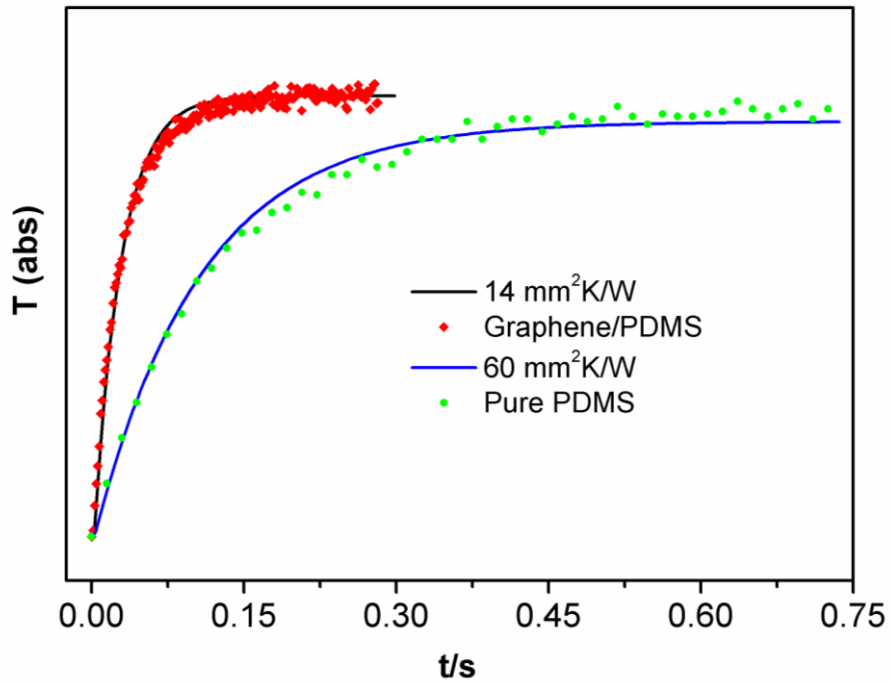
Figure 5.9 The estimated thermal resistance of 3D graphene/PDMS TIM and pure PDMS TIM. The curves are simulated with R_c= 14 and 60 mm²K/W, respectively, indicating a much improved thermal interface with the addition of 3D graphene.

80

The reason of the improvement with 3D graphene is attributed to the superior thermal conductivity of graphene as well as the 3D interconnected structure. In this way, the interfacial resistance between the graphene layers generally existed in common graphene composites is minimized. In addition, the great compliance of the graphene/PDMS TIM also helps enhance the performance.

5.4 Conclusion

In summary, we proved that the CVD grown 3D graphene/PDMS composite is able to be directly used as TIM. The thermal resistance is as small as 14 mm^2K/W, comparable to those of commercial products. What's more, we developed a convenient approach for measuring the thermal resistance. This transient method is easy to operate, which takes much less than 10 min for sample preparation and measurement. The data analysis procedure will take less than 5 min to run. As a result, it saves much time compared with the steady-state method that generally consumes a lot of time for equilibrium. In addition, the non-contact attribute will avoid contamination to the equipment.

In our model, we assumed that the TIM is extremely thin that it can be taken as a pure resistance layer for convenience. However, this sandwich model is also easily developed to accommodate the measurement for samples with finite thickness. We can measure the thermal conductivity of TIM sample first. After that we can derive the contact resistance of thick TIMs with a modified model using the same boundary and initial conditions.

CHAPTER 6   FUTURE WORK

6.1 Graphene-based Supercapacitors and MSCs

We have demonstrated that the electrochemical active benzene derivatives will greatly enhance the specific capacitance of graphene-based supercapacitors. Meanwhile, the reason for the increase has been identified to the configuration of the aromatic chemicals. *Para* and *ortho* configuration and the accompanied redox reactions are critical for the increase.

The next step is looking for suitable benzene derivatives additives to further increase the capacitance, which is more convenient with the above-mentioned conclusions. For example, we predict that 1,2,4-benzenetriamine contributes more than 1,3,5-benzenetriamine. In addition, the benzene derivatives bind to the rGO surface via π-π interaction. Thus providing the same conditions, naphthalene based derivatives should perform better than similar aromatic counterparts due to stronger π-π binding force.

In our work, we focus on the mechanism study behind the capacitance enhancement. Meanwhile, we can also adopt the methods reported in literature to further increase the performance. Those methods such as hydrothermal reactions, although misinterpreted, still improve the performance a lot. With the comparison of different methods, it is highly possible to develop a product with excellent performance.

6.2 Scalable Production of Flexible ac Line-Filters

Graphene have been investigated as the electrode material for ac line-filters. In Chapter 4, we present a novel way to fabricate ac line-filters based on rGO. This method is scalable, convenient and compatible with flexible substrates. However, it involves an e-beam lithography procedure that may add up the fabrication cost. A more cost-effective approach will be more suitable for industry applications.
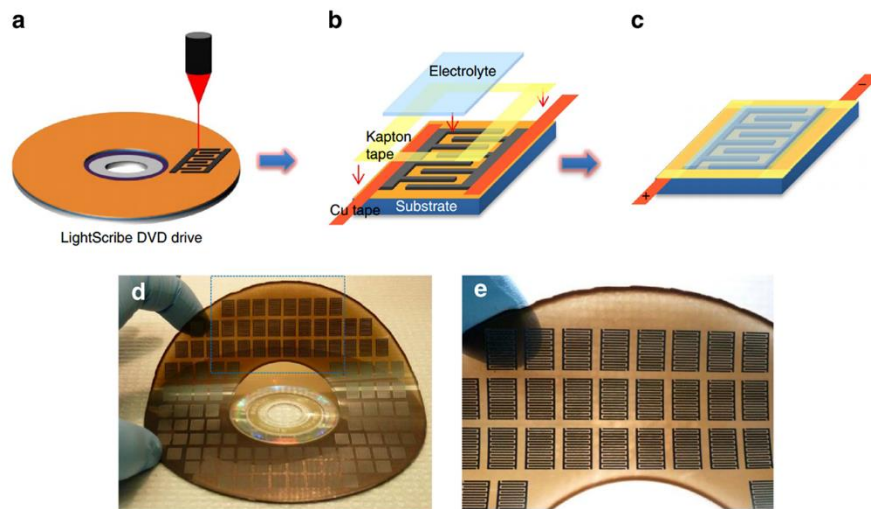
Figure 6.1 The fabrication process of LSG-based MSC. (a–c) The schematic diagram showing the fabrication process for an LSG-based MSC. (d,e) More than 100 flexible micro-devices can be produced on a single run.[46]

In our previous work, we find that the electrical conductive attribute, the interdigit pattern and open-porous structure of rGO are the three critical for high factors performance line-filtering. As a result, it is highly likely that we can achieve better performance if the three factors are maintained or improved. This concept can be fulfilled with much more convenient yet feasible engineering.
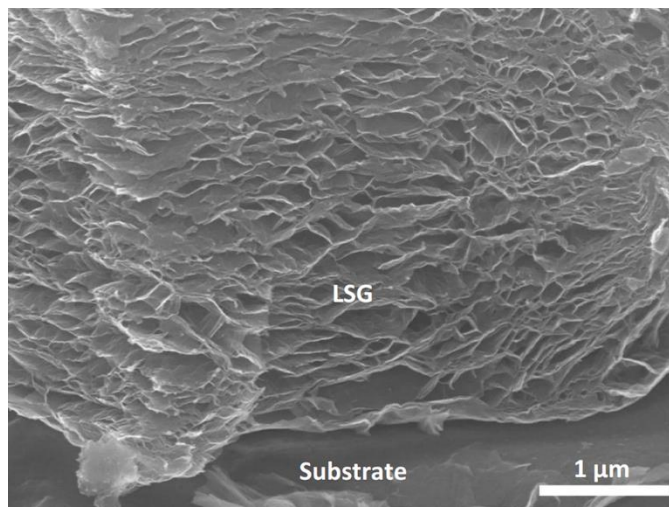
Figure 6.2 A SEM image of the LSG that clearly show an interconnected open-porous microscopic structure.[46]

Currently we are working on two different yet similar approaches for this project, one is light-scribing and the other is mask-patterned photo-reduction. Light reduction[45] and DVD light-scribing[46-49] of GO are widely investigated, especially for supercapacitors, electronics and photo-catalytic applications. When photons hit the GO surface, some of them will be absorbed and turned into heat, increasing the temperature. If the light intensity and accompanied energy density are large enough, the rapid temperature increase will be able to decompose the function groups of GO in the form of gas. The rapid leakage of decomposed gas will expand the graphene layers, producing an open-porous interconnected conductive rGO structure.

Figure 6.1 presents the schematic diagram showing the fabrication process of LSG-based MSC.[46] More than 100 MSCs can be produced in a single run of about 30 min. This method eliminates the necessity of the e-beam lithography procedure and will greatly reduce the fabrication cost. SEM microscopic structure of the as-produced LSG

clearly shows an interconnected open-porous structure that is beneficial for both high electrical conductivity and small ion transport barrier (Figure 6.2).[46] As a result, the as-fabricated MSC exhibits a small τ_0 of 20 ms with a gelled PVA/H$_2$SO$_4$ electrolyte.

In our previous research of flexible MSC and ac line-filter, we find that the electrolyte plays an important role in ac line-filters. τ_0 will decrease from 20 to 1.9 ms if the gelled PVA/ H$_2$SO$_4$ electrolyte is replaced with the aqueous H$_2$SO$_4$ electrolyte. As a result, it is possible that we can achieve a comparable rate performance if the gelled PVA/ H$_2$SO$_4$ electrolyte in LSG-based MSC is replaced with aqueous electrolyte.

Another approach also utilizes the light reducing mechanism (Figure 6.3). An interdigit-patterned photomask is fabricated in this approach, which is then placed over the GO film (step I). A flash light passes through the interdigit pattern, by which GO in the exposed area will be reduced (step II). Finally, the photomask is removed and the pattern will be used as the electrode material for flexible ac line-filters after being filled with aqueous electrolyte (step III).
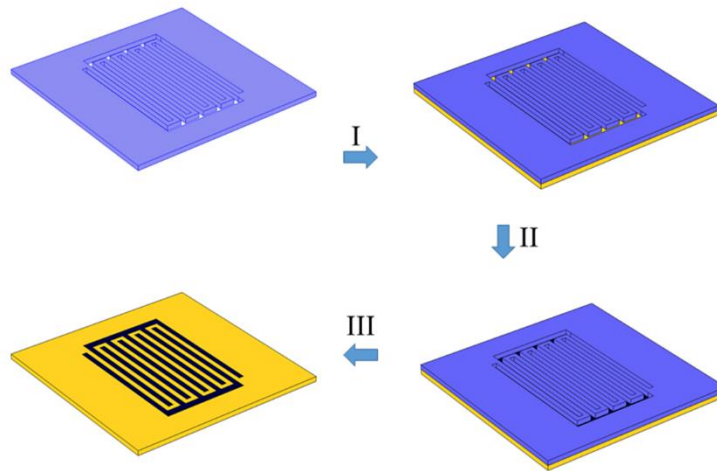
Figure 6.3 The fabrication mechanism utilizing patterned light-reduction. An interdigit-patterned photomask is placed over a thin GO film (step I); a flash light passes through the interdigit to reduce the exposed area of the GO film (step II); the photomask is removed in the last step (step III).

6.3 Vertically-Aligned rGO for High Performance TIMs

In Chapter 5, we have presented a feasible way to fabricate 3D graphene/PDMS TIM. The overall thermal resistance is comparable to those of commercial products. However, the thermal conductivity is much lower, which is not feasible for thicker TIMs required in un-ideal applications.

Graphene has been engineered into vertically aligned structure and shows excellent thermal conductivity (up to 112 W/mK).[170] However, this method is extremely tedious. It requires great effort for cutting the layered graphene sheets into small stripes and flipping them vertical one-by-one. Thus it is unfeasible to obtain a uniform and flat surface in this way, not to mention industrial deployment. Currently we are working on a scalable approach to produce vertically aligned reduced graphene oxide (VArGO)-based TIMs with high thermal conductivity.

First, a uniform GO thin film is fabricated with a convenient scalable method

(Figure 6.4).[213] In this wet-spinning approach GO solution is inject-pumped into a coagulation bath that contracted GO sheets into well aligned GO films. Figure 6.4b-c present the production setup and the as-produced GO film.
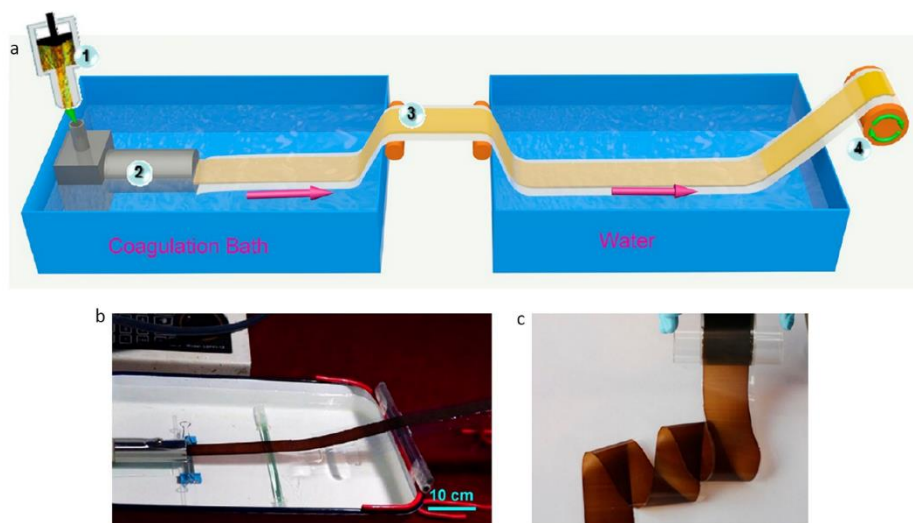
Figure 6.4 Wet-spinning of continuous GO film. (a) The schematic protocol: (1) the GO dispersion goes through an injector (2) a spinning channel (3) a coagulated GO gel film and (4) a film wind-up reel successively. (b) The wet-spinning setup. (c) The as-produced continuous GO film.[213]

After that, the GO film is rolled, cut and reduced into VArGO (Figure 6.5 and Figure 6.6).[139] The as-produced VArGO shows similar vertically aligned structure that will utilize the excellent in-plane thermal conductivity of graphene. All the procedures in this approach is scalable and readily available for industrial applications. Thus it is promising to be used as the next generation high performance TIM.
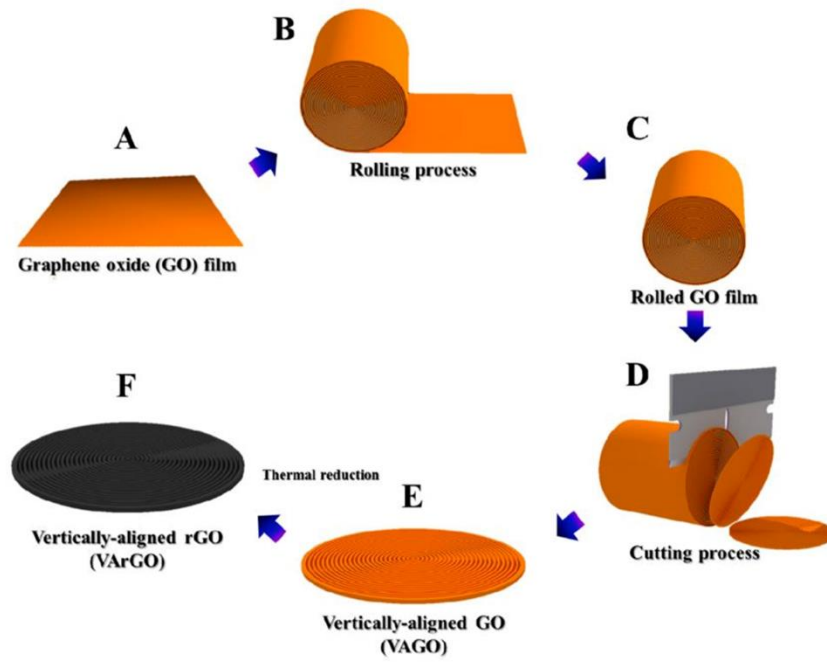
Figure 6.5 The fabrication process of VArGO (modified procedure).[139]
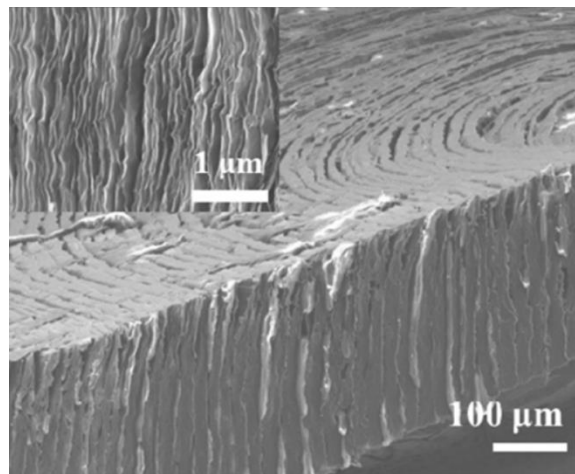
Figure 6.6 SEM image of VArGO.[139]

APPENDIX A: THE MATLAB® CODE FOR R_C CALCULATION

```
function [Temperature,
T_Backside]=ThermalResistanceModel(ThermalResistance,filename,TimeScale)

%{
This is a program that measures the thermal resistance (mm^2K/W) of Sandwich
Models using LFA447. ThermalResistance is the predicted value of thermal resistance.
By setting the thermal resistance to certain value, the simulated T_backside is
compared with the original Temperature data obtained from machine.

    In this model, the TIM comprises of a pure resistive layer sandwiched by two
square copper pads. Five assumptions are made:

        1. the heat conduction is 1D;
        2. the duration of the laser pulse is negligible compared with the
characteristic time t_(1/2) and the energy absorption occurs instantaneously;
        3. the penetration depth of the laser pulse is negligible;
        4. the properties of samples is independent of temperature;
        5. the sample is pure resistive layer.


    It takes the following steps:
        1. Load the LFA447 data into the program.
        2. Initiate the Temperature vector.
        3. Solve the equation.

%}
%%
%{
Step One: Load the data
    Temperature vs. Time
    N_data is the number of data points. It records the Temperature evolution at
the backside of trilayer sample. TimeScale is the time interval LFA447 takes to record
data (ms).
%}
%%
OriginalData=importdata(filename);
[rows,columns]=size(OriginalData);
TotalLength=rows*columns;
Degeneracy=10;
TimeInterval=TimeScale*Degeneracy/1000;


N_data=TotalLength/Degeneracy;
```

```
    X(1:rows*columns)=0;
    Y(1:rows*columns)=0;
        for i=1:rows
            for j1=1:columns
                    X((i-1)*columns +j1)=((i-1)*columns +j1)*TimeScale/1000;
                    Y((i-1)*columns +j1)=OriginalData(i,j1);
            end
        end

    Time(1:N_data)=0;
    Temperature(1:N_data)=0;
        for i=1:N_data
            Time(i)=sum(X((i-1)*Degeneracy+1:(i*Degeneracy)))/Degeneracy;

Temperature(i)=sum(Y((i-1)*Degeneracy+1:(i*Degeneracy)))/Degeneracy;
        end

    %%
    %{
    Step Two: Initiate Temperature
        Load the temperature distribution at the time 0, which is the initial condition.
        At the beginning, a thin layer of Cu is set to a finite temperature T and the rest
is set to 0.
        Adiabatic boundary condition is assumed in our modeling. The distance between
data points is set to 20um in this case, which can be adjusted for other problems.
    %}

    L_left=0.001;
    L_right=0.001;
    Distance=2*10^(-5);

    N_left=L_left/Distance+1;
    N_right=L_right/Distance+1;
    N_high=7;

    N_points=N_left+N_right;
    T_ini(1:N_points)=0;

    T_avg=
sum(Temperature(round(N_data/2):N_data))/(N_data-round(N_data/2)+1);
    T_high=T_avg*(N_points-2)^2/(N_points*(N_high-1));

    T_ini(1:N_high)=T_high;

    %%
    %{
```

Step Three: Solve the equations through Gauss Elimination

The evolution of temperature at the end point of the sample is simulated with the ThermalResistance value we set, which can be compared with the original data obtained from the machine.

By changing the ThermalResistance value, we can find the minimum differences between the simulated and original data. This point is the thermal resistance of our sample.

```
%}

%%    Copper parameters
ThermalConductivity_Cu=400;
Density_Cu=8900;
HeatCapacity_Cu=390;
ThermalResistance_Real=ThermalResistance*10^(-6);
ThermalDiffusivity_Cu=ThermalConductivity_Cu/(Density_Cu*HeatCapacity_
Cu);

N=length(T_ini);
L_left=0.001;
L_right=0.001;
Distance=(L_left+L_right)/(N-2);
IterationNumber=3*10^3;

Delta_x=Distance;
Delta_t=TimeInterval/IterationNumber;

k1=ThermalDiffusivity_Cu*Delta_t/(Delta_x)^2;
k2=ThermalConductivity_Cu*ThermalResistance_Real/Delta_x;
A(1:N,1:N)=0;

%

%% Initialization of matrix and vector.
%
A(1,1)=1;
A(1,2)=-1;
A(N,N-1)=1;
A(N,N)=-1;
A(N/2,N/2-1)=-k2;
A(N/2,N/2)=1+k2;
A(N/2,N/2+1)=-1;
A(N/2+1,N/2)=-1;
A(N/2+1,N/2+1)=1+k2;
A(N/2+1,N/2+2)=-k2;
T=T_ini;
```

```
    for i=2:N/2-1
         A(i,i-1)=-k1/2;
         A(i,i)=1+k1;
         A(i,i+1)=-k1/2;
    end

    for i=N/2+2:N-1
         A(i,i-1)=-k1/2;
         A(i,i)=1+k1;
         A(i,i+1)=-k1/2;
    end
%% To assign the data to new one for iteration.
    function B_sub=iterateT(T_sub,k1)

         N_sub=length(T_sub);
         B_sub(1:N_sub)=0;
         for j=2:N_sub/2-1
              B_sub(j)=(T_sub(j-1)+T_sub(j+1))*k1/2+(1-k1)*T_sub(j);
         end
         for j=N_sub/2+2:N_sub-1
              B_sub(j)=(T_sub(j-1)+T_sub(j+1))*k1/2+(1-k1)*T_sub(j);
         end
         B_sub(1)=0;
         B_sub(N_sub)=0;
         B_sub(N_sub/2)=0;
         B_sub(N_sub/2+1)=0;
    end

%% To solve the tri_diagonal matrix problem
 function X_sub=Tri_Diagonal(A_sub,B_sub)

         N_sub=length(B_sub);
         X_sub(1:N_sub)=0;
         for k=2:N_sub

A_sub(k,k)=A_sub(k,k)-A_sub(k-1,k)*A_sub(k,k-1)/A_sub(k-1,k-1);
              B_sub(k)=B_sub(k)-B_sub(k-1)*A_sub(k,k-1)/A_sub(k-1,k-1);
              A_sub(k,k-1)=0;
         end

         for k=1:N_sub-1

B_sub(N_sub-k)=B_sub(N_sub-k)-B_sub(N_sub-k+1)*A_sub(N_sub-k,N_sub-k+1)/
A_sub(N_sub-k+1,N_sub-k+1);
              A_sub(N_sub-k,N_sub-k+1)=0;
         end
```

```
            for k=1:N_sub
                X_sub(k)=B_sub(k)/A_sub(k,k);
            end
    end

%% Solve the problem using Crank-Nicolson form.
T_Backside(1:N_data)=0;
for j2=1:N_data
    T_Backside(j2)=T(N);
    for i=1:IterationNumber
        B=iterateT(T,k1);
        T=Tri_Diagonal(A,B);
    end
end

end
```

APPENDIX B: AUTHOR'S PUBLICATIONS

[1] **Wu, Z. K.**; Lin, Z. Y.; Li, L. Y.; Song, B.; Moon, K. S.; Bai, S. L.; Wong, C. P., Flexible micro-supercapacitor based on in-situ assembled graphene on metal template at room temperature. Nano Energy 10, 222-228 (2014).

[2] **Wu, Z. K.**; Li, L. Y.; Lin, Z. Y.; Song, B.; Li Z.; Moon, K. S.; Bai, S. L.; Wong, C. P., Alternating current line-filter based on electrochemical capacitor utilizing template-patterned graphene, accepted by Scientific Reports.

[3] **Wu, Z. K.**; Lin, Z. Y.; Li, L. Y.; Song, B.; Tuan, C. C.; Li Z.; Moon, K. S.; Bai, S. L.; Wong, C. P., Capacitance enhancement by electrochemically active benzene derivatives for graphene-based supercapacitors, submitted to RSC Advances.

[4] **Wu, Z. K.**; Moon, K. S.; Bai, S. L.; Wong, C. P., In situ reduced graphene oxide for Cu protection, The First International Conference on Nanoenergy and Nanosystems 637, (2014).

[5] Zhao, Y. H.; **Wu, Z. K.**; Bai, S. L.; Study on thermal properties of graphene foam/graphene sheets filled polymer composites, Composites Part A: Applied Science and Manufacturing 72, 200-206 (2015).

[6] Li, Z., Song, B.; **Wu, Z. K.**; Lin, Z. Y.; Yao, Y. G.; Moon, K. S.; Wong, C. P., 3D porous graphene with ultrahigh surface area for microscale capacitive deionization. Nano Energy 11, 711-718 (2015).

[7] Li, Z.; Le, T. R.; **Wu, Z. K.**; Yao, Y. G.; Li, L. Y.; Tentzeris, M.; Moon, K. S.; Wong, C. P.,Rational Design of a Printable, Highly Conductive Silicone-based Electrically Conductive Adhesive for Stretchable Radio-Frequency Antennas. Advanced Functional Materials 25 (3), 464-470 (2015).

REFERENCES

[1] Novoselov, K.S., A.K. Geim, S. Morozov, D. Jiang, Y. Zhang, S. Dubonos, I. Grigorieva, and A. Firsov, Electric field effect in atomically thin carbon films. Science 306 (5696), 666-669 (2004).

[2] Novoselov, K., A.K. Geim, S. Morozov, D. Jiang, M. Katsnelson, I. Grigorieva, S. Dubonos, and A. Firsov, Two-dimensional gas of massless Dirac fermions in graphene. Nature 438 (7065), 197-200 (2005).

[3] Geim, A.K. and K.S. Novoselov, The rise of graphene. Nature Materials 6 (3), 183-191(2007).

[4] Partoens, B. and F. Peeters, From graphene to graphite: Electronic structure around the K point. Physical Review B 74 (7), 075404 (2006).

[5] Saito, R., A. Jorio, A. Souza Filho, G. Dresselhaus, M. Dresselhaus, and M. Pimenta, Probing phonon dispersion relations of graphite by double resonance Raman scattering. Physical Review Letters 88 (2), 027401 (2001).

[6] Lee, C., X. Wei, J.W. Kysar, and J. Hone, Measurement of the elastic properties and intrinsic strength of monolayer graphene. Science 321(5887), 385-388 (2008).

[7] Stoller, M.D., S. Park, Y. Zhu, J. An, and R.S. Ruoff, Graphene-based ultracapacitors. Nano letters 8 (10), 3498-3502 (2008).

[8] Kim, S., J. Nah, I. Jo, D. Shahrjerdi, L. Colombo, Z. Yao, E. Tutuc, and S.K. Banerjee, Realization of a high mobility dual-gated graphene field-effect transistor with Al_2O_3 dielectric. Applied Physics Letters 94 (6), 062107-062107-3 (2009).

[9] Meric, I., M.Y. Han, A.F. Young, B. Ozyilmaz, P. Kim, and K.L. Shepard, Current saturation in zero-bandgap, top-gated graphene field-effect transistors. Nature Nanotechnology 3 (11), 654-659 (2008).

[10] Wu, J., H.A. Becerril, Z. Bao, Z. Liu, Y. Chen, and P. Peumans, Organic solar cells with solution-processed graphene transparent electrodes. Applied Physics Letters 92 (26), 263302 (2008).

[11] Kim, K.S., Y. Zhao, H. Jang, S.Y. Lee, J.M. Kim, K.S. Kim, J.-H. Ahn, P. Kim, J.-Y. Choi, and B.H. Hong, Large-scale pattern growth of graphene films for stretchable transparent electrodes. Nature 457 (7230), 706-710 (2009).

[12] Bae, S., H. Kim, Y. Lee, X. Xu, J.-S. Park, Y. Zheng, J. Balakrishnan, T. Lei, H.R. Kim, and Y.I. Song, Roll-to-roll production of 30-inch graphene films for transparent electrodes. Nature Nanotechnology 5 (8), 574-578 (2010).

[13] Ang, P.K., W. Chen, A.T.S. Wee, and K.P. Loh, Solution-gated epitaxial graphene as pH sensor. Journal of the American Chemical Society 130 (44), 14392-14393 (2008).

[14] Yoon, H.J., J.H. Yang, Z. Zhou, S.S. Yang, and M.M.-C. Cheng, Carbon dioxide gas sensor using a graphene sheet. Sensors and Actuators B: Chemical 157 (1), 310-313 (2011).

[15] Geim, A.K., Graphene: status and prospects. Science 324 (5934), 1530-1534 (2009).

[16] Zhu, J., Graphene production: New solutions to a new problem. Nature Nanotechnology 3 (9), 528-529 (2008).

[17] Green, A.A. and M.C. Hersam, Solution phase production of graphene with controlled thickness via density differentiation. Nano Letters 9 (12), 4031-4036 (2009).

[18] Lotya, M., P.J. King, U. Khan, S. De, and J.N. Coleman, High-concentration, surfactant-stabilized graphene dispersions. ACS Nano 4 (6), 3155-3162 (2010).

[19] Notley, S.M., Highly concentrated aqueous suspensions of graphene through ultrasonic exfoliation with continuous surfactant addition. Langmuir 28 (40), 14110-14113 (2012).

[20] Khan, U., H. Porwal, A. O'Neill, K. Nawaz, P. May, and J.N. Coleman, Solvent-exfoliated graphene at extremely high concentration. Langmuir 27 (15), 9077-9082 (2011).

[21] O'Neill, A., U. Khan, P.N. Nirmalraj, J. Boland, and J.N. Coleman, Graphene dispersion and exfoliation in low boiling point solvents. The Journal of Physical Chemistry C 115 (13), 5422-5428 (2011).

[22] Oyer, A.J., J.-M.Y. Carrillo, C.C. Hire, H.C. Schniepp, A.D. Asandei, A.V. Dobrynin, and D.H. Adamson, Stabilization of graphene sheets by a structured benzene/hexafluorobenzene mixed solvent. Journal of the American Chemical Society 134 (11), 5018-5021 (2012).

[23] Khan, U., A. O'Neill, M. Lotya, S. De, and J.N. Coleman, High-Concentration Solvent Exfoliation of Graphene. Small 6 (7), 864-871 (2010).

[24] Park, K.H., B.H. Kim, S.H. Song, J. Kwon, B.S. Kong, K. Kang, and S. Jeon, Exfoliation of non-oxidized graphene flakes for scalable conductive film. Nano letters 12 (6), 2871-2876 (2012).

[25] Sampath, S., A.N. Basuray, K.J. Hartlieb, T. Aytun, S.I. Stupp, and J.F. Stoddart, Direct Exfoliation of Graphite to Graphene in Aqueous Media with Diazaperopyrenium Dications. Advanced Materials 25 (19), 2740-2745 (2013).

[26] Su, X., G. Wang, W. Li, J. Bai, and H. Wang, A simple method for preparing graphene nano-sheets at low temperature. Advanced Powder Technology 24 (1), 317-323 (2013).

[27] Paton, K.R., E. Varrla, C. Backes, R.J. Smith, U. Khan, A. O'Neill, C. Boland, M. Lotya, O.M. Istrate, and P. King, Scalable production of large quantities of defect-free few-layer graphene by shear exfoliation in liquids. Nature Materials 13 (6), 624-630 (2014).

[28] Paton, K.R., E. Varrla, V. Nicolosi, and J.N. Coleman. Scale-up of Liquid Phase Exfoliation of Graphene. Chem on Tubes (2014).

[29] Berger, C., Z. Song, T. Li, X. Li, A.Y. Ogbazghi, R. Feng, Z. Dai, A.N. Marchenkov, E.H. Conrad, and P.N. First, Ultrathin epitaxial graphite: 2D electron gas properties and a route toward graphene-based nanoelectronics. The Journal of Physical

Chemistry B 108 (52), 19912-19916 (2004).

[30] Reina, A., X. Jia, J. Ho, D. Nezich, H. Son, V. Bulovic, M.S. Dresselhaus, and J. Kong, Large area, few-layer graphene films on arbitrary substrates by chemical vapor deposition. Nano Letters 9 (1), 30-35 (2008).

[31] Sutter, P.W., J.-I. Flege and E.A. Sutter, Epitaxial graphene on ruthenium. Nature Materials 7 (5), 406-411 (2008).

[32] Pletikosić, I., M. Kralj, P. Pervan, R. Brako, J. Coraux, A. N'diaye, C. Busse, and T. Michely, Dirac cones and minigaps for graphene on Ir (111). Physical Review Letters 102 (5), 056808 (2009).

[33] Li, X., W. Cai, J. An, S. Kim, J. Nah, D. Yang, R. Piner, A. Velamakanni, I. Jung, and E. Tutuc, Large-area synthesis of high-quality and uniform graphene films on copper foils. Science 324 (5932), 1312-1314 (2009).

[34] Dreyer, D.R., S. Park, C.W. Bielawski, and R.S. Ruoff, The chemistry of graphene oxide. Chemical Society Reviews 39 (1), 228-240 (2010).

[35] Paredes, J., S. Villar-Rodil, A. Martinez-Alonso, and J. Tascon, Graphene oxide dispersions in organic solvents. Langmuir 24 (19), 10560-10564 (2008).

[36] Chen, W., L. Yan and P.R. Bangal, Preparation of graphene by the rapid and mild thermal reduction of graphene oxide induced by microwaves. Carbon 48 (4), 1146-1152 (2010).

[37] Zhu, Y., M.D. Stoller, W. Cai, A. Velamakanni, R.D. Piner, D. Chen, and R.S. Ruoff, Exfoliation of graphite oxide in propylene carbonate and thermal reduction of the resulting graphene oxide platelets. ACS Nano 4 (2), 1227-1233 (2010).

[38] Becerril, H.A., J. Mao, Z. Liu, R.M. Stoltenberg, Z. Bao, and Y. Chen, Evaluation of solution-processed reduced graphene oxide films as transparent conductors. ACS Nano 2 (3), 463-470 (2008).

[39] Gao, X., J. Jang and S. Nagase, Hydrazine and thermal reduction of graphene oxide: reaction mechanisms, product structures, and reaction design. The Journal of Physical Chemistry C 114 (2), 832-842 (2009).

[40] Zhu, Y., S. Murali, W. Cai, X. Li, J.W. Suk, J.R. Potts, and R.S. Ruoff, Graphene and graphene oxide: synthesis, properties, and applications. Advanced Materials 22 (35), 3906-3924 (2010).

[41] McAllister, M.J., J.-L. Li, D.H. Adamson, H.C. Schniepp, A.A. Abdala, J. Liu, M. Herrera-Alonso, D.L. Milius, R. Car, and R.K. Prud'homme, Single sheet functionalized graphene by oxidation and thermal expansion of graphite. Chemistry of Materials 19 (18), 4396-4404 (2007).

[42] Zhou, Y., Q. Bao, L.A.L. Tang, Y. Zhong, and K.P. Loh, Hydrothermal dehydration for the "green" reduction of exfoliated graphene oxide to graphene and demonstration of tunable optical limiting properties. Chemistry of Materials 21 (13), 2950-2956 (2009).

[43] Long, D., W. Li, L. Ling, J. Miyawaki, I. Mochida, and S.-H. Yoon, Preparation of

nitrogen-doped graphene sheets by a combined chemical and hydrothermal reduction of graphene oxide. Langmuir 26 (20), 16096-16102 (2010).

[44] Xu, Y., K. Sheng, C. Li, and G. Shi, Self-assembled graphene hydrogel via a one-step hydrothermal process. ACS Nano 4 (7), 4324-4330 (2010).

[45] Cote, L.J., R. Cruz-Silva and J. Huang, Flash reduction and patterning of graphite oxide and its polymer composite. Journal of the American Chemical Society 131 (31), 11027-11032 (2009).

[46] El-Kady, M.F. and R.B. Kaner, Scalable fabrication of high-power graphene micro-supercapacitors for flexible and on-chip energy storage. Nature Communications 4, 1475 (2013).

[47] El-Kady, M.F. and R.B. Kaner, Direct Laser Writing of Graphene Electronics. ACS Nano 8 (9), 8725-8729 (2014).

[48] El-Kady, M.F., V. Strong, S. Dubin, and R.B. Kaner, Laser scribing of high-performance and flexible graphene-based electrochemical capacitors. Science 335 (6074), 1326-1330 (2012).

[49] Gao, W., N. Singh, L. Song, Z. Liu, A.L.M. Reddy, L. Ci, R. Vajtai, Q. Zhang, B. Wei, and P.M. Ajayan, Direct laser writing of micro-supercapacitors on hydrated graphite oxide films. Nature Nanotechnology 6 (8), 496-500 (2011).

[50] Stankovich, S., D.A. Dikin, R.D. Piner, K.A. Kohlhaas, A. Kleinhammes, Y. Jia, Y. Wu, S.T. Nguyen, and R.S. Ruoff, Synthesis of graphene-based nanosheets via chemical reduction of exfoliated graphite oxide. Carbon 45 (7), 1558-1565 (2007).

[51] Park, S., J. An, I. Jung, R.D. Piner, S.J. An, X. Li, A. Velamakanni, and R.S. Ruoff, Colloidal suspensions of highly reduced graphene oxide in a wide variety of organic solvents. Nano Letters 9 (4), 1593-1597 (2009).

[52] Zhang, J., H. Yang, G. Shen, P. Cheng, J. Zhang, and S. Guo, Reduction of graphene oxide via L-ascorbic acid. Chemical Communications 46 (7), 1112-1114 (2010).

[53] Pei, S., J. Zhao, J. Du, W. Ren, and H.-M. Cheng, Direct reduction of graphene oxide films into highly conductive and flexible graphene films by hydrohalic acids. Carbon 48 (15), 4466-4474 (2010).

[54] Zhou, M., Y. Wang, Y. Zhai, J. Zhai, W. Ren, F. Wang, and S. Dong, Controlled Synthesis of Large-Area and Patterned Electrochemically Reduced Graphene Oxide Films. Chemistry-A European Journal 15 (25), 6116-6120 (2009).

[55] Wang, Z., X. Zhou, J. Zhang, F. Boey, and H. Zhang, Direct electrochemical reduction of single-layer graphene oxide and subsequent functionalization with glucose oxidase. The Journal of Physical Chemistry C 113 (32), 14071-14075 (2009).

[56] Shao, Y., J. Wang, M. Engelhard, C. Wang, and Y. Lin, Facile and controllable electrochemical reduction of graphene oxide and its applications. Journal of Materials Chemistry 20 (4), 743-748 (2010).

[57] Maiti, U.N., J. Lim, K.E. Lee, W.J. Lee, and S.O. Kim, Three-Dimensional Shape Engineered, Interfacial Gelation of Reduced Graphene Oxide for High Rate, Large

Capacity Supercapacitors. Advanced Materials 26 (4), 615-619 (2014).

[58] Cao, X., D. Qi, S. Yin, J. Bu, F. Li, C.F. Goh, S. Zhang, and X. Chen, Ambient Fabrication of Large-Area Graphene Films via a Synchronous Reduction and Assembly Strategy. Advanced Materials 25 (21), 2957-2962 (2013).

[59] Zhang, L., J. Xia, Q. Zhao, L. Liu, and Z. Zhang, Functional graphene oxide as a nanocarrier for controlled loading and targeted delivery of mixed anticancer drugs. Small 6 (4), 537-544 (2010).

[60] Yang, X., Y. Wang, X. Huang, Y. Ma, Y. Huang, R. Yang, H. Duan, and Y. Chen, Multi-functionalized graphene oxide based anticancer drug-carrier with dual-targeting function and pH-sensitivity. Journal of Materials Chemistry 21 (10), 3448-3454 (2011).

[61] Yang, K., J. Wan, S. Zhang, B. Tian, Y. Zhang, and Z. Liu, The influence of surface chemistry and size of nanoscale graphene oxide on photothermal therapy of cancer using ultra-low laser power. Biomaterials 33 (7), 2206-2214 (2012).

[62] Zhu, Y., S. Murali, M.D. Stoller, K. Ganesh, W. Cai, P.J. Ferreira, A. Pirkle, R.M. Wallace, K.A. Cychosz, and M. Thommes, Carbon-based supercapacitors produced by activation of graphene. Science 332 (6037), 1537-1541 (2011).

[63] Wang, Y., Z. Shi, Y. Huang, Y. Ma, C. Wang, M. Chen, and Y. Chen, Supercapacitor devices based on graphene materials. The Journal of Physical Chemistry C 113 (30), 13103-13107 (2009).

[64] Song, Y., K. Qu, C. Zhao, J. Ren, and X. Qu, Graphene oxide: intrinsic peroxidase catalytic activity and its application to glucose detection. Advanced Materials 22 (19), 2206-2210 (2010).

[65] Huang, C., C. Li and G. Shi, Graphene based catalysts. Energy & Environmental Science 5 (10), 8848-8868 (2012).

[66] Zhang, L.L. and X. Zhao, Carbon-based materials as supercapacitor electrodes. Chemical Society Reviews 38 (9), 2520-2531 (2009).

[67] Yoon, Y., K. Lee, C. Baik, H. Yoo, M. Min, Y. Park, S.M. Lee, and H. Lee, Anti-Solvent Derived Non-Stacked Reduced Graphene Oxide for High Performance Supercapacitors. Advanced Materials 25 (32), 4437-4444 (2013).

[68] Liu, C., Z. Yu, D. Neff, A. Zhamu, and B.Z. Jang, Graphene-based supercapacitor with an ultrahigh energy density. Nano Letters 10 (12), 4863-4868 (2010).

[69] Yan, J., Q. Wang, T. Wei, L. Jiang, M. Zhang, X. Jing, and Z. Fan, Template-Assisted Low Temperature Synthesis of Functionalized Graphene for Ultra-High Volumetric Performance Supercapacitors. ACS Nano 8(5), 4720-4729 (2014).

[70] Cheng, Q., J. Tang, J. Ma, H. Zhang, N. Shinya, and L.-C. Qin, Graphene and carbon nanotube composite electrodes for supercapacitors with ultra-high energy density. Physical Chemistry Chemical Physics 13 (39), 17615-17624 (2011).

[71] Li, H., Y. Wang, Y. Shi, J. Li, L. He, and H.Y. Yang, Large scale synthesized sulphonated reduced graphene oxide: a high performance material for electrochemical

capacitors. RSC Advances 3 (35), 14954-14959 (2013).

[72] Wei, W., X. Cui, W. Chen, and D.G. Ivey, Manganese oxide-based materials as electrochemical supercapacitor electrodes. Chemical Society Reviews 40 (3), 1697-1721 (2011).

[73] Chen, S., J. Zhu, X. Wu, Q. Han, and X. Wang, Graphene oxide-MnO_2 nanocomposites for supercapacitors. ACS Nano 4 (5), 2822-2830 (2010).

[74] Zhang, K., L.L. Zhang, X. Zhao, and J. Wu, Graphene/polyaniline nanofiber composites as supercapacitor electrodes. Chemistry of Materials 22 (4), 1392-1401 (2010).

[75] Wuest, J.D. and A. Rochefort, Strong adsorption of aminotriazines on graphene. Chemical Communications 46 (17), 2923-2925 (2010).

[76] Xu, Y., Z. Lin, X. Huang, Y. Wang, Y. Huang, and X. Duan, Functionalized Graphene Hydrogel-Based High-Performance Supercapacitors. Advanced Materials 25 (40), 5779-5784 (2013).

[77] Lu, Y., Y. Huang, F. Zhang, L. Zhang, X. Yang, T. Zhang, K. Leng, M. Zhang, and Y. Chen, Functionalized graphene oxide based on *p*-phenylenediamine as spacers and nitrogen dopants for high performance supercapacitors. Chinese Science Bulletin 59 (16), 1809-1815 (2014).

[78] Cui, Y., Q.-Y. Cheng, H. Wu, Z. Wei, and B.-H. Han, Graphene oxide-based benzimidazole-crosslinked networks for high-performance supercapacitors. Nanoscale 5 (18), 8367-8374 (2013).

[79] Chen, J., K. Sheng, P. Luo, C. Li, and G. Shi, Graphene Hydrogels Deposited in Nickel Foams for High-Rate Electrochemical Capacitors. Advanced Materials 24 (33), 4569-4573 (2012).

[80] Zhang, L. and G. Shi, Preparation of highly conductive graphene hydrogels for fabricating supercapacitors with high rate capability. The Journal of Physical Chemistry C 115 (34), 7206-17212 (2011).

[81] Miller, J.R., R. Outlaw and B. Holloway, Graphene double-layer capacitor with ac line-filtering performance. Science 329 (5999), 1637-1639 (2010).

[82] Lin, J., C. Zhang, Z. Yan, Y. Zhu, Z. Peng, R.H. Hauge, D. Natelson, and J.M. Tour, 3-dimensional graphene carbon nanotube carpet-based microsupercapacitors with high electrochemical performance. Nano Letters 13 (1), 72-78 (2012).

[83] Sheng, K., Y. Sun, C. Li, W. Yuan, and G. Shi, Ultrahigh-rate supercapacitors based on eletrochemically reduced graphene oxide for ac line-filtering. Scientific Reports 2, 247 (2012).

[84] Waldner, J.-B., Nanocomputers and swarm intelligence. John Wiley & Sons (2013).

[85] Lin, W., Carbon nanotubes for thermal interface materials. Microelectronic Packaging, Georgia Institute of Technology (2011).

[86] Becker, G., C. Lee and Z. Lin, Thermal conductivity in advanced chips: Emerging generation of thermal greases offers advantages. Advanced Packaging 14 (7), 14

(2005).

[87] Intel Corporation, http://citeseerx.ist.psu.edu/viewdoc/summary?doi=10.1.1. 14.8322

[88] Khatri, P. and J. Ziemski. " Dry-to-the-touch" thermal grease. Advanced Packaging Materials: Processes, Properties and Interfaces, Proceedings International Symposium, IEEE (2001).

[89] Khatri, P., Dry thermal grease. Patent EP1189278A2 (2002).

[90] Blazej, D., Thermal interface materials. Electronics Cooling 9, 14-21 (2003).

[91] Webb, R.L. and J.P. Gwinn. Low melting point thermal interface material. Thermal and Thermomechanical Phenomena in Electronic Systems, the Eighth Intersociety Conference, IEEE (2002).

[92] Macris, C.G., T.R. Sanderson, R.G. Ebel, C.B. Leyerle, and E. Solutions. Performance, reliability, and approaches using a low melt alloy as a thermal interface material. Proceedings IMAPS (2004).

[93] Huang, H., Y. Wu, C.-H. Liu, and S.-S. Fan, Thermal interface material and method for manufacturing same. Patent US8029900 (2008).

[94] Matayabas Jr, J.C. and P.A. Koning, Phase change thermal interface materials including exfoliated clay. Patent US6924027 (2005).

[95] Jayaraman, S., P.A. Koning and A. Dani, Phase change material containing fusible particles as thermally conductive filler. Patent US20030153667 (2011).

[96] Chaowasakoo, T., T.H. Ng, J. Songninluck, M.B. Stern, and S. Ankireddi. Indium solder as a thermal interface material using fluxless bonding technology. Semiconductor Thermal Measurement and Management Symposium, 25th Annual IEEE (2009).

[97] Deppisch, C., T. Fitzgerald, A. Raman, F. Hua, C. Zhang, P. Liu, and M. Miller, The material optimization and reliability characterization of an indium-solder thermal interface material for CPU packaging. JOM 58 (6), 67-74 (2006).

[98] Hu, C. and D. Lu, Fluxless die-to-heat spreader bonding using thermal interface material. Patent US7009289 (2006).

[99] Dutta, I., R. Raj, P. Kumar, T. Chen, C. Nagaraj, J. Liu, M. Renavikar, and V. Wakharkar, Liquid phase sintered solders with indium as minority phase for next generation thermal interface material applications. Journal of Electronic Materials 38 (12), 2735-2745 (2009).

[100] Houle, S.J. and A.A. Dani, Multi-layer polymer-solder hybrid thermal interface material for integrated heat spreader and method of making same. Patent US20060124700 (2006).

[101] Sim, L.C., S. Ramanan, H. Ismail, K. Seetharamu, and T. Goh, Thermal characterization of Al_2O_3 and ZnO reinforced silicone rubber as thermal pads for heat dissipation purposes. Thermochimica Acta 430 (1), 155-165 (2005).

[102] Chen, X., M.A. Dam, K. Ono, A. Mal, H. Shen, S.R. Nutt, K. Sheran, and F. Wudl,

A thermally re-mendable cross-linked polymeric material. Science 295 (5560), 1698-1702 (2002).

[103] Sagal, E.M., Thermally conductive elastomeric heat dissipation assembly with snap-in heat transfer conduit. Patent US6651732 (2003).

[104] Tajbakhsh, A. and E. Terentjev, Spontaneous thermal expansion of nematic elastomers. the European Physical Journal E 6 (2), 181-188 (2001).

[105] Yu, H., L. Li, T. Kido, G. Xi, G. Xu, and F. Guo, Thermal and insulating properties of epoxy/aluminum nitride composites used for thermal interface material. Journal of Applied Polymer Science 124 (1), 669-677 (2012).

[106] Zhao, Y.-H., Z.-K. Wu and S.-L. Bai, Study on thermal properties of graphene foam/graphene sheets filled polymer composites. Composites Part A: Applied Science and Manufacturing 72, 200-206 (2015).

[107] Thounthong, P., S. Rael and B. Davat, Energy management of fuel cell/battery/supercapacitor hybrid power source for vehicle applications. Journal of Power Sources 193 (1), 376-385 (2009).

[108] Gamby, J., P. Taberna, P. Simon, J. Fauvarque, and M. Chesneau, Studies and characterisations of various activated carbons used for carbon/carbon supercapacitors. Journal of Power Sources 101 (1), 109-116 (2001).

[109] An, K.H., W.S. Kim, Y.S. Park, J.-M. Moon, D.J. Bae, S.C. Lim, Y.S. Lee, and Y.H. Lee, Electrochemical properties of high-power supercapacitors using single-walled carbon nanotube electrodes. Advanced Functional Materials 11 (5), 387-392 (2001).

[110] Lin, Z., Y. Liu, Y. Yao, O.J. Hildreth, Z. Li, K. Moon, and C.-p. Wong, Superior capacitance of functionalized graphene. Journal of Physical Chemistry C 115 (14), 7120-7125 (2011).

[111] Ji, H., X. Zhao, Z. Qiao, J. Jung, Y. Zhu, Y. Lu, L.L. Zhang, A.H. MacDonald, and R.S. Ruoff, Capacitance of carbon-based electrical double-layer capacitors. Nature Communications 5, 4317 (2014).

[112] Yu, D. and L. Dai, Self-assembled graphene/carbon nanotube hybrid films for supercapacitors. The Journal of Physical Chemistry Letters 1 (2), 467-470 (2009).

[113] Stoller, M.D., S. Park, Y. Zhu, J. An, and R.S. Ruoff, Graphene-based ultracapacitors. Nano Letters 8 (10), 3498-3502 (2008).

[114] Chen, Y., X. Zhang, P. Yu, and Y. Ma, Stable dispersions of graphene and highly conducting graphene films: a new approach to creating colloids of graphene monolayers. Chemical Communications (30), 4527-4529 (2009).

[115] Hummers Jr, W.S. and R.E. Offeman, Preparation of graphitic oxide. Journal of the American Chemical Society 80 (6), 1339-1339 (1958).

[116] Wu, Z.-K., Z. Lin, L. Li, B. Song, K.-s. Moon, S.-L. Bai, and C.-P. Wong, Flexible micro-supercapacitor based on in-situ assembled graphene on metal template at room temperature. Nano Energy 10, 222-228 (2014).

[117] Li, D., M.B. Müller, S. Gilje, R.B. Kaner, and G.G. Wallace, Processable aqueous

dispersions of graphene nanosheets. Nature Nanotechnology 3 (2), 101-105 (2008).

[118] Xu, Y., H. Bai, G. Lu, C. Li, and G. Shi, Flexible graphene films via the filtration of water-soluble noncovalent functionalized graphene sheets. Journal of the American Chemical Society 130 (18), 5856-5857 (2008).

[119] Compton, O.C., D.A. Dikin, K.W. Putz, L.C. Brinson, and S.T. Nguyen, Electrically conductive "alkylated" graphene paper via chemical reduction of amine-functionalized graphene oxide paper. Advanced Materials 22 (8), 892-896 (2010).

[120] Wang, H., J.T. Robinson, X. Li, and H. Dai, Solvothermal reduction of chemically exfoliated graphene sheets. Journal of the American Chemical Society 131 (29), 9910-9911 (2009).

[121] Rochefort, A. and J.D. Wuest, Interaction of substituted aromatic compounds with graphene. Langmuir 25 (1), 210-215 (2008).

[122] Xue, T., S. Jiang, Y. Qu, Q. Su, R. Cheng, S. Dubin, C.Y. Chiu, R. Kaner, Y. Huang, and X. Duan, Graphene-Supported Hemin as a Highly Active Biomimetic Oxidation Catalyst. Angewandte Chemie 124 (16), 3888-3891 (2012).

[123] Stoller, M.D. and R.S. Ruoff, Best practice methods for determining an electrode material's performance for ultracapacitors. Energy & Environment Science 3 (9), 1294-1301 (2010).

[124] Duić, L. and S. Grigić, The effect of polyaniline morphology on hydroquinone/quinone redox reaction. Electrochimica Acta 46 (18), 2795-2803 (2001).

[125] Pech, D., M. Brunet, H. Durou, P. Huang, V. Mochalin, Y. Gogotsi, P.-L. Taberna, and P. Simon, Ultrahigh-power micrometre-sized supercapacitors based on onion-like carbon. Nature Nanotechnology 5 (9), 651-654 (2010).

[126] Chmiola, J., C. Largeot, P.-L. Taberna, P. Simon, and Y. Gogotsi, Monolithic carbide-derived carbon films for micro-supercapacitors. Science 328 (5977), 480-483 (2010).

[127] Xing, H., X. Wang, C. Shen, and S. Li, Fabrication and tests of a three-dimensional microsupercapacitor using SU-8 photoresist as the separator. Micro & Nano Letters, IET 7 (12), 1166-1169 (2012).

[128] Pech, D., M. Brunet, P.-L. Taberna, P. Simon, N. Fabre, F. Mesnilgrente, V. Conédéra, and H. Durou, Elaboration of a microstructured inkjet-printed carbon electrochemical capacitor. Journal of Power Sources 195 (4), 1266-1269 (2010).

[129] Zhu, Y., L. Li, C. Zhang, G. Casillas, Z. Sun, Z. Yan, G. Ruan, Z. Peng, A.-R.O. Raji, and C. Kittrell, A seamless three-dimensional carbon nanotube graphene hybrid material. Nature Communications 3, 1225 (2012).

[130] Beidaghi, M. and C. Wang, Micro-Supercapacitors Based on Interdigital Electrodes of Reduced Graphene Oxide and Carbon Nanotube Composites with Ultrahigh Power Handling Performance. Advanced Functional Materials 22 (21), 4501-4510 (2012).

[131] Niu, Z., L. Zhang, L. Liu, B. Zhu, H. Dong, and X. Chen, All-Solid-State Flexible Ultrathin Micro-Supercapacitors Based on Graphene. Advanced Materials 25 (29), 4035-4042 (2013).

[132] Wu, Z.S., K. Parvez, A. Winter, H. Vieker, X. Liu, S. Han, A. Turchanin, X. Feng, and K. Müllen, Layer-by-layer Assembled Heteroatom-Doped Graphene Films with Ultrahigh Volumetric Capacitance and Rate Capability for Micro-Supercapacitors. Advanced Materials 26 (26), 4552-4558 (2014).

[133] Wu, Z.S., K. Parvez, X. Feng, and K. Müllen, Graphene-based in-plane micro-supercapacitors with high power and energy densities. Nature communications 4, 2487 (2013).

[134] Xu, Y., Z. Lin, X. Huang, Y. Wang, Y. Huang, and X. Duan, Functionalized Graphene Hydrogel-Based High-Performance Supercapacitors. Advanced Materials 25 (40), 5779-5784 (2013).

[135] Hummers Jr, W.S. and R.E. Offeman, Preparation of graphitic oxide. Journal of the American Chemical Society 80 (6), 1339-1339 (1958).

[136] Cao, X., D. Qi, S. Yin, J. Bu, F. Li, C.F. Goh, S. Zhang, and X. Chen, Ambient Fabrication of Large-Area Graphene Films via a Synchronous Reduction and Assembly Strategy. Advanced Materials 25 (21), 2957-2962 (2013).

[137] Kim, M.S., B. Hsia, C. Carraro, and R. Maboudian, Flexible micro-supercapacitors with high energy density from simple transfer of photoresist-derived porous carbon electrodes. Carbon 74, 163-169 (2014).

[138] Maiti, U.N., J. Lim, K.E. Lee, W.J. Lee, and S.O. Kim, Three-Dimensional Shape Engineered, Interfacial Gelation of Reduced Graphene Oxide for High Rate, Large Capacity Supercapacitors. Advanced Materials 26 (4), 615-619 (2014).

[139] Yoon, Y., K. Lee, S. Kwon, S. Seo, H. Yoo, S. Kim, Y. Shin, Y. Park, D. Kim, and J.-Y. Choi, Vertical Alignments of Graphene Sheets Spatially and Densely Piled for Fast Ion Diffusion in Compact Supercapacitors. ACS Nano 5 (8), 4580-4590 (2014).

[140] Compton, O.C., B. Jain, D.A. Dikin, A. Abouimrane, K. Amine, and S.T. Nguyen, Chemically active reduced graphene oxide with tunable C/O ratios. ACS Nano 5 (6), 4380-4391 (2011).

[141] Wang, H., J.T. Robinson, X. Li, and H. Dai, Solvothermal reduction of chemically exfoliated graphene sheets. Journal of the American Chemical Society 131 (29), 9910-9911 (2009).

[142] Lin, Z., Y. Liu, Y. Yao, O.J. Hildreth, Z. Li, K. Moon, and C.-p. Wong, Superior capacitance of functionalized graphene. The Journal of Physical Chemistry C 115 (14), 7120-7125 (2011).

[143] Szabó, T., O. Berkesi, P. Forgó, K. Josepovits, Y. Sanakis, D. Petridis, and I. Dékány, Evolution of surface functional groups in a series of progressively oxidized graphite oxides. Chemistry of Materials 18 (11), 2740-2749 (2006).

[144] Yang, X., L. Qiu, C. Cheng, Y. Wu, Z.F. Ma, and D. Li, Ordered Gelation of

Chemically Converted Graphene for Next-Generation Electroconductive Hydrogel Films. Angewandte Chemie International Edition 50 (32), 7325-7328 (2011).

[145] Gogotsi, Y. and P. Simon, True performance metrics in electrochemical energy storage. Science Magazine 334, 917-918 (2011).

[146] Niu, Z., W. Zhou, J. Chen, G. Feng, H. Li, W. Ma, J. Li, H. Dong, Y. Ren, and D. Zhao, Compact-designed supercapacitors using free-standing single-walled carbon nanotube films. Energy & Environmental Science 4 (4), 1440-1446 (2011).

[147] In, H.J., S. Kumar, Y. Shao-Horn, and G. Barbastathis, Origami fabrication of nanostructured, three-dimensional devices: Electrochemical capacitors with carbon electrodes. Applied Physics Letters 88 (8), 083104 (2006).

[148] Kaempgen, M., C.K. Chan, J. Ma, Y. Cui, and G. Gruner, Printable thin film supercapacitors using single-walled carbon nanotubes. Nano Letters 9 (5), 1872-1876 (2009).

[149] Sheng, K., Y. Sun, C. Li, W. Yuan, and G. Shi, Ultrahigh-rate supercapacitors based on eletrochemically reduced graphene oxide for ac line-filtering. Scientific Reports 2, 247 (2012).

[150] Gamby, J., P. Taberna, P. Simon, J. Fauvarque, and M. Chesneau, Studies and characterisations of various activated carbons used for carbon/carbon supercapacitors. Journal of Power Sources 101 (1), 109-116 (2001).

[151] Wu, Z.S., K. Parvez, A. Winter, H. Vieker, X. Liu, S. Han, A. Turchanin, X. Feng, and K. Müllen, Layer-by-Layer Assembled Heteroatom-Doped Graphene Films with Ultrahigh Volumetric Capacitance and Rate Capability for Micro-Supercapacitors. Advanced Materials 26 (26), 4552-4558 (2014).

[152] Miller, J.R. and P. Simon, Electrochemical capacitors for energy management. Science Magazine 321 (5889), 651-652 (2008).

[153] An, K.H., W.S. Kim, Y.S. Park, J.-M. Moon, D.J. Bae, S.C. Lim, Y.S. Lee, and Y.H. Lee, Electrochemical properties of high-power supercapacitors using single-walled carbon nanotube electrodes. Advanced Functional Materials 11 (5), 387-392 (2001).

[154] Mastragostino, M., C. Arbizzani and F. Soavi, Conducting polymers as electrode materials in supercapacitors. Solid State Ionics 148 (3), 493-498 (2002).

[155] Snook, G.A., P. Kao and A.S. Best, Conducting-polymer-based supercapacitor devices and electrodes. Journal of Power Sources 196 (1), 1-12 (2011).

[156] Wei, W., X. Cui, W. Chen, and D.G. Ivey, Manganese oxide-based materials as electrochemical supercapacitor electrodes. Chemical Society Reviews 40 (3), 1697-1721 (2011).

[157] Jiang, J. and A. Kucernak, Electrochemical supercapacitor material based on manganese oxide: preparation and characterization. Electrochimica Acta 47 (15), 2381-2386 (2002).

[158] Frackowiak, E., V. Khomenko, K. Jurewicz, K. Lota, and F. Beguin, Supercapacitors based on conducting polymers/nanotubes composites. Journal of

Power Sources 153 (2), 413-418 (2006).

[159] Zhang, K., L.L. Zhang, X. Zhao, and J. Wu, Graphene/polyaniline nanofiber composites as supercapacitor electrodes. Chemistry of Materials 22 (4), 1392-1401 (2010).

[160] Yoon, Y., K. Lee, S. Kwon, S. Seo, H. Yoo, S. Kim, Y. Shin, Y. Park, D. Kim, and J.-Y. Choi, Vertical Alignments of Graphene Sheets Spatially and Densely Piled for Fast Ion Diffusion in Compact Supercapacitors. ACS Nano 8 (5), 4580-4590 (2014).

[161] Niu, C., E.K. Sichel, R. Hoch, D. Moy, and H. Tennent, High power electrochemical capacitors based on carbon nanotube electrodes. Applied Physics Letters 70 (11), 1480-1482 (1997).

[162] Du, C. and N. Pan, Supercapacitors using carbon nanotubes films by electrophoretic deposition. Journal of Power Sources 160 (2), 1487-1494 (2006).

[163] Dubin, S., S. Gilje, K. Wang, V.C. Tung, K. Cha, A.S. Hall, J. Farrar, R. Varshneya, Y. Yang, and R.B. Kaner, A one-step, solvothermal reduction method for producing reduced graphene oxide dispersions in organic solvents. ACS Nano 4 (7), 3845-3852 (2010).

[164] Balducci, A., R. Dugas, P.-L. Taberna, P. Simon, D. Plee, M. Mastragostino, and S. Passerini, High temperature carbon-carbon supercapacitor using ionic liquid as electrolyte. Journal of Power Sources 165 (2), 922-927 (2007).

[165] Taberna, P., P. Simon and J.-F. Fauvarque, Electrochemical characteristics and impedance spectroscopy studies of carbon-carbon supercapacitors. Journal of the Electrochemical Society 150 (3), A292-A300 (2003).

[166] Prasher, R., Thermal interface materials: historical perspective, status, and future directions. Proceedings of the IEEE 94 (8), 1571-1586 (2006).

[167] Due, J. and A.J. Robinson, Reliability of thermal interface materials: A review. Applied Thermal Engineering 50 (1), 455-463 (2013).

[168] Pettes, M.T., H. Ji, R.S. Ruoff, and L. Shi, Thermal transport in three-dimensional foam architectures of few-layer graphene and ultrathin graphite. Nano Letters 12 (6), 2959-2964 (2012).

[169] Shahil, K.M. and A.A. Balandin, Graphene-multilayer graphene nanocomposites as highly efficient thermal interface materials. Nano Letters 12 (2), 861-867 (2012).

[170] Liang, Q., X. Yao, W. Wang, Y. Liu, and C.P. Wong, A three-dimensional vertically aligned functionalized multilayer graphene architecture: an approach for graphene-based thermal interfacial materials. ACS Nano 5 (3), 2392-2401 (2011).

[171] Zhou, Y., H. Wang, F. Xiang, H. Zhang, K. Yu, and L. Chen, A poly (vinylidene fluoride) composite with added self-passivated microaluminum and nanoaluminum particles for enhanced thermal conductivity. Applied Physics Letters 98 (18), 182906 (2011).

[172] Yu, A., P. Ramesh, M.E. Itkis, E. Bekyarova, and R.C. Haddon, Graphite nanoplatelet-epoxy composite thermal interface materials. The Journal of Physical

Chemistry C 111 (21), 7565-7569 (2007).

[173] Tian, X., M.E. Itkis, E.B. Bekyarova, and R.C. Haddon, Anisotropic thermal and electrical properties of thin thermal interface layers of graphite nanoplatelet-based composites. Scientific Reports 3, 1710 (2013).

[174] Lee, Y., S. Shanmugan and D. Mutharasu, Thermal resistance of CNTs-based thermal interface material for high power solid state device packages. Applied Physics A 114 (4), 1145-1152 (2014).

[175] Song, W.-L., L.M. Veca, C.Y. Kong, S. Ghose, J.W. Connell, P. Wang, L. Cao, Y. Lin, M.J. Meziani, and H. Qian, Polymeric nanocomposites with graphene sheets: Materials and device for superior thermal transport properties. Polymer 53 (18), 3910-3916 (2012).

[176] Ramanath, G., G. Cui, P. Ganesan, X. Guo, A.V. Ellis, M. Stukowski, K. Vijayamohanan, P. Doppelt, and M. Lane, Self-assembled subnanolayers as interfacial adhesion enhancers and diffusion barriers for integrated circuits. Applied Physics Letters 83 (2), 383-385 (2003).

[177] Zhang, K., G.-W. Xiao, H.-W. Gu, M. Yuen, P.C. Chan, and B. Xu. Study on thermal interface material with carbon nanotubes and carbon black in high-brightness LED packaging with flip-chip. Electronic Components and Technology Conference, Proceedings 55th IEEE (2005).

[178] Konatham, D. and A. Striolo, Thermal boundary resistance at the graphene-oil interface. Applied Physics Letters 95 (16), 163105 (2009).

[179] Chen, S., Q. Wu, C. Mishra, J. Kang, H. Zhang, K. Cho, W. Cai, A.A. Balandin, and R.S. Ruoff, Thermal conductivity of isotopically modified graphene. Nature Materials 11 (3), 203-207 (2012).

[180] Balandin, A.A., Thermal properties of graphene and nanostructured carbon materials. Nature Materials 10 (8), 569-581 (2011).

[181] Wang, H., J. Gong, Y. Pei, and Z. Xu, Thermal Transfer in Graphene-Interfaced Materials: Contact Resistance and Interface Engineering. ACS Applied Materials & Interfaces 5 (7), 2599-2603 (2013).

[182] Jang, W., Z. Chen, W. Bao, C.N. Lau, and C. Dames, Thickness-dependent thermal conductivity of encased graphene and ultrathin graphite. Nano Letters 10 (10), 3909-3913 (2010).

[183] Behnam, A., A.S. Lyons, M.-H. Bae, E.K. Chow, S. Islam, C.M. Neumann, and E. Pop, Transport in nanoribbon interconnects obtained from graphene grown by chemical vapor deposition. Nano Letters 12 (9), 4424-4430 (2012).

[184] Seol, J.H., I. Jo, A.L. Moore, L. Lindsay, Z.H. Aitken, M.T. Pettes, X. Li, Z. Yao, R. Huang, and D. Broido, Two-dimensional phonon transport in supported graphene. Science 328 (5975), 213-216 (2010).

[185] Xu, Y., X. Luo and D. Chung, Sodium silicate based thermal interface material for high thermal contact conductance. Journal of Electronic Packaging 122 (2), 128-131

(2000).

[186] Prasher, R.S. and J. Matayabas Jr, Thermal contact resistance of cured gel polymeric thermal interface material. Components and Packaging Technologies, IEEE Transactions 27 (4), 702-709 (2004).

[187] Sarvar, F., D.C. Whalley and P.P. Conway. Thermal interface materials-A review of the state of the art. Electronics System integration Technology Conference, IEEE (2006).

[188] Leong, C.K. and D. Chung, Carbon black dispersions as thermal pastes that surpass solder in providing high thermal contact conductance. Carbon 41 (13), 2459-2469 (2003).

[189] Hopkins, P.E., M. Baraket, E.V. Barnat, T.E. Beechem, S.P. Kearney, J.C. Duda, J.T. Robinson, and S.G. Walton, Manipulating thermal conductance at metal–graphene contacts via chemical functionalization. Nano Letters 12 (2), 590-595 (2012).

[190] Ganguli, S., A.K. Roy and D.P. Anderson, Improved thermal conductivity for chemically functionalized exfoliated graphite/epoxy composites. Carbon 46 (5), 806-817 (2008).

[191] Song, S.H., K.H. Park, B.H. Kim, Y.W. Choi, G.H. Jun, D.J. Lee, B.S. Kong, K.W. Paik, and S. Jeon, Enhanced Thermal Conductivity of Epoxy-Graphene Composites by Using Non-Oxidized Graphene Flakes with Non-Covalent Functionalization. Advanced Materials 25 (5), 732-737 (2013).

[192] Sedeh, M.M. and J. Khodadadi, Thermal conductivity improvement of phase change materials/graphite foam composites. Carbon 60, 117-128 (2013).

[193] Cai, W., A.L. Moore, Y. Zhu, X. Li, S. Chen, L. Shi, and R.S. Ruoff, Thermal transport in suspended and supported monolayer graphene grown by chemical vapor deposition. Nano Letters 10 (5), 1645-1651 (2010).

[194] Ghosh, S., W. Bao, D.L. Nika, S. Subrina, E.P. Pokatilov, C.N. Lau, and A.A. Balandin, Dimensional crossover of thermal transport in few-layer graphene. Nature Materials 9 (7), 555-558 (2010).

[195] Berber, S., Y.-K. Kwon and D. Tomanek, Unusually high thermal conductivity of carbon nanotubes. Physical Review Letters 84 (20), 4613 (2000).

[196] Hone, J., Carbon nanotubes: thermal properties. Journal of Nanoscience and Nanotechnology 6, 603-610 (2004).

[197] Fujii, M., X. Zhang, H. Xie, H. Ago, K. Takahashi, T. Ikuta, H. Abe, and T. Shimizu, Measuring the thermal conductivity of a single carbon nanotube. Physical Review Letters 95 (6), 065502 (2005).

[198] Nan, C.-W., Z. Shi and Y. Lin, A simple model for thermal conductivity of carbon nanotube-based composites. Chemical Physics Letters 375 (5), 666-669 (2003).

[199] Biercuk, M., M.C. Llaguno, M. Radosavljevic, J. Hyun, A.T. Johnson, and J.E. Fischer, Carbon nanotube composites for thermal management. Applied Physics Letters, 2002. 80(15): p. 2767-2769.

[200] Gojny, F.H., M.H. Wichmann, B. Fiedler, I.A. Kinloch, W. Bauhofer, A.H. Windle, and K. Schulte, Evaluation and identification of electrical and thermal conduction mechanisms in carbon nanotube/epoxy composites. Polymer 47 (6), 2036-2045 (2006).

[201] Nan, C.-W., G. Liu, Y. Lin, and M. Li, Interface effect on thermal conductivity of carbon nanotube composites. Applied Physics Letters 85 (16), 3549-3551 (2004).

[202] Bryning, M., D. Milkie, M. Islam, J. Kikkawa, and A. Yodh, Thermal conductivity and interfacial resistance in single-wall carbon nanotube epoxy composites. Applied Physics Letters 87 (16), 161909 (2005).

[203] Tong, T., Y. Zhao, L. Delzeit, A. Kashani, M. Meyyappan, and A. Majumdar, Dense vertically aligned multiwalled carbon nanotube arrays as thermal interface materials. Components and Packaging Technologies, IEEE Transactions 30 (1), 92-100 (2007).

[204] Ngo, Q., B.A. Cruden, A.M. Cassell, G. Sims, M. Meyyappan, J. Li, and C.Y. Yang, Thermal interface properties of Cu-filled vertically aligned carbon nanofiber arrays. Nano Letters 4 (12), 2403-2407 (2004).

[205] Xu, J. and T.S. Fisher, Enhancement of thermal interface materials with carbon nanotube arrays. International Journal of Heat and Mass Transfer 49 (9), 1658-1666 (2006).

[206] Jakubinek, M.B., M.A. White, G. Li, C. Jayasinghe, W. Cho, M.J. Schulz, and V. Shanov, Thermal and electrical conductivity of tall, vertically aligned carbon nanotube arrays. Carbon 48 (13), 3947-3952 (2010).

[207] Balandin, A.A., S. Ghosh, W. Bao, I. Calizo, D. Teweldebrhan, F. Miao, and C.N. Lau, Superior thermal conductivity of single-layer graphene. Nano Letters 8 (3), 902-907 (2008).

[208] Chen, Z., W. Ren, L. Gao, B. Liu, S. Pei, and H.-M. Cheng, Three-dimensional flexible and conductive interconnected graphene networks grown by chemical vapour deposition. Nature Materials 10 (6), 424-428 (2011).

[209] Xu, Y., Y. Zhang, E. Suhir, and X. Wang, Thermal properties of carbon nanotube array used for integrated circuit cooling. Journal of Applied Physics 100 (7), 074302 (2006).

[210] Zhu, L., D.W. Hess and C. Wong. Assembling carbon nanotube films as thermal interface materials. Electronic Components and Technology Conference, Proceedings 57th, IEEE (2007).

[211] Parker, W., R. Jenkins, C. Butler, and G. Abbott, Flash method of determining thermal diffusivity, heat capacity, and thermal conductivity. Journal of Applied Physics 32 (9), 1679-1684 (1961).

[212] McNamara, A., V. Sahu, Y. Joshi, and Z. Zhang. Infrared imaging microscope as an effective tool for measuring thermal resistance of emerging interface materials. ASME/JSME 2011 8th Thermal Engineering Joint Conference, American Society of Mechanical Engineers (2011).

[213] Liu, Z., Z. Li, Z. Xu, Z. Xia, X. Hu, L. Kou, L. Peng, Y. Wei, and C. Gao, Wet-spun continuous graphene films. Chemistry of Materials 26 (23), 6786-6795 (2014)

VITA

Zhenkun Wu

Zhenkun Wu was born in Xiantao, Hubei Province, China. He received his B.S. in Physics from Peking University, China 2009. In 2009, he joined Dr. Bai, Shulin's group in the Department of Materials Science and Engineering, Peking University. In 2012, he participated in the Joint-Ph. D. Program between Peking University and Georgia Tech, where he joined Dr. C. P. Wong's group in School of Materials Science and Engineering at Georgia Tech, as a PhD student and graduate research assistant. He is expecting his PhD in Materials Science and Engineering in June 2015.